REVIEW

Check for updates

Surface engineering strategies for selectivity tuning and enhancement in photoelectrochemical biomass and CO₂ valorization

Yudhistira Tirtayasri Amrillah, [ID] [a] Kaijian Zhu, [ID] [b]
Fani Rahayu Hidayah Rayanisaputri, [ID] [a] Fita Widiyatun,[a] Vivi Fauzia, [ID] [a]
Munawar Khalil, [ID] [cde] Fatwa F. Abdi [ID] *[bc] and Ferry Anggoro Ardy Nugroho [ID] *[ad]

Biomass and CO₂ valorization constitutes a sustainable solution to mitigate global waste accumulation by converting biomass and CO₂ into valuable chemicals and fuels. Among various conversion strategies, photoelectrochemical (PEC) systems have emerged as a promising approach due to their ability to drive redox reactions under mild conditions using solar energy. However, challenges such as poor selectivity, charge recombination, and inefficient light harvesting hinder the widespread adoption of PEC biomass and CO₂ valorization. In efforts to push the concept into the practical realm, modifying the surface of the corresponding photoanodes has emerged as the most viable and effective approach. Acknowledging its importance, in this review, we thoroughly discuss various surface engineering strategies for enhancing and tuning PEC biomass and CO₂ valorization selectivity. We open the discussion by introducing the fundamental principles of PEC processes, system configurations, and the critical role of surface properties in governing reaction pathways. Building on the previous discussions, common surface engineering strategies, particularly surface functionalization, crystal face tuning, defect engineering, and nanostructuring, are systematically reviewed for their ability to tailor surface properties and modulate the electronic structures of photoelectrodes. Crucially, we provide insights into the interplay between photoelectrode design and reaction dynamics responsible for the improvement and tunability of PEC biomass and CO₂ valorization selectivity. By providing a comprehensive overview of recent advancements, this review aims to serve as a valuable resource for guiding future developments in PEC biomass and CO₂ valorization.

1. Introduction

The Industrial Revolution marked a turning point in human progress driving urbanization and industrialization as the primary pathways to economic and social development.[1] However, rapid industrial and economic growth largely relies on finite fossil fuel resources, raising urgent concerns about energy security, environmental degradation, and sustainability.[2] In response, global attention has turned toward renewable energy systems and circular economic models that reduce reliance on fossil fuels while mitigating waste accumulation and greenhouse gas emissions.[3,4] In parallel with the decline of fossil fuel reserves, annual waste generation is projected to increase from 2.0 billion tonnes in 2018 to 3.4 billion tonnes by 2050.[5] Without urgent intervention, the global annual cost of waste management could reach an alarming USD 640.3 billion.[6] To address the environmental and economic burden of waste accumulation, it is imperative to develop recycling methods that not only reduce waste volumes but also convert biomass and CO₂ into valuable chemicals and fuels, *i.e.*, upcycling.[7–9] One promising approach is establishing a circular economic system centered on biomass and CO₂ valorization to drive fuel production and waste reduction.[10] In its broadest sense, biomass encompasses all organic matter produced *via* photosynthesis, whether directly harvested from plants or generated as by-products from industrial and municipal processes.[11] In the context of waste reduction, biomass valorization plays a pivotal role by transforming organic waste materials, ranging from agricultural residues and food processing by-products to post-consumer waste, such as packaging, used vegetable oils,

ᵃDepartment of Physics, Faculty of Mathematics and Natural Sciences, Universitas Indonesia, Depok 16424, Indonesia. E-mail: f.a.a.nugroho@sci.ui.ac.id

ᵇSchool of Energy and Environment, City University of Hong Kong, 83 Tat Chee Avenue, Kowloon, Hong Kong S.A.R., China. E-mail: f.abdi@cityu.edu.hk

ᶜDepartment of Chemistry, Faculty of Mathematics and Natural Sciences, Universitas Indonesia, Depok 16424, Indonesia

ᵈInstitute for Advanced Sustainable Materials Research and Technology (INA-SMART), Faculty of Mathematics and Natural Sciences, Universitas Indonesia, Depok 16424, Indonesia

ᵉAdvanced Materials and Molecular Synthesis Laboratory, Department of Chemistry, Faculty of Mathematics and Natural Sciences, Universitas Indonesia, Depok 16424, Indonesia

and demolition debris, into high-value products.[12] Historically, agriculture has functioned as a circular economic system, repurposing livestock waste as manure, animal bedding, and soil-enriching by-products while utilizing crop residues to restore soil fertility.[13] Expanding this circular model to incorporate diverse biomass and waste sources presents a viable strategy for mitigating both environmental challenges and energy shortages.

Scientific and technological advances have demonstrated that biomass can be efficiently transformed into valuable chemicals such as phenol and catechol, both of which have widespread use in various industries (*e.g.*, automotive, aerospace, building materials, electronics, consumer goods applications, fragrances and pharmaceuticals).[14–17] However, conventional biomass valorization processes utilize a thermochemical approach that generally requires high temperatures, high pressures, and harsh reaction conditions, which severely limit reaction selectivity and overall process efficiency.[18,19] In response to these limitations, photoelectrochemical (PEC) systems have emerged as a promising alternative.[20] By harnessing solar energy to drive redox reactions under mild conditions, PEC technologies significantly reduce energy input and environmental impact while enabling the simultaneous production of value-added chemicals and fuels.[21,22] Despite these advantages, PEC conversion faces significant challenges. In particular, rapid recombination of photogenerated charge carriers, inefficient light harvesting, and nonselective substrate activation can lead to the formation of mixed products rather than a single, desired target compound. For example, in PEC glycerol oxidation, which has attracted significant interest in recent years, glycerol waste, a byproduct from, *e.g.*, diesel production, can be converted into products such as dihydroxy-acetone (DHA), formic acid (FA), glyceraldehyde (GLAD), glycolaldehyde (GCAD), and glycolic acid (GA), each with varying commercial values.[23–26] Among these, DHA is particularly attractive due to its high market value and demand in the cosmetics, pharmaceutical, fine chemicals, and food industries.[27,28] Yet, many high-efficiency methods tend to favor C–C bond cleavage, predominantly yielding lower-value compounds like FA rather than DHA. Similarly, PEC processes applied to 5-hydroxymethylfurfural (HMF) oxidation,[29] glucose oxidation,[30] methane conversion[31] and CO_2 reduction[32] encounter challenges in achieving selective multi-carbon product formation—a necessity for generating high-energy-density fuels—due to difficulties in managing multi-electron transfer, suppressing charge recombination, and ensuring efficient charge transport.

As the field of PEC biomass and CO_2 valorization continues to grow rapidly (Fig. 1), surface engineering has emerged as a critical strategy to overcome challenges related to reaction selectivity, efficiency, and stability. This focus is understandable since surfaces are the literal sites where the reactions occur; it is thus logical to first modify them to generate certain chemical products selectively. Furthermore, surface engineering encompasses virtually unlimited strategies, for which minute details on the surface modification may give rise to contrasting effects. Specifically, by tailoring the catalyst surface at the nanometer and atomic scales, researchers have successfully modified the
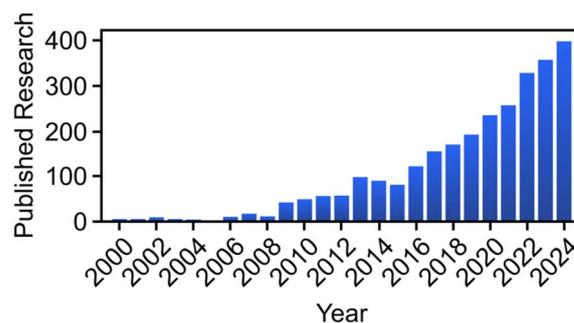

Fig. 1 Number of Scopus-indexed research articles published from 2000 to 2024 on PEC biomass valorization. The research trend on PEC biomass valorization has been rising in recent years. The search string used in Scopus was "(photoelectrochemical OR photoelectrocatalytic OR PEC) AND (oxidation OR reduction OR conversion OR valorization) AND NOT (water OR sensor OR cell)". Accessed March 22nd, 2025.

interfacial electronic structure, enhanced light absorption, and controlled the adsorption and activation of biomass-derived intermediates.[33,34] Furthermore, surface functionalization approaches, such as incorporating nanoparticles,[35,36] quantum dots,[37,38] single-atom metals,[39] layered double hydroxides and hydroxides,[40] and molecular cocatalysts,[41–43] not only enhance light harvesting efficiency and promote charge transport but also introduce more active reaction centers.[44,45] In addition, crystal facet tuning[46] and defect engineering[47,48] enable precise adjustment of active sites to selectively promote specific reaction pathways.

While several reviews have addressed PEC biomass[23,49] or CO_2 (ref. 50–52) valorization individually, a comprehensive focus on surface engineering strategies that directly influence selectivity remains lacking. This review aims to fill this gap by systematically highlighting how specific surface engineering approaches, including surface functionalization, crystal facet tuning, defect engineering, and nanostructuring, can tailor surface properties. Furthermore, we aim to emphasize the interplay between photoelectrode surface design and reaction dynamics, providing mechanistic insights into how such modifications steer selective biomass and CO_2 valorization. By integrating recent findings across both biomass and CO_2 valorization systems and offering a cross-cutting perspective on selectivity control through surface engineering, this review offers a timely and unique contribution that can guide future advancements in the rational design of PEC systems for sustainable chemical production. Doing so, we begin by introducing the prospects of PEC biomass and CO_2 valorization and its potential to significantly mitigate environmental and economic challenges. The principle of PEC valorization is then introduced along with typical PEC systems. Next, we discuss the importance of surface properties in PEC systems and their limitations, underscoring the necessity for surface engineering, followed by a detailed discussion on the principles, mechanisms, and the critical role of surface properties in PEC biomass valorization. Building upon this, state-of-the-art surface engineering strategies, including surface functionalization, crystal facet tuning, defect engineering, and nanostructuring

approaches, that have been employed to improve and tune the selectivity of PEC biomass valorization are discussed. By highlighting how the interplay between catalyst design, defect engineering, and interfacial charge transfer is essential for overcoming kinetic and thermodynamic barriers, this review provides insights into future research directions that could drive the development of cutting-edge PEC technologies for sustainable biomass valorization.

2. PEC biomass valorization

Despite the rising interest in PEC biomass valorization,[20] it still faces challenges such as low selectivity and limited efficiency, hindering its practical application and commercialization. Before discussing strategies targeted to alleviate these problems, it is therefore useful to first review the underlying principles of PEC biomass valorization, typical PEC systems, and the need for surface engineering for PEC biomass valorization. Understanding these factors will help one appreciate the various surface engineering strategies detailed in later sections.

2.1. Principles of PEC biomass valorization

PEC biomass valorization involves several key steps, beginning with light absorption using a photoelectrode. Initially, photons with energy higher than the bandgap of the semiconductor can be absorbed, exciting electrons from the valence band (VB, equivalent to the highest occupied molecular orbital, HOMO, in organic molecules) to the conduction band (CB, equivalent to the lowest occupied molecular orbital, LUMO, in organics), leaving behind holes in the VB. Here, the absorption coefficient plays a critical role in photon capture efficiency, as a higher absorption coefficient allows for thinner films and shorter charge transfer distances. Beyond the intrinsic properties of the material, strategies such as nanostructuring can introduce light-trapping effects, further enhancing light absorption efficiency.[53] The next step involves photogenerated charge

separation and recombination. In inorganic semiconductors, free electrons and holes are typically separated by internal electric fields, which can arise from various mechanisms such as band bending or facet engineering.[54] However, due to their low dielectric constant, organic semiconductors often require additional layers[55] or specific stacking configurations[56] to facilitate exciton dissociation into free charge carriers. Charge separation typically occurs within hundreds of femtoseconds to a few picoseconds, while charge recombination occurs on a timescale ranging from picoseconds to microseconds.[57] The lifetime of active charge carriers is influenced by various factors during transport, including particle–particle grain boundaries and defects. In general, materials with high conductivity, mobility, and charge carrier density enable more effective charge transport, reducing recombination losses. Finally, the transferred charge carriers accumulate on the electrode surface, driving chemical reactions. Since catalytic reactions occur over milliseconds to seconds, a significant portion of charge carriers may deactivate before contributing to the reaction. Additionally, the adsorption modes of different reactant molecules influence charge transfer from the electrode to the reactant, impacting biomass conversion kinetics and selectivity. As a result, the electrode/electrolyte interface plays a crucial role in determining reaction selectivity and efficiency.

When a semiconductor is immersed in an electrolyte, charge transfer occurs due to the potential difference between the semiconductor's Fermi level (E_F) and the electrolyte's redox potential (E_{redox}). Upon equilibration, E_F aligns with E_{redox}, leading to band bending and the formation of a space charge layer (Fig. 2a). Taking an n-type semiconductor used for oxidation reactions as an example, the downward shift of E_F induces upward band bending, which results in hole accumulation within the space charge layer. On the electrolyte side, an electrical double layer, consisting of the Stern layer and the Gouy-Chapman diffuse layer, forms at the interface. The Stern layer, located closest to the semiconductor, contains adsorbed ions
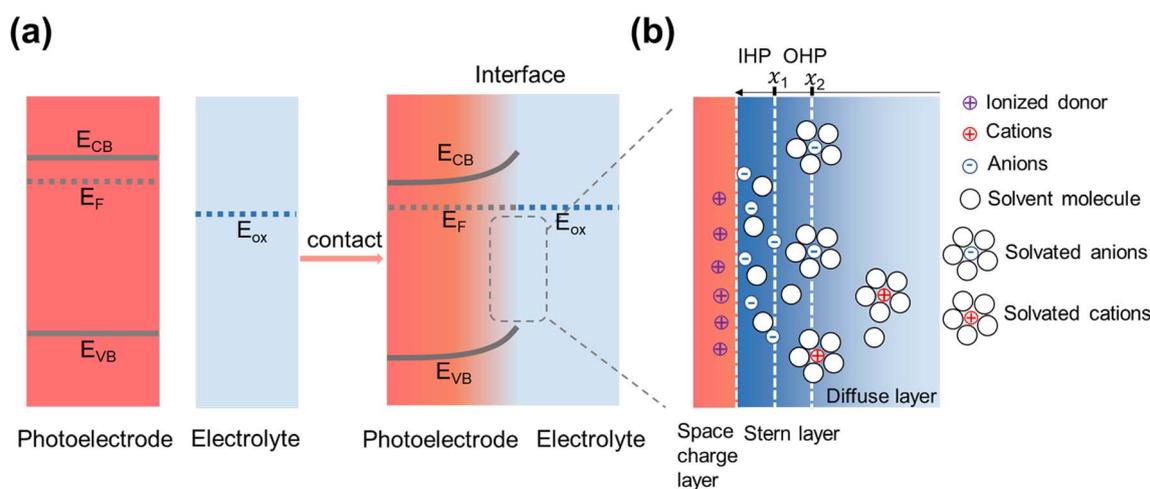

Fig. 2 Mechanism of photoelectrode/electrolyte interface equilibration. (a) The band energetics of a semiconductor/liquid before and after contact. (b) Model of the double-layer structure of an n-type semiconductor electrode in contact with the electrolyte under equilibrium conditions.

and solvated molecules and is further divided into the inner Helmholtz plane (IHP) and the outer Helmholtz plane (OHP). The IHP corresponds to the position of the electrical centers of adsorbed ions at a distance x_1, while the OHP represents the position of solvated molecules or ions, which can only approach the semiconductor up to a distance x_2 (see Fig. 2b).[58] In this regard, changes in electrolyte composition, such as variations in cations and anions, can significantly influence the distribution of adsorbed ions in the IHP and solvated species in the OHP, thereby affecting both reaction activity and selectivity. Several studies have reported the effects of different cations and anions on, *e.g.*, glycerol oxidation.[59,60] Beyond ion type, potential drops across the Stern layer and Gouy–Chapman diffuse layer must also be considered in biomass valorization. The concentration of biomass feedstock plays a crucial role in influencing ionic conductivity, electrolyte viscosity, and electrode surface coverage—all of which impact conversion efficiency and selectivity. For example, studies have shown that variations in glucose concentration distinctly affect mass transport and electron transfer kinetics.[61] In the case of glycerol oxidation, the peak current was found to increase as glycerol concentration rose from 0.5 to 1.0 M but decreased at concentrations above 1.0 M, a decline attributed to insufficient OH^- coverage on the electrode surface.[62] Another study investigated how varying glycerol concentrations influenced selectivity, finding that higher concentrations favored the production of C_3 products.[63]

2.2. Structure of a typical photoelectrochemical system

In terms of the photoelectrodes' arrangement, a PEC system can be typically categorized into S2, D2, and D4 configurations (Fig. 3).[64] The S2 configuration represents a single-bandgap PEC cell consisting of at least an anode and a cathode, with one electrode made from an n- or a p-type semiconductor capable of capturing sunlight. For example, when the photoanode is an n-type semiconductor, the cathode is typically a standard electrode material, such as Pt. When the photoanode absorbs light with sufficient energy, electrons in the VB are excited to the CB, leaving behind holes in the VB. Following charge separation, driven by either an internal or external electric field, the holes

migrate to the electrode surface, facilitating an oxidation reaction, while the electrons travel through the external circuit to the counter electrode, where they drive a reduction reaction. To enable the desired reaction, the semiconductor in a single-bandgap PEC cell must meet specific criteria. Particularly, its bandgap must be larger than the thermodynamic requirement for the overall reaction (*e.g.*, >1.23 eV for water splitting), with its CB and VB appropriately positioned to straddle the reduction and oxidation potentials (*e.g.*, CB < 0 V *vs.* RHE for H_2 evolution and VB > 1.23 V *vs.* RHE for O_2 evolution or 0.003 V *vs.* RHE for glycerol oxidation).[65] However, significant energy losses during charge separation, charge transport, and surface reaction kinetics typically result in overpotentials, necessitating a semiconductor with a higher bandgap (*e.g.*, >1.6 eV for water splitting).[66] This requirement limits material choices, and photons with energy lower than the bandgap are practically not utilized.

To broaden the solar spectrum absorption and mitigate the constraints of a single semiconductor, PEC systems can incorporate two photoactive materials, one as the photoanode and the other as the photocathode, classified as D2 or D4 configurations. In the D2 configuration, the two photoelectrodes are illuminated side by side, whereas the D4 configuration employs a tandem structure, where the two electrodes are optically stacked to achieve complementary light absorption. Due to the increased illuminated area, the theoretical solar conversion efficiency of the D2 configuration is lower than that of the D4 configuration. In the D4 setup, the VB position of the photoanode must be more positive than the oxidation potential, while the CB position of the photocathode must be more negative than the reduction potential. The complementary absorption of light by both electrodes allows transmitted light with lower energy to be captured by the second photoelectrode, improving light utilization. This approach enables an ideal theoretical solar conversion efficiency of up to 27%, even when accounting for energy losses (0.8 eV per absorbed photon).[64]

2.3. The need for surface engineering in PEC biomass valorization

Biomass valorization often yields multiple products from a single feedstock, yet not all products are desirable. From an
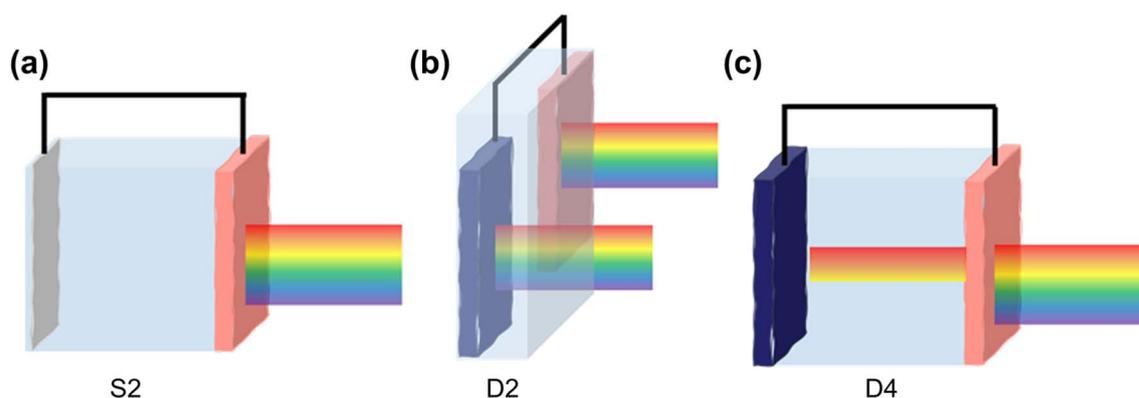

Fig. 3 Configurations of a typical PEC system. (a) S2, the system employs a single bandgap PEC cell with only one electrode absorbing light. (b) D2, the system utilizes a dual bandgap PEC cell with two electrodes being illuminated side-by-side. (c) D4, a dual bandgap PEC cell with two electrodes featuring complementary light absorption.

economic standpoint, high-value products, such as DHA and GLAD from glycerol oxidation or glycolic acid from ethylene glycol oxidation, are typically preferred.[67] The formation of multiple products reflects inefficient energy utilization and increases the costs of purification and separation, raising overall production expenses. Additionally, unwanted byproduct intermediates can also occupy active reaction sites, hindering catalysis. Consequently, achieving high selectivity toward a single desired product is essential in PEC biomass conversion. Several strategies have been proposed to enhance selectivity, including electrolyte composition and feedstock concentration adjustment.[68–70] However, since most reactions occur at the solid–liquid interface, the properties of the photoelectrode surface critically govern both reactivity and selectivity.

In PEC biomass valorization, surface engineering enhances conversion efficiency and selectivity through several key factors. One critical factor is surface area and morphology. Nanostructured surfaces, such as nanoporous or nanoarray architectures, generally outperform thin-film electrodes due to their increased active sites for biomass adsorption and subsequent reaction. Furthermore, nanostructuring is an effective strategy to shorten the transport length for photoexcited charges, reducing bulk recombination losses.[71,72] Another key aspect involves surface defects and functionalization. The electronic state at the surface differs from that of the bulk due to abrupt termination at the interface. Surface defects and adsorbed functional species can significantly influence catalytic behavior by tuning the adsorption energy of reactants and products, a crucial parameter in catalysis according to the Sabatier principle.[73–75] Moreover, surface functionalization can modulate charge transfer kinetics and recombination rates, directly affecting the overall reaction efficiency.[76,77]

The exposed facets on a material surface further dictate its catalytic performance. During crystal formation, facets with higher surface energies tend to grow rapidly and eventually diminish, while lower-energy facets remain stable.[78] Uncontrolled growth thus often yields less reactive surfaces. Since different facets exhibit distinct atomic arrangements and electronic structures, they can enable unique reaction pathways in biomass conversion.[79] For instance, some facets preferentially accumulate holes, while others favor electron accumulation,[80,81] allowing selective tuning of the reaction environment. The combination of these specific facets can create built-in electric fields, enhancing charge separation.[82,83]

Finally, the local surface environment also plays a significant role. Properties such as hydrophilicity, hydrophobicity, and surface polarity impact the solubility, diffusion, and adsorption of biomass feedstocks. Tailoring surface wettability can improve interfacial interactions between the electrode, electrolyte, and biomass molecules, enhancing reaction efficiency.[59,84] Furthermore, the polarizability of the surface has been reported to affect surface energy,[85] band bending,[86] and excited-state deactivation pathways,[87] all of which influence PEC reaction dynamics. In some cases, local confinement effects can restrict the adsorption modes of biomass molecules, further refining reaction selectivity.

2.4. PEC biomass and CO_2 valorization

Among the various PEC biomass valorization reactions, the glycerol oxidation reaction (GOR) is one of the most widely studied. Glycerol, a key by-product of biodiesel production, is abundant and inexpensive. These properties make it an ideal feedstock for conversion into value-added chemicals. Its three hydroxyl functional groups offer multiple oxidation pathways. For example, two-electron oxidation of the primary and secondary hydroxyl groups can yield glyceraldehyde (GLAD) and 1,3-dihydroxyacetone (DHA), respectively. Further oxidation can lead to more C_3 products such as glyceric acid (GLYA) and lactic acid (LA). When C–C bond cleavage occurs, C_2 and C_1 products such as glycolic acid (GA) and formic acid (FA) can be formed. Among these, DHA and GLAD exhibit high market value, while formic acid has broad industrial demand, drawing significant interest to these transformations.[23–26] In addition to glycerol, glucose ($C_6H_{12}O_6$), the most abundant monosaccharide, has also been extensively studied in PEC systems due to its polyhydroxy structure, which allows diverse oxidation pathways. Oxidation of the C–OH groups produces C_6 carboxylic acids such as gluconic acid and glucaric acid, while C–C bond cleavage can yield shorter-chain sugars and acids like arabinose, erythrose, glycolic acid, and formic acid.[88] Conventional electrochemical or catalytic oxidation of glucose often requires noble metal catalysts, alkaline media, and O_2.[89,90] These conditions are transferable to PEC systems, though challenges persist, including overoxidation and uncontrolled C–C cleavage, which hinder selectivity. Such limitations call for surface engineering strategies, which will be discussed in the subsequent sections.

Another target in biomass valorization is the oxidation of 5-hydroxymethylfurfural (HMF) to 2,5-furandicarboxylic acid (FDCA). HMF, derived from cellulose and hemicellulose, is a key platform molecule in biorefineries.[91,92] Its PEC oxidation to FDCA, a valuable monomer for bioplastics like polyethylene furanoate (PEF), has attracted growing attention.[93] This reaction proceeds *via* sequential oxidation of the aldehyde and alcohol functional groups in HMF, forming intermediates such as 5-hydroxymethyl-2-furancarboxylic acid (HMFCA) and 5-formyl-2-furancarboxylic acid (FFCA). Achieving high selectivity to FDCA under PEC conditions requires careful control of active sites, surface potential, and light-assisted oxidation kinetics.[94] Integration of co-catalysts and tuning of semiconductor surfaces are emerging strategies to promote FDCA formation while suppressing side reactions. In a similar context, aromatic alcohols such as benzyl alcohol can be selectively oxidized to benzaldehyde or further to benzoic acid under PEC conditions.[95,96] These reactions represent valuable model systems for studying PEC oxidation mechanisms due to their relatively well-defined electron-transfer steps and stable intermediates. Oxidation of benzyl alcohol proceeds first to benzaldehyde, which can undergo further PEC oxidation to benzoic acid depending on the applied bias and reaction time. In addition, CO_2 valorization has emerged as a parallel strategy for utilizing solar energy in a sustainable manner.[97] The PEC reduction of CO_2 to C_1–C_3 products such as CO, formic acid, methanol, ethanol, and acetic

Table 1 Representative biomass and CO_2 valorization reactions

Feedstock	Product(s)	Reaction pathway(s)	Product utilization
Glycerol	Dihydroxyacetone	Oxidation[98]	Cosmetics, pharmaceuticals, fine chemicals, food[28,65,99]
	Formic acid	$C_3H_8O_3 \xrightarrow[2OH^-]{-2H_2O,-2e^-} C_3H_6O_3$ (DHA) Oxidation[100] $1.\ C_3H_8O_3 \xrightarrow[2OH^-]{-2H_2O,-2e^-} C_3H_6O_3\,(GLAD) \xrightarrow[3OH^-]{-2H_2O,-2e^-}$ $C_3H_5O_4 \xrightarrow[3OH^-]{-2H_2O,-2e^-} C_2H_4O_3 \xrightarrow[3OH^-]{-2H_2O,-2e^-} HCOO^-$ $2.\ C_3H_8O_3 \xrightarrow[2OH^-]{-2H_2O,-2e^-} C_3H_6O_3\,(GLAD) \xrightarrow[3OH^-]{-2H_2O,-2e^-} HCOO^-$ $C_3H_5O_4 \xrightarrow[3OH^-]{-2H_2O,-2e^-} HCOO^-$	Pharmaceuticals, agriculture, fuel technology, de-icing agents[101–103]
	Glyceraldehyde	Oxidation[100]	Pharmaceuticals, food, cosmetics, fuel production[104,105]
	Lactic acid	$C_3H_8O_3 \xrightarrow[2OH^-]{-2H_2O,-2e^-} C_3H_6O_3$ (GLAD) Oxidation[106] $C_3H_8O_3 \xrightarrow[2OH^-]{-2H_2O,-2e^-} C_3H_6O_3$ $(GLAD) \xrightarrow{OH^-} C_3H_6O_3\,(DHA) \xrightarrow{-H_2O} C_3H_4O_3\,(pyruvaldehyde) \xrightarrow{Cannizaro\ rearrangengment} CH_3CH(OH)COOH$	Pharmaceuticals, plastics, industrial cleaning, animal feed additives, food, personal care[107–111]
Glucose	Glucaric acid	Oxidation[88] $C_6H_{12}O_6 \xrightarrow{-2e^-+2H^+} C_6H_{10}O_8$	Pharmaceuticals, corrosion inhibitors, de-icing agents, food additives, detergents, textile industry, personal care[112–114]
Benzyl alcohol	Benzoic acid	Oxidation[95] Benzyl alcohol $\xrightarrow[2OH^-]{-2H_2O,2e^-}$ Benzaldehyde $\xrightarrow[2OH^-]{H_2O,2e^-}$ Benzoic acid Oxidation[96]	Food preservative, chemical industry, pharmaceuticals, industrial products[95,96]
	Benzaldehyde	Benzyl alcohol $\xrightarrow{H^+/-e^-}$ Ketyl radical $\xrightarrow{-2e^-/2H^+}$ Benzaldehyde	Coatings, textiles, food, pharmaceutical intermediates, agrochemicals, cosmetics[95,96]
HMF	FDCA	Oxidation[115] $HMF \xrightarrow[2OH^-]{H_2O+2e^-} HMFCA \xrightarrow[2OH^-]{H_2O+2e^-} FFCA \xrightarrow[2OH^-]{H_2O+2e^-} FDCA$ Reduction[97]	Fine chemicals[115]
CO_2	CO	$CO_2 \xrightarrow{H^++e^-} {}^*COOH \xrightarrow{H^++e^-} {}^*CO \xrightarrow{H^++e^-} CO$ Reduction[97]	Metallurgical, semiconductors, graphene, chemical feedstock, food processing[116–118]
	Formic acid	$CO_2 \xrightarrow{H^++e^-} {}^*OCHO \xrightarrow{H^++e^-} HCOOH$ Reduction[121]	Pharmaceuticals, agriculture, batteries, de-icing agents[119,120]
	Formate	$2CO_2 \xrightarrow{8H^++8e^-} CH_3COOH$ Reduction[97]	Chemical feedstock, pharmaceuticals, textiles, cosmetics[97,121,122]
	Acetic acid		
	Methanol	$CO_2 \xrightarrow{H^++e^-} {}^*COOH \xrightarrow{H^++e^-} {}^*COH \xrightarrow{3(H^++e^-)} CH_3OH$ Reduction[97]	Chemical feedstock, biodiesel production, automotive fuel cells, construction, agriculture, water treatment[123–125]
	Methane		

Table 1 (*Contd.*)

Feedstock	Product(s)	Reaction pathway(s)	Product utilization
		$CO_2 \xrightarrow{H^+ + e^-} *COOH \xrightarrow{H^+ + e^-} *CO$	Fuel, automotive, aerospace, electronics[126–128]
	Ethylene	$*COH \xrightarrow{5(H^+ + e^-)} CH_4$ Reduction[97] $CO_2 \xrightarrow{H^+ + e^-} *COOH \xrightarrow{H^+ + e^-} *COCOH \xrightarrow{H^+ + e^-} *CO \rightarrow *OCCO$ $*CCO \xrightarrow{H^+ + e^-} *CHCO \xrightarrow{H^+ + e^-} *CHCHO \xrightarrow{H^+ + e^-} *CH_2CHO \xrightarrow{3} (H^+ + e^-) C_2H_4$ Reduction[97]	Plastics for packaging, construction, automotive, textiles, agriculture[129–131]
	Ethanol	$CO_2 \xrightarrow{H^+ + e^-} *COOH \xrightarrow{H^+ + e^-} *CO$ $*OCCO \xrightarrow{H^+ + e^-} *COCOH \xrightarrow{H^+ + e^-} *CHCHO$ $*CCO \xrightarrow{H^+ + e^-} *CHCO \xrightarrow{H^+ + e^-} *CHCHO \xrightarrow{H^+ + e^-} *CHCHO$ $*CH_2CHO \xrightarrow{3(H^+ + e^-)} C_2H_5OH$	Bio-based solvents, pharmaceuticals, food, fuel[132,133]

acid not only mitigates greenhouse gas emissions but also provides renewable chemical feedstocks. Surface engineering, including the incorporation of metal single atoms, plasmonic nanoparticles, or molecular catalysts, can steer reaction pathways, in particular towards multi-carbon products, improve CO_2 adsorption, and enhance charge separation.[32]

Table 1 summarizes all the reactions above, which are the target reactions covered in this review. The table includes the reactants, products, reaction pathways, and, most importantly, their corresponding product utilizations.

3. Surface engineering for selectivity control in PEC biomass valorization

The surface properties of photoelectrodes play a fundamental role in determining the reactivity, efficiency, and selectivity of PEC biomass conversion. While optical and electronic modifications are commonly employed to regulate charge carrier dynamics, molecular adsorption is collectively governed by surface composition, wettability, and geometry. By precisely tuning these properties, it is possible to promote the preferential binding of target molecules while suppressing undesired competitive adsorption.[134–136] In this section, we comprehensively discuss various surface engineering strategies, such as surface functionalization, crystal facet tuning, defect engineering, and nanostructuring, that enhance selectivity in PEC biomass and CO_2 valorization. While examples specific to biomass valorization are available, they remain somewhat limited; we therefore also draw insights from PEC CO_2 reduction systems, where a similar selectivity limitation exists and analogous surface engineering approaches (*e.g.*, active site control and interfacial modulation) have been more extensively studied. The discussed strategies offer precise control over active sites, charge transfer, and interactions with complex biomass feedstocks, enabling optimized reaction pathways for improved selectivity.

3.1. Surface functionalization

Surface functionalization plays a pivotal role in tailoring photoelectrode properties to enhance both the efficiency and selectivity of PEC biomass and CO_2 valorization.[137–139] This section delves into various surface engineering strategies, including the incorporation of nanoparticles, quantum dots, single-atom metals, layered double hydroxides, and molecular co-catalysts. Each approach offers unique advantages in optimizing light absorption, promoting charge separation, providing abundant active sites, and precisely tuning reaction pathways to achieve desired products. By decorating the surface of photoelectrodes, these strategies overcome limitations such as charge recombination and non-selective reactions, paving the way for more efficient and selective PEC conversion processes.

3.1.1. Nanoparticles. Incorporating metal or metal compound nanoparticles (NPs) is a widely adopted strategy to utilize heterostructuring in PEC systems.[140] One interesting phenomenon is localized surface plasmon resonance (LSPR),

where incident light excites collective oscillations of conduction electrons in metal NPs.[141] This unique property allows metal NPs to concentrate electromagnetic energy at their surfaces, generating "hot spots" that enhance light absorption and amplify localized electromagnetic fields.[142–145] These effects significantly boost photocatalytic activity by increasing the number of photogenerated charge carriers available for PEC reactions. Additionally, the LSPR effect enables metal NPs to extend the system's light absorption spectrum into the visible and near-infrared regions, further improving PEC performance.[146–148] Finally, the LSPR effect may also drive the selectivity of PEC biomass and CO_2 valorization reactions through the modification of the energetic landscape induced by the enhanced electromagnetic field.[35,149]

One strategy to leverage NPs for enhancing PEC biomass valorization selectivity is utilizing them as efficient light harvesters. By channeling additional energy into an already selective photoelectrode, metal NPs facilitate the generation of high-energy charge carriers, promoting improved PEC activity.[150] This approach is commonly employed, often using simple deposition techniques such as drop-casting.[151,152] For instance, Au_3Cu NPs have been shown to enhance the PEC performance of CO_2 reduction on Si nanowires, improving the faradaic efficiency (FE) for CO to nearly 80% under illumination.[153] Another example involves loading Ag NPs onto TiO_2, leading to an increase in the FE of CO_2-to-formic acid (FA) conversion from 52% in the absence of illumination to 73% under light exposure (Fig. 4a).[154] This increase in FE is analogous to the enhanced current density and light absorption, indicating the effectiveness of the deposited NPs in improving charge transfer and acting as a light harvester. However, optimizing the deposited NP concentration is crucial in this
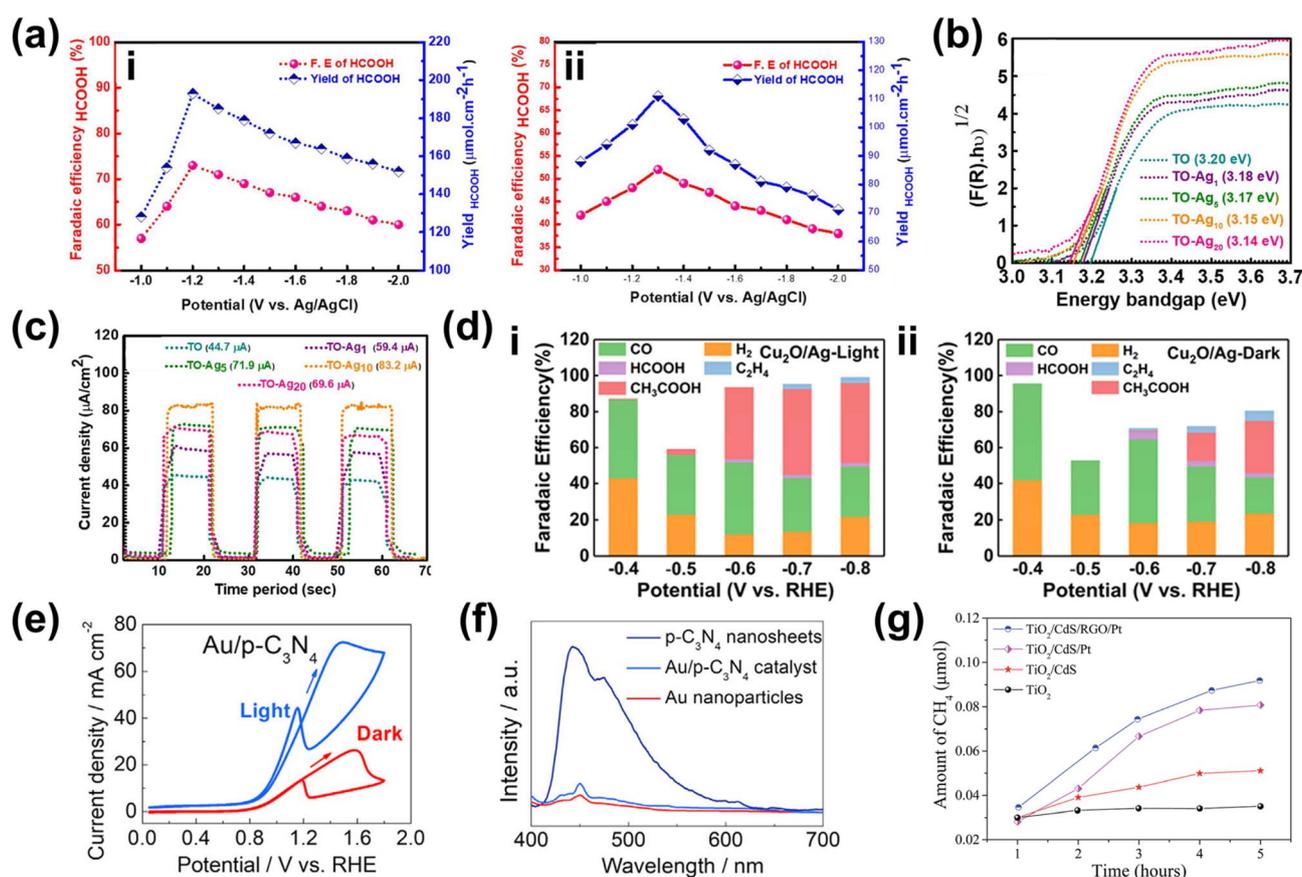

Fig. 4 NPs in enhancing selectivity through light harvesting and charge transfer enhancement. (a) FE and yield of formate on TiO_2–Ag NP photoelectrodes (i) with and (ii) without light illumination. (b) Tauc plot comparing the optical bandgap of bare TiO_2 and Ag NP-decorated TiO_2. (c) Photocurrent density of TiO_2–Ag NP photoelectrodes with varying Ag NP concentrations. The photocurrent density shows an increasing trend up to 20 mM (TiO_2–Ag_{20}), beyond which a decline is observed despite a reduced bandgap. Adapted from ref. 154 with permission. Copyright 2022 The Korean Society of Industrial and Engineering Chemistry. (d) FE of products on the CuO_2/Ag NP photoelectrode at different applied biases (i) with and (ii) without light illumination. Under illumination, multi-carbon products, acetic acid (CH_3COOH, red) and ethylene (C_2H_4, blue), dominate. A lower potential is required to achieve the increase in selectivity when the reaction is conducted under light illumination. Adapted from ref. 154 with permission. Copyright 2022 The Royal Society of Chemistry. (e) Cyclic voltammetry of Au NPs/p-C_3N_4 photoelectrodes under dark and illuminated conditions. (f) Photoluminescence spectra of p-C_3N_4 nanosheets, the Au NPs/p-C_3N_4 catalyst, and Au NPs. The decrease in light emission around the 460 nm wavelength indicates that the interface electric field of the resulting Au NPs/p-C_3N_4 heterojunction effectively separates the photogenerated charge carriers. Adapted from ref. 158 with permission. Copyright 2021 Elsevier Inc. (g) Methane production from photocatalytic CO_2 reduction in the presence of water on bare and modified TiO_2 photoelectrodes. Reproduced from ref. 159 with permission. Copyright 2015 The Royal Society of Chemistry.

strategy. Varying the Ag NP loading on TiO_2 results in distinct absorption bands (Fig. 4b), indicating changes in the system's (apparent) bandgap.[155] While increased NP concentration reduces the bandgap and enhances charge transfer capability, excessive deposition can lead to agglomeration, reducing the active surface area and negatively impacting performance (Fig. 4c).[156] A similar enhancement under illumination is observed when Ag NPs are deposited onto Cu_2O nanowires using vacuum thermal evaporation.[157] This method improves CO_2 reduction selectivity and increases the overall yields of multi-carbon products (Fig. 4d).

Beyond enhancing light absorption, another strategy for leveraging NPs in PEC systems involves their role in promoting charge separation, by acting as electron reservoirs or sinks. This function is critical in reducing charge recombination losses and ensuring selective transfer of photogenerated carriers to targeted reaction sites. For instance, PEC glycerol oxidation on polymeric C_3N_4 (p-C_3N_4) nanosheets exhibits a significant performance enhancement upon incorporating Au NPs.[158] In this case, the interaction between Au NPs and p-C_3N_4 suppresses charge carrier recombination while promoting the accumulation of photogenerated holes on the NPs. These synergistic effects result in a higher current density (Fig. 4e) and a suppressed photoluminescence signal around 460 nm (Fig. 4f). A promising extension to this strategy involves employing multiple types of NPs. For example, TiO_2/CdS and Pt NPs have been integrated onto reduced graphene oxide (rGO) to enhance the CO_2-to-methane yield.[159] Here, TiO_2 predominantly absorbs in the UV region, limiting the PEC performance. However, this limitation is mitigated by incorporating CdS, which extends the light absorption into the visible range. Moreover, introduction of Pt NPs further enhances methane production (Fig. 4g), attributed to the synergistic effect of the NPs and rGO in photogeneration, charge separation, and carrier transport. Upon exposure to visible light, electron–hole pairs are generated in both semiconductors. Due to the specific band alignment at the TiO_2/CdS interface, photogenerated electrons transfer to the CB of TiO_2, while holes remain in the VB of CdS. This spatial separation of charge carriers reduces recombination. Additionally, rGO, a well-known electron-accepting material with excellent conductivity due to its two-dimensional planar structure, facilitates rapid charge transfer. This efficient transport of charge carriers across the graphene sheets further enhances charge separation, ultimately suppressing the electron–hole recombination.

In terms of selectivity control, NPs can be employed to promote specific reaction pathways. The enhanced electromagnetic field near the plasmonic surface lowers activation energy for certain reactions, selectively stabilizing key intermediates or transition states.[35,149] Additionally, plasmonic "hot spots" enhance the adsorption of biomass molecules near active sites, improving surface interactions and reaction kinetics.[160–162] By selectively strengthening the interaction energy between the plasmonic surface and specific functional groups, these NPs drive targeted reactions with high precision. In this context, the impact of NPs on the selectivity of PEC reactions has been well demonstrated. For instance, in PEC glycerol oxidation, the incorporation of Au NPs on p-C_3N_4 enhances selectivity toward dihydroxyacetone (DHA).[158] In this approach, a chemical reduction method was used to evenly distribute the NPs on the C_3N_4 photoelectrode. Calculations reveal that the potential energy for middle hydroxyl oxidation is higher than that for the terminal hydroxyl (Fig. 5a), resulting in selective dehydrogenation and oxidation of glycerol to DHA with a selectivity of up to 53.7% (Fig. 5b). Beyond Au NP-modified systems, Bi-based NPs have also shown remarkable potential in tuning PEC glycerol oxidation selectivity, particularly toward DHA.[163] A notable example involves the *in situ* reduction of WO_3/$BiVO_4$ using hydrazine hydrate to produce a WO_3/$BiVO_4$/Bi NP photoanode, which achieves a DHA selectivity of up to 60.6%, surpassing the 53.3% observed for bare WO_3/$BiVO_4$ (Fig. 5c). This process reduces Bi^{3+} in $BiVO_4$ to metallic Bi^0, forming Bi^0/Bi^{3+} active sites (Fig. 5d). The hydrazine reduction is carefully controlled to prevent over-reduction, which could compromise the structural integrity of the composite. The improved selectivity is attributed to the enhanced affinity of the $BiVO_4$/Bi NP surface for the middle hydroxyl of glycerol, with the NPs further promoting adsorption. DFT calculations confirm that glycerol's terminal and middle hydroxyl groups (*i.e.*, primary and secondary –OH, respectively) preferentially adsorb onto Bi^0 sites at the Bi^0/Bi^{3+} interface. The rate-limiting step in this process is carbon-centered radical formation *via* photogenerated hole-driven dehydrogenation. The activation barrier for middle-carbon radical formation is lower than that for terminal radicals, resulting in the mechanism that favors DHA production. A similar trend is observed in Bi_2O_3 NP-modified TiO_2 photoanodes. In this system, Bi is first electrodeposited onto TiO_2, followed by electro-oxidation to form a Bi_2O_3/TiO_2 heterojunction (Fig. 5e).[164] This structure achieves an impressive glycerol-to-DHA selectivity of 75.4%. The Bi_2O_3 NPs exhibit low DHA adsorption capability, preventing further oxidation and contributing to high selectivity. Additionally, the Bi_2O_3/TiO_2 heterojunction has enhanced charge transfer and photogenerated hole utilization due to the formation of a p–n junction. The important role of the Bi_2O_3 NPs in tuning selectivity is evident from the fact that bare TiO_2 favors FA formation instead; although FA is another high-value glycerol derivative, its market price is far below that of DHA.

Beyond glycerol oxidation, selectivity tuning through the incorporation of NPs has also been demonstrated for PEC CO_2 reduction. Similar to glycerol oxidation, NPs can serve as adsorption centers for CO_2 molecules, selectively adsorbing key intermediates that directly influence reaction selectivity—particularly toward single-carbon products.[165] To tune the reaction selectivity toward CO, the system must be engineered to promote CO_2 activation into *COOH and facilitate *CO desorption. In this regard, employing Au NPs[166] and AgCu bimetallic NPs[167,168] has proven to be highly effective for achieving high selectivity in the CO_2 reduction reaction toward CO. For the former, electrodeposited Au NPs exhibit a synergistic effect with TiO_2 (Fig. 6a), jointly enhancing CO_2 adsorption and promoting the kinetics of CO production by accelerating both the *COOH formation step and the subsequent desorption of *CO from active sites. This results in an
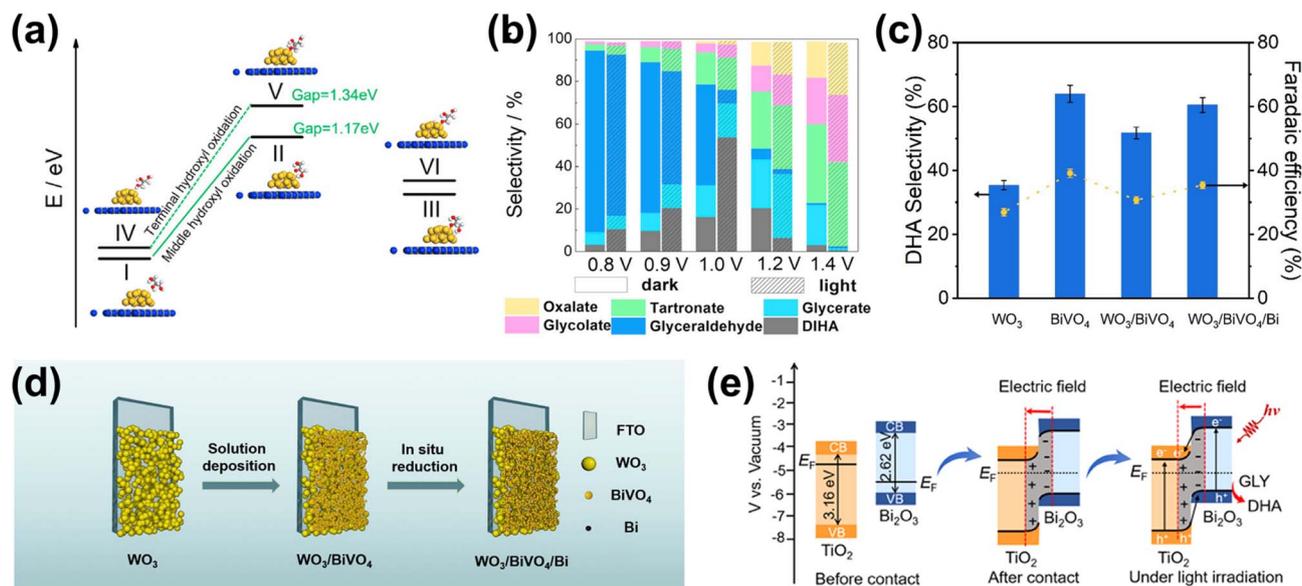
Fig. 5 NP-assisted selectivity tuning in PEC glycerol oxidation. (a) Potential energy for the oxidation of terminal and middle hydroxyls of glycerol on the Au NPs/p-C_3N_4 photoelectrode. The adsorption energies of middle and terminal hydroxyls are calculated to be −1.42 eV and −1.27 eV, respectively, which are higher than that of pristine p-C_3N_4. The theoretical calculations of the oxidation potential energy and adsorption energy are consistent with the heightened selectivity of the Au NPs/p-C_3N_4 photoelectrode towards DHA. (b) Product selectivity for glycerol oxidation on Au NPs/p-C_3N_4 at various potentials with and without light illumination. The maximum selectivity of DHA (gray) is achieved at 1.0 V_{RHE} potential under light illumination. Adapted from ref. 158 with permission. Copyright 2021 Elsevier Inc. (c) DHA selectivity and FE on pristine WO_3, $BiVO_4$, and modified photoelectrodes. The reaction is conducted under light illumination and 1.2 V_{RHE} applied bias in 0.5 M Na_2SO_4 with glycerol. Adapted from ref. 163 with permission. Copyright 2023 The Royal Society of Chemistry. (d) Fabrication steps of the $WO_3/BiVO_4/Bi$ NP photoanode. (e) Energy band diagram of Bi_2O_3 and TiO_2, along with the proposed mechanism for PEC glycerol oxidation in the Bi_2O_3/TiO_2 p−n junction under illumination. Adapted from ref. 164 with permission. Copyright 2022 American Chemical Society.

improved FE for CO, reaching 86% (Fig. 6b). Alternatively, the use of AgCu NPs offers a unique tunability mechanism based on composition modulation. The AgCu NPs are embedded onto a p-Si film *via* immersion in an HF solution containing Ag^+ and Cu^{2+} ions (Fig. 6c). The reaction is more selective towards CO when Ag is the dominant component, and the selectivity shifts to methane when Cu is introduced (Fig. 6d(i and ii)). This tunability through the modulation of Ag and Cu ratio in the NPs arises from the electronic and geometrical effects generated by the nanoscale coupling of the two metals. On the one hand, Ag is responsible for the reduction of CO_2 to CO and on the other, Cu continues the reduction process to single or multi-carbon. It is also important to highlight that the geometric structure plays a crucial role in tuning the reaction selectivity. In this case, the selectivity towards the single-carbon product, methane, rather than multi-carbon products, is possible due to the presence of intermixed Ag and Cu domains, which preferentially produce methane. Additionally, similar selectivity modulation is observed when NPs are embedded onto p-Si micropillars.

Formate is another valuable single-carbon product of PEC CO_2 reduction. To tune the reaction toward formate, it is essential to stabilize *OCHO and *HCOOH intermediates while reducing the desorption energy of *HCOOH. Cu-based NPs are particularly effective for this purpose.[169,170] In this process, chemisorbed CO_2 attracts protons from the electrolyte, forming a chemisorbed HCOO radical *via* a stable *OCHO intermediate. Electron transfer to this radical species leads to formate

desorption. Additionally, CO_2 radicals at Cu active sites can react with surface-bound H atoms to generate formate. This strategy has been successfully demonstrated through the integration of Cu NPs into Co_3O_4 nanotube arrays and p-NiO films. In the first case, Cu NPs are electrodeposited onto nanotube arrays, yielding 6.75 mmol L^{-1} cm^{-2} of formate over 8 hours of reaction with nearly 100% selectivity (Fig. 6e). In the second case, a 3 nm Cu layer is deposited onto a p-NiO film *via* electron-beam physical vapor deposition, resulting in a formate FE of at least 20% (Fig. 6f(i and ii)). Notably, bare p-NiO exclusively produces H_2 with an FE of 98%, underscoring the crucial role of Cu NPs in selectively tuning the reaction toward formate.

For PEC CO_2 reduction to multi-carbon products, the corresponding selectivity largely depends on the specific ability of the metal NPs to facilitate carbon–carbon (C–C) coupling. Notably, Cu is the only known metal thus far capable of catalyzing this crucial step. One example of utilizing Cu NPs for this purpose involves incorporating them into Si nanowires (Fig. 7a(i and ii)) *via* a drop-casting method.[171] This approach enables the selective conversion of CO_2 to ethylene for up to 50 hours while maintaining a FE above 15% (Fig. 7b). Moreover, increasing the Cu loading further enhances this selectivity (Fig. 7c). However, excessive Cu deposition leads to NP accumulation at the base of the nanowire arrays, which leads to agglomeration and decreased active surface area,[172] negatively impacting the conversion performance. Additionally, AuCu bimetallic NPs can be integrated with photoelectrodes to achieve selective PEC CO_2
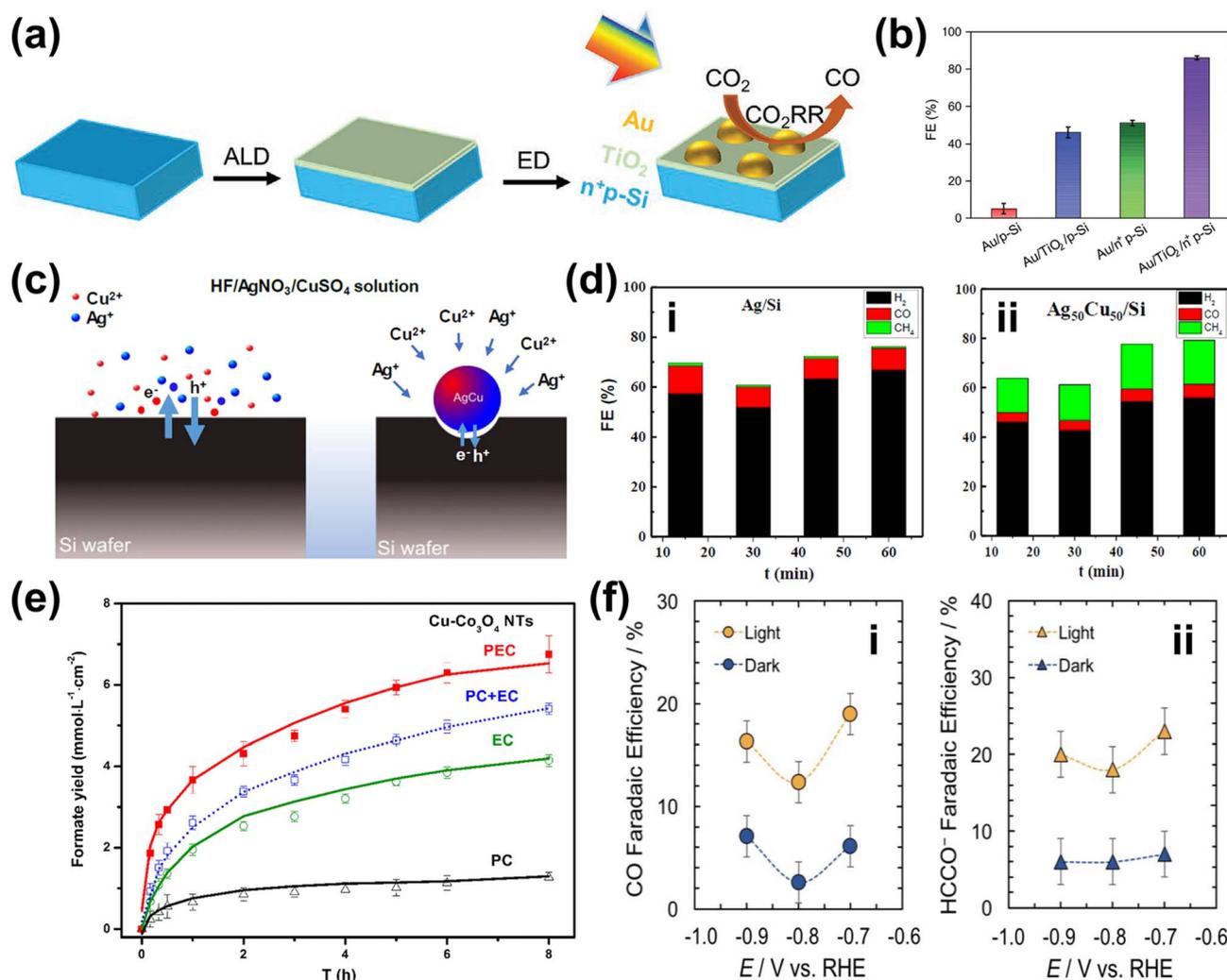
Fig. 6 NP-enabled selectivity tuning in PEC CO_2 reduction toward single-carbon products and other biomass valorization reactions. (a) Fabrication process of the Au NPs/TiO_2/n^+p-Si photoelectrode. (b) FE for CO at -0.4 V_{RHE} on Au NP-modified p-Si photoelectrodes. Adapted from ref. 166 with permission. Copyright 2022 Wiley-VCH GmbH. (c) Schematic illustration of AgCu NP formation and deposition on a Si wafer *via* metal-assisted chemical etching. Ag^+ and Cu^{2+} ions are spontaneously reduced upon contact with the Si surface, extracting electrons from the Si valence band and forming Ag^0 and Cu^0 nuclei. HF solution facilitates Si dissolution, creating a porous structure that supports ion reduction and NP growth. (d) FE of PEC CO_2 reduction products on (i) Ag and (ii) AgCu NP-modified Si photoelectrodes. Adapted from ref. 167 with permission. Copyright 2023 American Chemical Society. (e) Performance of Cu NPs on the Co_3O_4 NT photoelectrode for selective CO_2 reduction to formate. Adapted from ref. 169 with permission. Copyright 2015 American Chemical Society. (f) Performance of Cu NPs on the p-NiO film to selectively reduce CO_2 to (i) CO and (ii) formate. Adapted from ref. 170 with permission. Copyright 2020 American Chemical Society.

reduction to ethanol.[173] While Cu facilitates C–C coupling, Au plays a critical role in modifying the binding energies of key reaction intermediates, such as *CH_2CHO, *CH_3CHO, and *CH_3CH_2O, thereby contributing to the reaction selectivity. However, to the best of our knowledge, this strategy has only been demonstrated in electrocatalysis, where the NPs are deposited on Cu submicrocone arrays (Cu SCAs) *via* an *in situ* reduction method. Nevertheless, this approach presents a promising pathway for achieving selective PEC CO_2 reduction to multi-carbon products.

In conclusion, the examples discussed above highlight the ability of NPs to enhance and tune PEC biomass and CO_2 valorization selectivity. In particular, they concentrate

electromagnetic energy on their surfaces, generating "hot spots" that enhance light absorption and amplify localized electromagnetic fields, in turn boosting photocatalytic activity by increasing photogenerated charge carriers available for PEC reactions. Additionally, NPs extend the system's light absorption spectrum into the visible and near-infrared regions, further improving PEC performance. They also act as efficient light harvesters, channeling additional energy into selective photoelectrodes to promote improved PEC activity. Beyond light absorption, NPs promote charge separation by acting as electron reservoirs or sinks, which is critical in reducing charge recombination losses and ensuring selective transfer of photogenerated carriers to targeted reaction sites. In the context
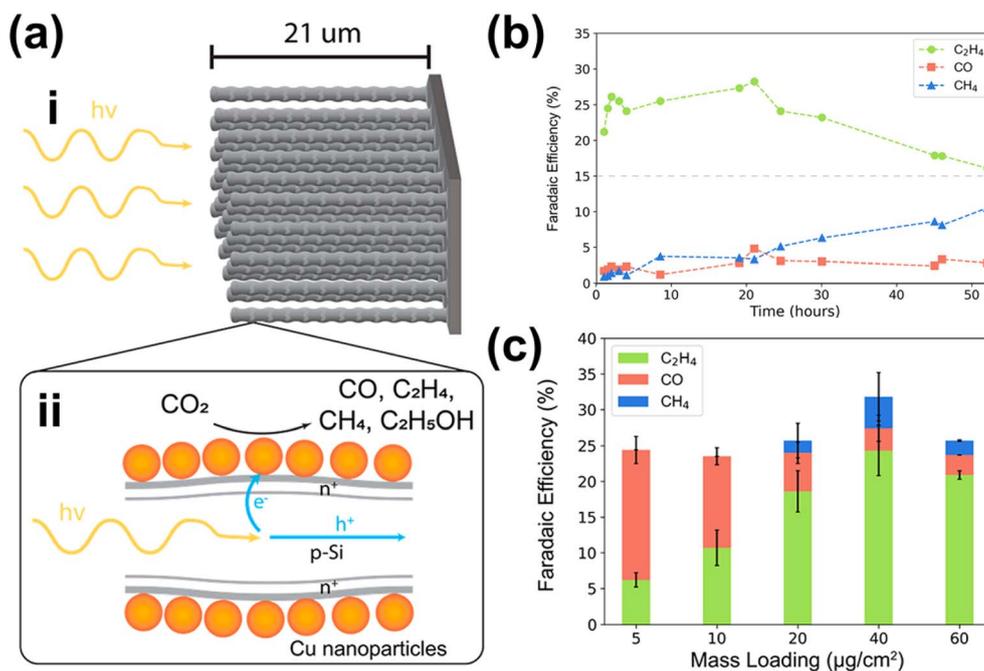
Fig. 7 NP-enabled selectivity tuning in PEC CO_2 reduction toward multi-carbon products. (a) Cu NPs/Si NW photocathode: (i) illustration and (ii) PEC reaction mechanism. (b) PEC CO_2 reduction performance of the Cu NPs/Si NW photocathode over 50 h. (c) FE of PEC CO_2 reduction products as a function of Cu NP loading. Adapted from ref. 171 with permission. Copyright 2022 American Chemical Society.

of selectivity tuning, the enhanced electromagnetic field near the plasmonic surface lowers activation energy for certain reactions, selectively stabilizing key intermediates or transition states. NPs also enhance the adsorption of biomass molecules near active sites, improving surface interactions and reaction kinetics. Given their versatility, decorating photoelectrodes' surface with NP cocatalysts holds significant potential for selectivity tuning and enhancement in a broad range of PEC reactions, including methane oxidation,[174,175] ethanol oxidation,[176] and nitrate reduction.[177] However, a crucial consideration with NP surface functionalization relates to its concentration optimization, as excessive deposition can lead to agglomeration, which subsequently reduces the active surface area and negatively impacts performance. A summary of the role of NPs in enhancing and tuning PEC reaction selectivity is presented in Table 2.

3.1.2. Quantum dots. Heterostructuring with quantum dots (QDs) offers a transformative approach to increasing both conversion efficiency and selectivity in PEC of biomass. QDs are known for their size-tunable bandgap and high surface area-to-volume ratio, which could provide unique electronic and optical properties to influence reaction pathways.[178] Distributing QDs onto photoelectrode surfaces often results in the introduction of additional energy levels in the heterostructure.[20,179,180] These energy levels may be better aligned with the redox potentials of substrate molecules and/or biomass-derived intermediates. Additionally, QDs exhibit strong light absorption across a wide light spectrum.[181–183] Hence, its presence can also boost the light harvesting ability of the overall photoelectrodes and improve conversion efficiency. Due to their small size, infiltrating and

decorating the often-intricate photoelectrode morphologies (*e.g.*, nanostructured or porous) are possible. QDs can also function as co-catalysts in PEC biomass valorization.[37,180,184] In this case, QDs can facilitate specific reaction pathways by acting as active sites for the adsorption and activation of reactants or intermediates. Their tunable surface properties and ability to generate a high density of reactive sites also enable precise modulation of the reaction environments.[185,186] Moreover, their strong quantum confinement effect can create highly reactive electronic states that selectively interact with specific functional groups in complex biomass molecules.[187,188] By serving as co-catalysts, QDs not only enhance the photocatalytic efficiency of PEC systems but also ensure a higher degree of control over product distribution, making them an invaluable component in the selective valorization of biomass. Another impact is enhanced selectivity through the QDs' ability to generate localized surface states that interact preferentially with certain intermediates.[37,189–191] Last, the introduction of QDs can lead to direct photogenerated electrons or holes toward specific reaction sites by modulating the local electronic environment of the photoelectrodes.[192,193] This effect ensures that the energy from charge carriers is channeled efficiently into selective reaction pathways, thereby reducing side reactions.

A common application for surface engineering with QDs found in the literature is in PEC CO_2 reduction systems. In such a case, integrating QDs to form a metal-insulator-semiconductor (MIS) structure offers a promising strategy by improving charge transfer and providing abundant active sites, thereby enhancing catalytic activity and selectivity for the PEC reaction.[194–196] One example is the $Ag_3Cu/TiO_2/ZnTe$ QD

Table 2 Summary of nanoparticle (NP) utilization on the surface of photoelectrodes for PEC biomass valorization selectivity enhancement and tuning applications

| Photoelectrode[a]	NP role	Deposition method	Reaction	Target product(s)	Selectivity	FE	Reaction conditions	Ref.
Au$_3$Cu NPs/Si NW	Light harvester	Drop-casting	CO$_2$ reduction	CO	N/A	80%	• Electrolyte: CO$_2$-saturated KHCO$_3$ (0.1 M, pH 6.8) • Applied bias: −0.2 V$_{RHE}$ • Light: AM 1.5G (100 mW cm^{-2})	153
TiO$_2$–Ag NPs	Light absorption and charge transport promoter	Immersion and calcination	CO2 reduction	FA	N/A	73%	• Electrolyte: CO$_2$-saturated K$_2$SO$_4$ (0.5 M) • Applied bias: −1.2 V$_{Ag/AgCl}$ • Light: 300 W Xe lamp	154
Cu$_2$O NW/Ag NPs	Light harvester and charge separation promoter	Vacuum thermal evaporation	CO$_2$ reduction	Acetic acid	N/A	47.7%	• Electrolyte: CO$_2$-saturated KHCO$_3$ (0.1 M) • Applied bias: −0.7 V$_{RHE}$ • Light: AM 1.5G (100 mW cm^{-2})	157
Au NPs/C$_3$N$_4$	Promoting middle hydroxyl oxidation, charge transfer and separation promoter, light harvester	Immersion	Glycerol oxidation	DHA	53.7%	N/A	• Electrolyte: KOH (1 M) with glycerol (1 M) • Applied bias: 1.0 V$_{RHE}$ • Light: AM 1.5G	158
WO$_3$/BiVO$_4$/Bi NPs	Middle hydroxyl adsorption site, light harvester, charge transport promoter	In situ reduction	Glycerol oxidation	DHA	60.6%	N/A	• Electrolyte: Na$_2$SO$_4$ (0.5 M, pH 2) with glycerol (0.1 M) • Applied bias: 1.2 V$_{RHE}$ • Light: AM 1.5G (100 mW cm^{-2})	163
Bi$_2$O$_3$ NPs/TiO$_2$ NRAs	Middle hydroxyl adsorption site and charge transfer promoter	Electrodeposition and electro-oxidation	Glycerol oxidation	DHA	75.4%	N/A	• Electrolyte: Na$_2$SO$_4$ (0.5 M, pH 2) • Applied bias: 1.0 V • Light: AM 1.5G (100 mW cm^{-2})	164
TiO$_2$ NTs/CuO NPs	CO$_2$ adsorption site, charge transport and separation promoter	Dip-coating	CO$_2$ reduction	Methanol	N/A	57%	• Electrolyte: K$_2$SO$_4$ (0.1 M, pH 8) • Applied bias: 0.2 V$_{Ag/AgCl}$ • Light: UV-visible	165
Au NPs/TiO$_2$/n$^+$p-Si	Light harvester, charge separation and transport promoter, promoting COOH* formation and CO desorption	Electrodeposition	CO$_2$ reduction	CO	N/A	86%	• Electrolyte: CO$_2$-saturated KHCO$_3$ (0.1 M) • Applied bias: −0.4 V$_{RHE}$ • Light: AM 1.5G (100 mW cm^{-2})	166
Ag NPs/p-p-Si	Light harvester, reaction and adsorption center	Metal-assisted chemical etching	CO$_2$ reduction	CO	N/A	10%	• Electrolyte: CO$_2$-saturated NaHCO$_3$ (0.5 M) • Applied bias: −0.87 V$_{RHE}$ • Light: AM 1.5G (100 mW cm^{-2})	167

Table 2 (Contd.)

Photoelectrode[a]	NP role	Deposition method	Reaction	Target product(s)	Selectivity	FE	Reaction conditions	Ref.
AgCu NPs/p-Si	Light harvester, reaction and adsorption center	Metal-assisted chemical etching	CO_2 reduction	Methane	N/A	18.2%	• Electrolyte: CO_2-saturated $NaHCO_3$ (0.5 M) • Applied bias: −0.87 V_{RHE} • Light: AM 1.5G (100 mW cm^{-2})	167
Ag NPs/Si MPs	Light harvester, reaction and adsorption center	Metal-assisted chemical etching	CO_2 reduction	CO	N/A	12.1%	• Electrolyte: CO_2-saturated $NaHCO_3$ (0.5 M) • Applied bias: −0.87 V_{RHE} • Light: AM 1.5G (100 mW cm^{-2})	168
AgCu NPs/Si MPs	Light harvester, reaction and adsorption center	Metal-assisted chemical etching	CO_2 reduction	CO and methane	N/A	16.7% (CO) and 9% (methane)	• Electrolyte: CO_2-saturated $NaHCO_3$ (0.5 M) • Applied bias: −0.87 V_{RHE} • Light: AM 1.5G (100 mW cm^{-2})	168
Cu NPs-Co_3O_4 NTs	CO_2 adsorption and formate desorption sites	Electrodeposition	CO_2 reduction	Formate	100%	N/A	• Electrolyte: CO_2-saturated Na_2SO_4 (0.1 M) • Applied bias: −0.9 V_{SCE} • Light: 10 mW cm^{-2}	169
Cu NPs/p-NiO	CO_2 adsorption and activation to CO_2^- sites	Electron-beam physical vapor deposition	CO_2 reduction	Formate	N/A	20%	• Electrolyte: CO_2-saturated K_2CO_3 (0.05 M) • Applied bias: −0.7 V_{RHE} • Light: 160 mW cm^{-2}	170
Cu NPs/Si NWs	C–C coupling catalyst	Drop-casting	CO_2 reduction	Ethylene	N/A	25%	• Electrolyte: CO_2-saturated $KHCO_3$ (0.1 M) • Applied bias: −0.5 V_{RHE} • Light: AM 1.5G (100 mW cm^{-2})	171
AuCu NPs/Cu SCAs	C–C coupling catalyst and CH_2CHO^*, CH_3CHO^*, and $CH_3CH_2O^*$ intermediate adsorption sites	In situ reduction	CO_2 reduction	Ethanol and ethylene	N/A	29% (ethanol) and 16% (ethylene)	• Electrolyte: CO_2-saturated $KHCO_3$ (0.5 M) • Applied bias: −1.0 V_{RHE} (ethanol) and −1.1 V_{RHE} (ethylene)	173
TiO_2/MOF(Ti)/Au NPs	Increasing surface roughness and light harvester	Photochemical	Methane oxidation	Methanol	N/A	65.32%	• Light: no information • Electrolyte: Na_2SO_4 (0.1 M) • Applied bias: 0.5 V_{RHE} • Light: AM 1.5G (100 mW cm^{-2})	174

[a] MP: micropillar, NP: nanoparticle, NRA: nanorod array, NT: nanotube, NW: nanowire, and SCA: submicrocone array.
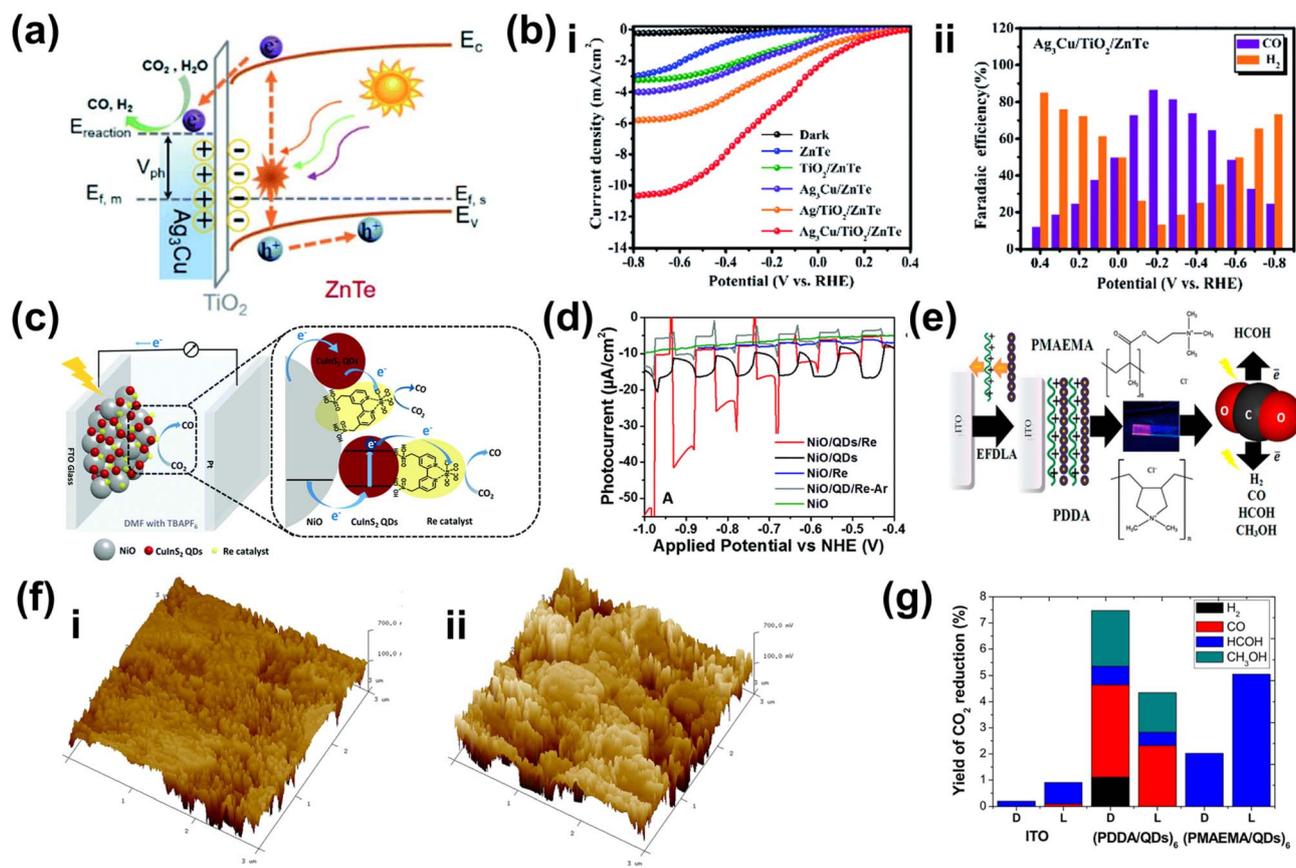
Fig. 8 QDs as a co-catalyst for improved selectivity of the PEC CO_2 reduction reaction. (a) Band diagram of the $Ag_3Cu/TiO_2/ZnTe$ QD photocathode. The Ag_3Cu NCs serve as a metallic collector on a TiO_2-coated ZnTe QD semiconductor film. The diagram highlights key energy levels, including the conduction band (E_0), valence band (E_V), Fermi level of ZnTe ($E_{f,s}$), Fermi level of the metal ($E_{f,m}$), and the potential values of relevant chemical reactions ($E_{reaction}$), providing insight into the charge transfer mechanism and photocatalytic activity of the system. (b) PEC CO_2 reduction performance of the $Ag_3Cu/TiO_2/ZnTe$ QD photocathode shown as (i) the comparison of photocurrent density and (ii) the FE of CO and H_2 production on the photocathode as a function of the applied bias. Adapted from ref. 197 with permission. Copyright 2021 The Royal Society of Chemistry. (c) The schematic representation of a PEC cell designed for CO_2 reduction featuring a NiO photocathode co-modified with $CuInS_2$ QDs and a Re catalyst. (d) Linear-sweep voltammetry curves of the NiO photocathode recorded for various samples under chopped light illumination. Adapted from ref. 199 with permission. Copyright 2019 The Royal Society of Chemistry. (e) Schematic diagram of the electric field-directed layer-by-layer assembly on an ITO substrate under an applied potential of 1000 mV. This process involves the deposition of strong polycations with distinct structural differences—cyclic versus branched monomer structures—which influence the assembly mechanism. These structural variations can impact key factors such as the growth dynamics and adsorption kinetics of the multilayers, ultimately affecting the overall stability and performance of the assembled film. (f) 3-Dimensional AFM phase imaging of (i) ITO-$(PDDA/QDs)_6$ and (ii) ITO-$(PMAEMA/QDs)_6$ surfaces. (g) CO_2 reduction product yields obtained by potential controlled electrolysis under dark conditions (D) and light irradiation (L) over 3 h with −450 mV applied bias. Adapted from ref. 200 with permission. Copyright 2015 American Chemical Society.

structure for the CO_2 reduction reaction to CO.[197] Through this design, the MIS structure effectively couples interfacial charge transport, surface reaction processes, and long-term stability, offering a robust PEC photocathode design. Under light irradiation, the ZnTe QDs absorb photons, generating minority electrons that tunnel through the TiO_2 layer to the Ag_3Cu nanocrystals (NCs), where reduction reactions involving CO_2 or H^+ occur (Fig. 8a). Furthermore, the ultrathin TiO_2 layer reduces surface defects on the ZnTe film and minimizes charge recombination. Overall, this strategy leads to significant performance enhancements, as demonstrated by the $Ag_3Cu/TiO_2/ZnTe$ photocathode achieving a photocurrent density of −10.68 mA cm^{-2} at −0.8 V_{RHE} (Fig. 8b (i)) and a maximum FE of 86.5% for CO at −0.2 V_{RHE} (Fig. 8b(ii)). However, despite its

effectiveness, this approach is often associated with high costs.[198] As a cost-effective alternative, immersion techniques can instead be employed. One example utilizes $CuInS_2$ QDs along with Re catalysts to serve as photosensitizers on NiO photocathodes for selective PEC CO_2 reduction to CO (Fig. 8c).[199] Specifically in this approach, the $CuInS_2$ QDs were directly synthesized from an aqueous solution using L-cysteine immobilized on a 1 mm thick NiO electrode by immersion. This method yields small molecular sizes, allowing more penetration into mesoporous NiO films and providing more surface coverage. $CuInS_2$ QDs, with a valence band (VB) positioned at 0.5 V and a conduction band (CB) at −1.3 V_{NHE}, can thermodynamically transfer photogenerated holes into the VB of NiO, allowing efficient charge separation and reaction progression.

Additionally, the CB of $CuInS_2$ facilitates efficient electron transfer to the Re catalysts due to the more negative reductive potential of the QDs. A PEC CO_2 reduction test shows that the deposited $CuInS_2$ QDs significantly enhance the photocurrent, as shown in Fig. 8d, albeit with a relatively low CO_2 to CO FE of 32% at -0.87 V_{NHE}. Nevertheless, these examples demonstrate the versatility and capability of QDs as co-catalysts to enhance the selectivity of PEC CO_2 reduction to CO.

Adding to the versatility of QD utilization for the PEC CO_2 reduction reaction, incorporating QDs onto electrode surfaces through bondage with polymers or biomolecules unveils opportunities to tune the selectivity of the reaction. In particular, electrostatic assembly can be achieved using an electric field-driven layer-by-layer deposition of polycations, such as poly(diallyldimethylammonium) (PDDA) and poly(2-trimethylammonium)ethyl methacrylate (PMAEMA) (Fig. 8e).[200] It is later revealed that the former sample exhibits a higher structural profile (Fig. 8f (i)), whereas the latter displays higher average roughness (Fig. 8f(ii)). This increased roughness is likely associated with a greater presence of microdomain structures due to the incorporation of the PMAEMA polycation. The polycations influence the assembly process and interact with the QDs, resulting in a subtle shift in the onset potential for both electrodes. These shifts enhance intermolecular charge transfer and improve electrocatalytic performance. The photoelectrocatalytic activity of the $(PDDA/QDs)_6$ assembly yielded carbon monoxide, methanol, and smaller amounts of formaldehyde, whereas the $(PMAEMA/QDs)_6$ assembly exclusively produced formaldehyde, emphasizing its selectivity for HCOH formation (Fig. 8g). The distinct reaction products suggest that variations in the surface structure and the resulting interactions between polycations, QDs, and CO_2 molecules drive two distinct reduction pathways, the formaldehyde and carbene pathways.

Based on the discussion above, surface functionalization with QDs serves as a powerful platform for PEC biomass and CO_2 valorization selectivity enhancement and tuning. Their distribution onto photoelectrode surfaces often introduces additional energy levels in the heterostructure, which may more suitably align with the redox potentials of substrate molecules and/or biomass-derived intermediates. QDs also exhibit strong light absorption across a wide spectrum, boosting the overall photoelectrode's light harvesting ability and improving conversion efficiency. Due to their small sizes, QDs can infiltrate and decorate intricate photoelectrode morphologies like nanostructured or porous designs. Their tunable surface properties and ability to generate a high density of reactive sites enable precise modulation of reaction environments. Moreover, their strong quantum confinement effect can create highly reactive electronic states that selectively interact with specific functional groups in complex biomass molecules. In terms of selectivity, QDs are able to generate localized surface states that interact preferentially with certain intermediates. Lastly, the introduction of QDs can direct photogenerated electrons or holes toward specific reaction sites by modulating the local electronic environment of the photoelectrodes, ensuring efficient channeling of energy into selective reaction pathways and reducing side reactions. However, several challenges remain for

the practical deployment of QD-functionalized PEC systems. In colloidal QD-based photoelectrodes, interfacial charge-carrier recombination, limited catalytic selectivity, and poor operational stability in aqueous electrolytes continue to hinder PEC performance.[201] Furthermore, carbon-based QD-sensitized semiconductor systems, in particular, suffer from low efficiency due to small surface area and high energy barriers for charge transport.[202] In the case of CO_2 reduction, systems employing QDs often favor water reduction in carbonated solutions, as its pathway is kinetically more accessible.[203] Despite these limitations, the unique tunability, strong light absorption, and capacity for selective interfacial interactions make QDs a highly promising class of surface modifiers for advancing PEC biomass and CO_2 valorization. The selected utilization of various QDs for PEC biomass and CO_2 valorization and their respective performances are summarized in Table 3.

3.1.3. Single-atom metals. The incorporation of single-atom metals (SAs) onto catalyst surfaces is a cutting-edge strategy for improving both the photoactivity and selectivity of PEC in biomass valorization. Unlike the previous two heterostructuring strategies discussed above, SAs serve as isolated, highly efficient catalytic centers due to their unique electronic and geometric characteristics.[39,204,205] From a photoactivity perspective, SAs profoundly influence the electronic structure of the underlying catalyst.[206] By modulating the bandgap of semiconductors or altering the electronic properties of carbon-based materials, SAs improve light absorption and optimize energy band alignment.[207-209] This modification enhances photogenerated charge carrier separation while minimizing recombination losses, ensuring that more electrons and holes participate in catalytic reactions. Additionally, SAs can act as electron sinks or hole traps, facilitating charge carrier transfer to reactants and accelerating reaction kinetics.[210,211] For instance, Pt SAs anchored on O_{Vac}-rich TiO_2 nanorods (Pt/def-TiO_2 NRAs) have demonstrated exceptional selectivity in glucose oxidation to glucaric acid.[212] Here, TiO_2 underwent electrochemical reduction to introduce O_{Vac}, which then serves as the anchoring site for Pt SAs deposited by atomic layer deposition (Fig. 9a). Furthermore, O_{Vac} in def-TiO_2 enhances charge carrier extraction, as its large electron conduction region and substantial surface band bending promote efficient electron transport. Specifically, extracted electrons migrate to the counter electrode for H_2 production, while the valence band structure of defective TiO_2 optimizes hole energy for glucose oxidation. Following that, Pt SAs facilitate hole transfer to glucose, enabling selective oxidation to glucaric acid. Using this approach, a remarkable glucose conversion is achieved, *i.e.*, 98.8% conversion, with 84.3% selectivity toward glucaric acid—over six times higher than that of bare def-TiO_2 NRAs, which predominantly yield gluconic acid (Fig. 9b). This significant shift in selectivity is attributed to the unique reaction kinetics introduced by Pt SAs. Mechanistically, it was revealed that glucose is initially oxidized to gluconic acid, which then converts into L-guluronic acid before forming glucaric acid (Fig. 9c). On bare def-TiO_2, the charge transfer rate for gluconic acid is 45 s^{-1}, whereas for L-guluronic acid, it is significantly higher at 190 s^{-1}, indicating that the conversion of gluconic

Table 3 Summary of quantum dot (QD) utilization on the surface of photoelectrodes for PEC biomass valorization selectivity enhancement and tuning applications

Photoelectrode	QD role	Deposition method	Reaction	Target product(s)	Selectivity	FE	Reaction conditions	Ref.
Ag₃Cu/TiO₂/ZnTe QDs	Charge separation and transport promoter, light harvester	Spin-coating	CO₂ reduction	CO	6.8 CO : H₂ ratio	N/A	• Electrolyte: CO₂-saturated KHCO₃ (0.1 M, pH 6.8) • Applied bias: −0.2 V_{RHE} • Light: AM 1.5G	197
CuInS₂ QDs/NiO	Charge separation and transport promoter	Immersion	CO₂ reduction	CO	N/A	32%	• Electrolyte: Ar and CO₂-saturated DMF • Applied bias: −1.0 V_{RHE} to −0.4 V_{RHE} • Light: 17 W, Zenaro Lighting GmbH, 420–750 nm	199
PMAEMA/QDs	Charge transport promoter and light harvester	Electric field-driven layer-by-layer	CO₂ reduction	HCOH	100%	N/A	• Electrolyte: CO₂-saturated NaClO₄ (0.1 M) • Applied bias: −0.45 V • Light: 500 W Xe–Hg lamp	200

acid to L-guluronic acid is the rate-limiting step. The incorporation of Pt SAs reduces the charge transfer rate of gluconic acid to 90 s⁻¹, thereby shifting selectivity toward glucaric acid.

Beyond improving charge transfer, SAs' unsaturated coordination environments lead to stronger interactions with reactants and intermediates. These unique active sites enable precise tuning of reaction pathways, significantly improving PEC reaction selectivity.[20] Furthermore, SAs prevent active site aggregation, ensuring uniform activity and precise control over the catalytic process. One example of the effort to harness these properties is by dispersing Ni SAs on silicon nanowires (Si NWs), which allows the photocathode to achieve nearly 100% FE for CO₂ reduction to CO at −0.6 V_{RHE} (Fig. 9d).[213] This high selectivity stems from the unique electronic structure of Ni SAs. Among transition metals, Ni exhibits the lowest thermodynamic barrier for *COOH formation and CO desorption, favoring CO₂ reduction to CO (Fig. 9e). Additionally, the high surface area of Ni SAs dispersed on Si NWs provides abundant reaction sites, further enhancing catalytic performance. In detail, under illumination, electrons in Si are excited from the corresponding VB to CB. When an external bias is applied, electrons from the CB of Si are driven toward Ni SAs, where CO₂ reduction to CO occurs. In addition, Pt SAs can be dispersed on a WO₃ amorphous/crystalline homojunction to selectively oxidize glycerol to DHA.[214] The photoanode is fabricated through the electrochemical reduction of WO₃, followed by immersion in a solution containing 2,2′-bipyridine and Pt cations ([Pt(bpy)]²⁺) and annealing (Fig. 9f). Due to its unique gradient structure, the photoanode exhibits an upward shift in E_F from the inner to the outer layer. This shift generates an internal electric field that, upon illumination, drives photogenerated charge carriers toward the photoanode/electrolyte interface, where they participate in the oxidation reaction. Additionally, this internal electric field effectively suppresses charge recombination, further enhancing the reaction efficiency. In this approach, adsorption plays a crucial role. The middle hydroxyl groups of glycerol spontaneously adsorb onto the W atom sites of the photoelectrode, while Pt SAs provide additional adsorption sites for the oxygen atoms of both the terminal and middle hydroxyl groups of glycerol. Once adsorbed, glycerol undergoes dehydrogenation, forming carbon-centered radicals as intermediates through reactions with photogenerated holes from the photoanode. The unique structure of the Pt-SA/WO$_x$ surface significantly influences selectivity. The free energy barrier for radical formation at the middle carbon is lower than that at the terminal carbon, favoring the selective conversion of glycerol to DHA. As a result, the Pt-SA/WO$_x$ photoanode achieves an impressive glycerol-to-DHA selectivity of up to 60.2% (Fig. 9g). Additionally, Co SAs can be integrated with C₃N₄/α-Fe₂O₃ to enhance PEC-driven syngas production from CO₂ reduction.[215] Although the actual syngas production occurs at a bimetallic Ag/ Pd cathode, where CO₂ chemisorption and CO desorption take place, Co SAs play a crucial role by providing active sites for C₃N₄ anchoring. These sites facilitate water oxidation and proton/electron transfer, supporting overall reaction efficiency.

While the application of SAs has been extensively explored and widely used in electrochemical systems,[216–219] these
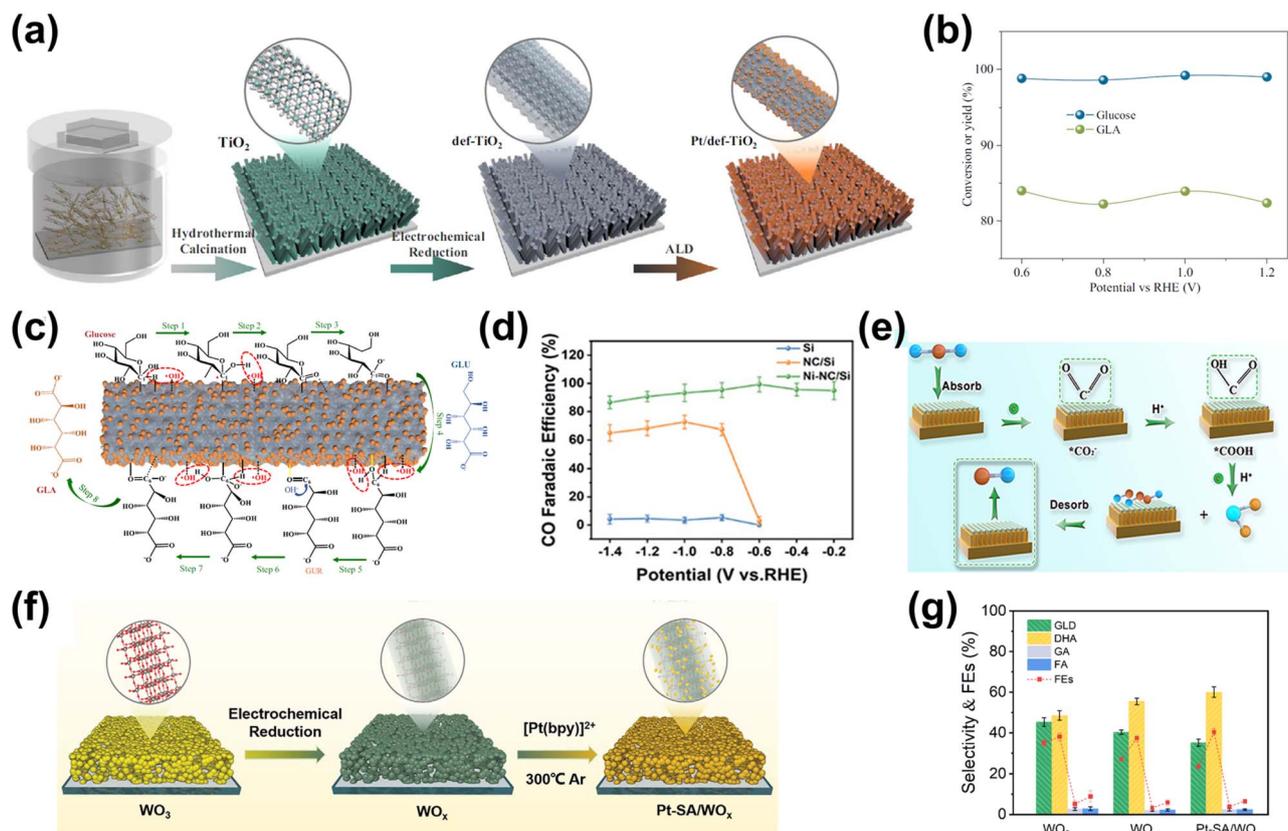
Fig. 9 SA utilization for PEC biomass valorization selectivity enhancement and tuning. (a) Fabrication steps for Pt SAs/def-TiO$_2$ NRAs. (b) Glucose conversion and selectivity of glucaric acid (GLA) as a function of applied potential. (c) Glucose oxidation mechanisms on Pt SA-modified def-TiO$_2$ under light illumination and applied bias. Adapted from ref. 212. Copyright 2023 The Author(s). (d) FE of CO production on the Si-NC/Si NW photocathode. (e) Schematic of the PEC CO$_2$ reduction mechanism on the Si-NC/Si NW photocathode. Adapted from ref. 213 with permission. Copyright 2024 The Royal Society of Chemistry. (f) Synthesis process of Pt−SAs/WO$_x$. (g) Selectivity and FE of PEC glycerol oxidation on Pt−SAs/WO$_x$ compared to WO$_3$ and WO$_x$ photoelectrodes. Adapted from ref. 214 with permission. Copyright 2024 Wiley-VCH GmbH.

examples highlight their versatility in PEC biomass valorization. Unlike nanoparticles or quantum dots, SAs serve as isolated, highly efficient catalytic centers due to their unique electronic and geometric characteristics. From a photoactivity perspective, SAs profoundly influence the electronic structure of the underlying catalyst. This modification enhances light absorption and optimizes energy band alignment, improving photogenerated charge carrier separation while minimizing recombination losses. SAs can also act as electron sinks or hole traps, facilitating charge carrier transfer to reactants and accelerating reaction kinetics. Beyond improving charge transfer, SAs' unsaturated coordination environments lead to stronger interactions with reactants and intermediates. These unique active sites enable precise tuning of reaction pathways, significantly improving PEC reaction selectivity. Furthermore, SAs prevent active site aggregation, ensuring uniform activity and precise control over the catalytic process. Their high surface area also provides abundant reaction sites. However, functionalization with SAs often comes with a high cost due to their sophisticated method.[220] A summary of SA-based PEC biomass valorization strategies is presented in Table 4.

3.1.4. Layered double hydroxides. Layered double hydroxides (LDHs) have gained significant attention in PEC

applications due to their well-defined two-dimensional layered structure, tunable internal architecture, cost-effective and non-toxic metal precursors, and adjustable composition.[221,222] Structurally, LDHs resemble hydrotalcite, comprising positively charged brucite-like layers neutralized by intercalated anionic species and water molecules. The metal cations within LDH layers adopt an octahedral coordination, forming metal hydroxide sheets. The structural integrity of LDHs is primarily maintained by two interactions: first, coulombic attraction between the positively charged metal hydroxide layers and the interlayer anions, which depends on charge distribution, and second, hydrogen bonding between the oxygen atoms of intercalated anions and the hydroxyl groups in the metal hydroxide layers, influenced by coordination symmetry.[40,223,224] A key advantage of LDHs is the uniform distribution of divalent (M^{2+}), trivalent (M^{3+}), or tetravalent (M^{4+}) cations across the hydroxide layers, preventing the formation of localized aggregation sites.

One effective approach to improving the selectivity of PEC biomass valorization is to leverage the tunable interaction of LDHs with reactants. For instance, NiCo LDHs can be employed to improve the selectivity of PEC glycerol[225] and benzyl alcohol[226] oxidation reactions. For the former, controlling selectivity to a higher-valued chemical remains a challenge due to frequent

Table 4 Summary of single atom metal (SA) utilization on the surface of photoelectrodes for PEC biomass valorization selectivity enhancement and tuning applications

Photoelectrode[a]	SA role	Deposition method	Reaction	Target product(s)	Selectivity	FE	Reaction conditions	Ref.
Pt SAs/TiO$_2$ NRAs	Charge transport promoter	Atomic layer deposition	Glucose oxidation	Glucaric acid	84.3%	N/A	• Electrolyte: KOH (1 M) with glucose • Applied bias: 0.6 V_{RHE} • Light: AM 1.5G (100 mW cm^{-2})	212
Ni-NC/Si NWs	Charge transport, promoting COOH* formation and CO desorption	Drop-casting	CO$_2$ reduction	CO	N/A	100%	• Electrolyte: CO$_2$-saturated KHCO$_3$ (0.1 M) • Applied bias: −0.6 V_{RHE} • Light: AM 1.5G (100 mW cm^{-2})	213
Pt SAs/WO$_x$	Charge separation and transport promoter, adsorption site for O atoms of the terminal and middle hydroxyl	Immersion	Glycerol oxidation	DHA	60.2%	N/A	• Electrolyte: Na$_2$SO$_4$ (0.5 M) with glycerol (0.1 M) with pH 2, adjusted by H$_2$SO$_4$ • Applied bias: 1.2 V_{RHE} • Light: AM 1.5G (100 mW cm^{-2})	214

[a] NRA: nanorod array, NW: nanowire, and SA: single atom.

C–C bond cleavage and hydroxyl group peroxidation during electrooxidation. Therefore, to address this, activated NiCo-LDH can be integrated with BiVO$_4$ (Fig. 10a) to produce DHA. The surface oxygen activation process significantly increases the lattice oxygen content, primarily due to the dehydrogenation of hydroxyl groups, which then exposes active oxygen sites on the LDH surface. As a result, it enhances both hole transfer efficiency and surface oxidation activity (Fig. 10b), contributing to improved selectivity to nearly 42% and a productivity of 20.5 μmol cm^{-2} h^{-1} at 1.4 V_{RHE} under light illumination (Fig. 10c(i)), which is higher than those of bare BiVO$_4$ and inactivated LDH-modified photoelectrodes. Notably, when the applied bias was increased, DHA selectivity decreased, likely due to excessive glycerol oxidation, which led to C–C bond breakage (Fig. 10c(ii)). It thus demonstrates tunable selectivity for PEC glycerol oxidation. Moreover, for the selective PEC oxidation of benzyl alcohol, an α-Fe$_2$O$_3$ photoanode can be loaded with a NiCo-LDH cocatalyst *via* a hydrothermal method. In this approach, the performance depends on the relative Ni and Co content in NiCo-LDH (Fig. 10d). As the Co content increases, the electron density of Ni decreases, making it more susceptible to oxidation. At the same time, the energy barrier for forming high-valence species is lowered, thereby enhancing the driving force for NiCo-LDH oxidation by photogenerated holes on α-Fe$_2$O$_3$. This effect is crucial because if the oxidative capability of high-valence NiCo-LDH species is too weak, it becomes challenging to extract protons and electrons from alcohol molecules. As shown in Fig. 10e, the photoanode achieved a benzyl alcohol conversion efficiency of 99.1% and a benzoic acid selectivity of 90.9%. This mechanism confirms that the NiCo-LDH cocatalyst facilitates PEC benzyl alcohol oxidation through an indirect catalytic process involving high-valence species.

Aside from modifying LDH interaction with reactants, LDHs can lead to an increased active surface area, which will improve the PEC performance of the system. For instance, trimetallic transition metal CoNiFe-LDH can be electrodeposited onto Ta$_3$N$_5$ nanotube arrays (Fig. 11a).[227] Through this approach, the trimetallic CoNiFe-LDH nanosheets (NSs) exhibit an enhanced specific surface area, a higher density of exposed active sites, and reduced charge-transfer resistance, attributed to their ultrathin 2D nanostructure and optimized electronic properties (Fig. 11b). This strategy successfully enhances the selectivity of the PEC GOR, achieving nearly 100% FE for the co-production of formate and H$_2$ (Fig. 11c). The improved selectivity stems from the efficient transfer of photogenerated holes in Ta$_3$N$_5$ to the photoelectrode/electrolyte interface, which is assisted by CoNiFe-LDH. Furthermore, the surface-adsorbed glycerol molecules are then activated by these holes and converted into formic acid through further oxidation, which involves C–C bond cleavage. The unique structure of CoNiFe-LDHs and their ability to increase active sites result in improved adsorption and interaction between glycerol and the photoanode. Combining the strategies mentioned above, an ultrathin Co-based layered double hydroxide catalyst and graphene can be incorporated into BiVO$_4$ photoanodes using a hydrothermal method followed by acetone treatment to selectively oxidize benzyl alcohol to benzaldehyde (Fig. 11d).[228] The additional acetone treatment
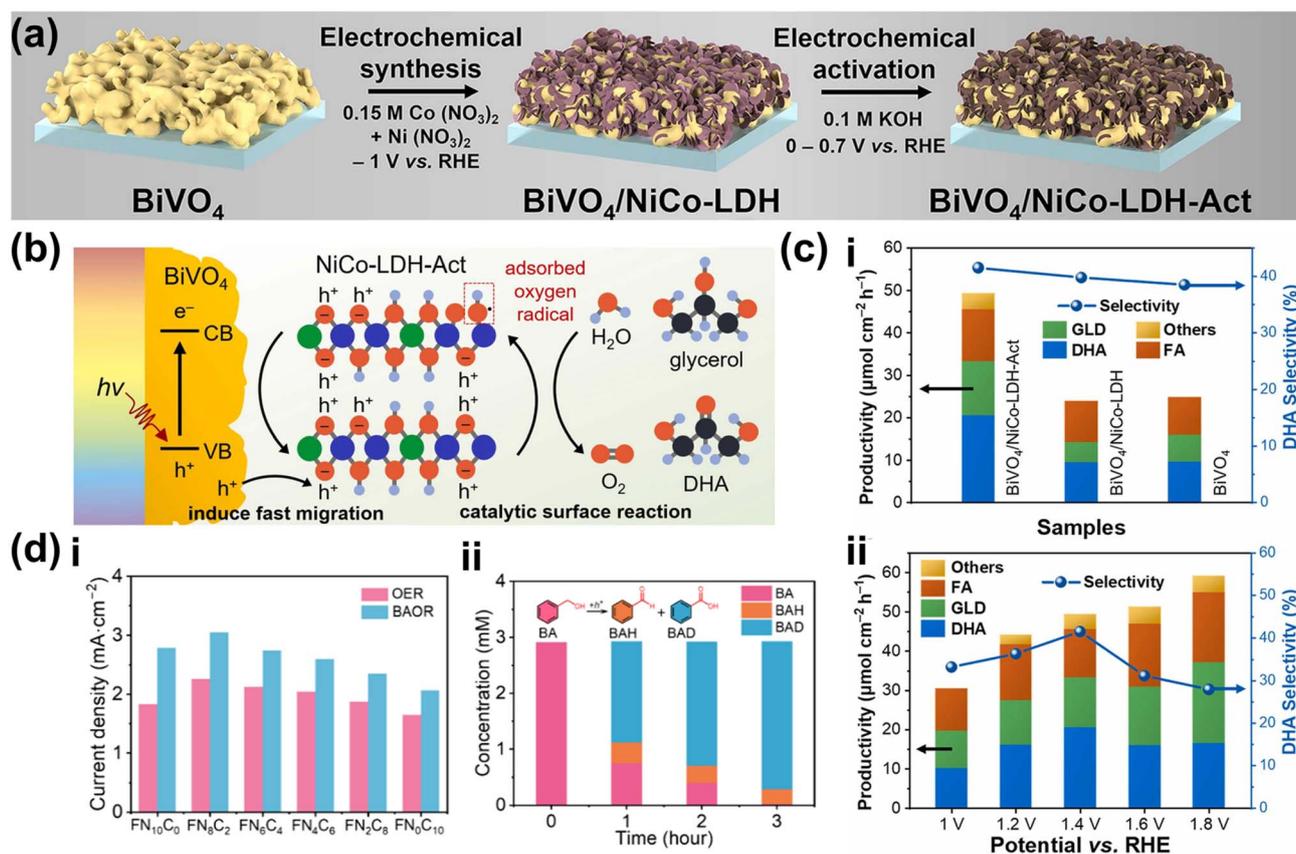
Fig. 10 LDH–reactant interaction modulation for PEC biomass valorization selectivity control. (a) Fabrication steps for the BiVO$_4$/NiCo-LDH-Act photoanode. The LDH is electrodeposited with a three-electrode configuration at −1.0 V$_{Ag/AgCl}$ potential with 7.5×10^{-3} C loading. LDH activation is conducted through cyclic voltammetry from 0 to 0.7 V for 3 cycles. (b) Mechanism of glycerol adsorption and oxidation to DHA on BiVO$_4$/NiCo-LDH-Act. Upon illumination, photogenerated holes facilitate the formation of OH radicals on the surface. These adsorbed OH radicals extract H atoms of glycerol, thereby promoting selective glycerol conversion to DHA. (c) Productivity of various glycerol oxidation products and DHA selectivity over BiVO$_4$/NiCo-LDH-Act (i) compared to inactivated BiVO$_4$/NiCo-LDH and bare BiVO$_4$ photoanodes and (ii) at different potentials within 1 h. Adapted from ref. 225 with permission. Copyright 2022 Elsevier B.V. (d) Performance of the α-Fe$_2$O$_3$/NiCo-LDH photoanode represented as (i) current density for different Ni and Co compositions and (ii) product selectivity over 3 h of reaction. Adapted from ref. 226 with permission. Copyright 2024 American Chemical Society.

promotes the specific growth needed to form ultrathin LDH nanosheets. With this approach, a benzaldehyde yield of 289 µmol was achieved in 4 hours, with a selectivity of nearly 100% (Fig. 11e). This impressive performance stems from the capabilities of the LDH to lower their adsorption energy by adsorbing OH radicals through hydrogen bonding. Furthermore, under illumination, the benzyl alcohol adsorbs onto the LDH surface and converts to carbon-centered radicals, which then combine with the relayed OH radicals obtained by the oxidation of water, and the C–O bond was activated to produce benzaldehyde.

Another role LDHs play in improving the selectivity of PEC biomass valorization is enhancing charge transfer. For instance, BiVO$_4$/NiCo-LDH is shown to improve the selectivity for PEC ethylene glycol oxidation, a key process for converting hydrolysis byproducts of polyethylene terephthalate (PET) plastic waste. Specifically, the heterostructure achieves an impressive FE of over 90% for formate in 0.1 M KOH (Fig. 12a),[229] attributed to the synergistic effect of Ni(OH)$_x$ and Co(OH)$_x$. On one hand, Ni(OH)$_x$ provides a high number of

active sites for ethylene glycol oxidation. On the other hand, Co(OH)$_x$ on BiVO$_4$ acted as a protective layer. Furthermore, when combined, the generation and transfer of photoexcited holes from BiVO$_4$ to NiCo-LDH lead to the oxidation of Ni^{2+} and Co^{2+} to higher oxidation states (Ni^{3+} and Co^{3+} or beyond), further catalyzing ethylene glycol oxidation. In addition, Co-LDH, alone, can be utilized to improve the selectivity of glycerol oxidation toward high-value products, particularly DHA.[230] This approach involves developing Bi$_2$O$_3$ on TiO$_2$ nanorod arrays via electrodeposition, followed by the hydrothermal synthesis of linear Co-LDH on Bi$_2$O$_3$/TiO$_2$ (Fig. 12b). Through this method, a dual type-II heterojunction is formed, effectively suppressing electron–hole recombination. The resulting photoanode allows PEC glycerol oxidation to achieve 65% selectivity, surpassing the 52% for bare Bi$_2$O$_3$/TiO$_2$ (Fig. 12c).

Beyond layered double hydroxides, the use of hydroxides such as Ni(OH)$_2$ offers a promising strategy to tune the selectivity of HMF oxidation. In one such system, Ni(OH)$_2$ is deposited on the surface of titanium-doped hematite (Ti:Fe$_2$O$_3$) (Fig. 12d).[231] Fe$_2$O$_3$ was chosen for its inherent stability, cost-
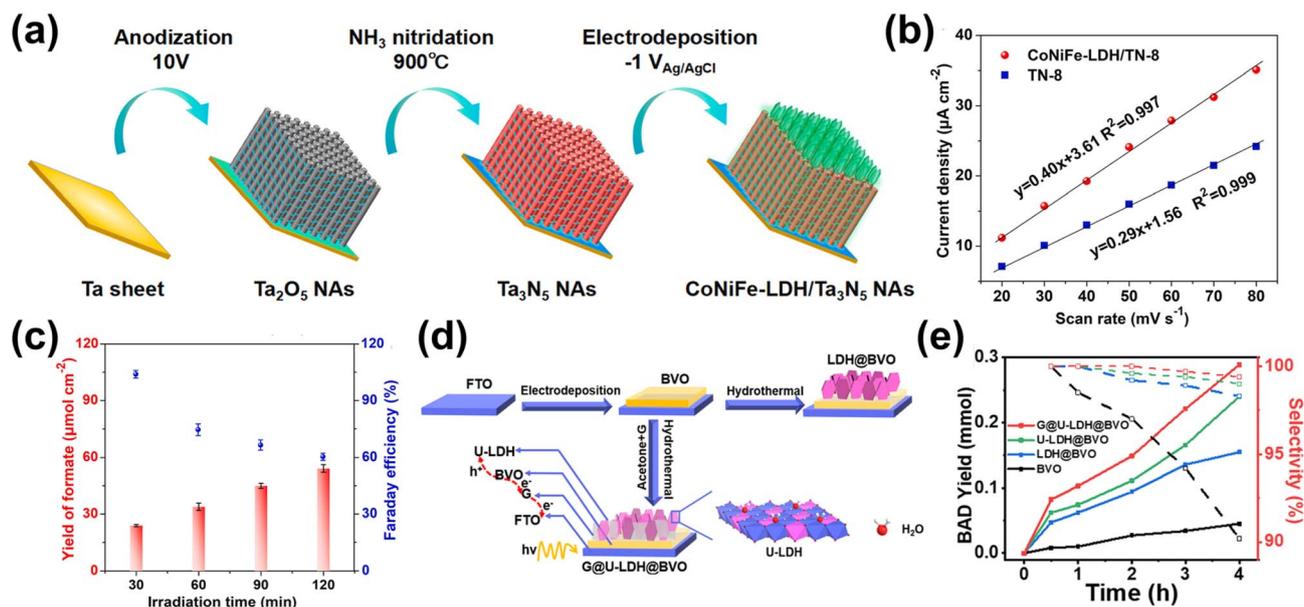
Fig. 11 LDH-improved active surface area to enhance PEC biomass valorization selectivity. (a) Fabrication steps of the CoNiFe-LDH/Ta$_3$N$_5$ photoanode. (b) Plots of current density as a function of scan rate for the bare Ta$_3$N$_5$ (blue) and CoNiFe-LDH/Ta$_3$N$_5$ photoelectrodes. The electrochemically active surface area (ECSA) is estimated by double-layer capacitance, which is represented by a linear slope. The ECSA of LDH-modified Ta$_3$N$_5$ is calculated to be 1.38 times that of bare Ta$_3$N$_5$. (c) Yield of formate and the corresponding FE for formate on CoNiFe-LDH/Ta$_3$N$_5$. Adapted from ref. 227 with permission. Copyright 2021 Elsevier Ltd. (d) Fabrication process of graphene@ultrathin-CoAl-LDH@BiVO$_4$. BiVO$_4$ particles were synthesized on fluorine-doped tin oxide substrates using an electrodeposited-Bi precursor method. Ultrathin LDH nanosheets were vertically grown on the BVO surface via a conventional hydrothermal method, forming the ultrathin-CoAl-LDH@BiVO$_4$ photoanode. To further enhance charge transfer, acetone and graphene dispersion were introduced during the hydrothermal process, resulting in the formation of the graphene@ultrathin-CoAl-LDH@BiVO$_4$ photoanode. (e) Benzaldehyde yield and selectivity as a function of reaction time under illumination at an applied potential of 1.2 V$_{RHE}$. Adapted from ref. 228 with permission. Copyright 2020 American Chemical Society.
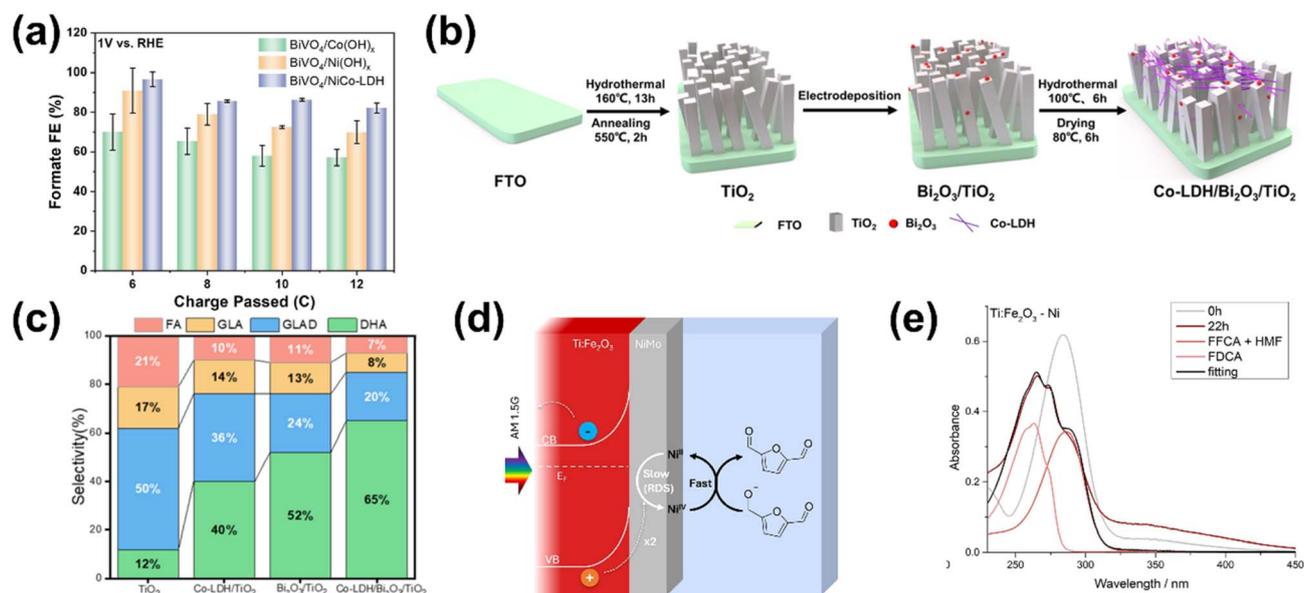
Fig. 12 Utilization of LDHs and hydroxides as charge transfer promoters to improve PEC biomass valorization selectivity. (a) FE of formate from ethylene glycol oxidation on the BiVO$_4$/NiCo-LDH, BiVO$_4$/Ni(OH)$_x$ and BiVO$_4$/Co(OH)$_x$ photoanodes at an applied bias of 1 V$_{RHE}$. Adapted from ref. 229 with permission. Copyright 2024 Wiley-VCH GmbH. (b) Fabrication process of the Co-LDH/Bi$_2$O$_3$/TiO$_2$ photoanode. (c) Selectivity of glycerol oxidation products of Co-LDH/Bi$_2$O$_3$/TiO$_2$ compared to other photoanodes. Adapted from ref. 230 with permission. Copyright 2025 American Chemical Society. (d) Ni(OH)$_2$-deposited Ti:Fe$_2$O$_3$ for selective HMF oxidation to FDCA. (e) UV-vis absorbance spectra evolution from 0 to 22 h of HMF reaction on Ni(OH)$_2$/Ti:Fe$_2$O$_3$.

effectiveness, and excellent light-harvesting capabilities in the visible spectrum.[232] However, its widespread application is often hampered by limited hole diffusion and charge injection efficiency. The introduction of the Ti dopant effectively addresses these limitations by improving charge carrier transport and significantly reducing the recombination of photogenerated charge carriers.[233] Furthermore, the deposition of $Ni(OH)_2$ leads to the swift utilization of excess holes on the oxidized nickel sites by HMF, as evidenced by the nickel oxidation state as a function of applied potential. This strong hole utilization is crucial because it effectively diverts photogenerated holes towards HMF oxidation, thereby suppressing the competitive OER and directly enhancing the selectivity toward HMF oxidation. This directly enhances the selectivity towards HMF oxidation over water oxidation. From a reaction kinetics perspective, the regeneration of Ni^{4+} from its reduced state is the rate-determining step. The decrease in the nickel oxidation state upon HMF addition indicates that Ni^{4+} is rapidly reduced through interaction with HMF. Through the evolution of the absorption spectra (Fig. 12e), it was calculated that the deposition of $Ni(OH)_2$ results in up to 49% selectivity towards FDCA.

To summarize, these examples highlight the versatility of LDHs as cocatalysts in selective PEC biomass valorization reactions. With the ability to modify the binding energy of molecule species and enhance charge transport, LDHs offer a promising solution to improve the selectivity of PEC biomass valorization. Despite their promising advantages, LDHs also present several limitations that can hinder their practical application in PEC biomass valorization. One key drawback is the precise control over the composition and crystallinity of LDHs, particularly when scaling up synthesis for practical applications. These limitations underscore the need for continued optimization of LDH synthesis, stabilization, and integration strategies in PEC systems. The utilization of LDHs in PEC biomass valorization is summarized in Table 5.

3.1.5. Molecular co-catalysts. The integration of molecular co-catalysts, such as coordination compounds, into PEC systems offers a sophisticated strategy for enhancing photoconversion efficiency and selectivity in biomass valorization. These molecular complexes, typically comprising transition metals coordinated with ligands, function as highly specialized catalytic centers that facilitate targeted redox reactions. Their molecular nature allows for precise tuning of redox potential, coordination environment, and electronic structure to align with the specific requirements of PEC reactions.[175–178] While most current applications of such systems have focused on PEC water splitting, their potential for biomass valorization is equally promising. In particular, immobilizing or attaching molecular co-catalysts onto the surface of photoelectrodes enhances photoconversion efficiency by mediating charge transfer between the photoelectrode and the reactants. Acting as intermediaries, these surface-bound co-catalysts accept photogenerated electrons or holes from the photoelectrode and transfer them with high precision to the adsorbed biomass molecules. This process reduces surface charge recombination, thereby ensuring that a greater proportion of photogenerated carriers contribute effectively to the desired reactions.[179–182]

As an example, anchoring 5,10,15,20-tetrakis(4-carboxylphenyl)porphyrin (TCPP) molecules onto Ce–CoCu-LDH has been shown to enhance PEC methanol oxidation.[234] Here, TCPP exhibits high catalytic activity and durability, consequently increasing the light absorption capability of the photoelectrode and generating more photogenerated electrons. Moreover, rapid charge transfer from TCPP to Ce–CoCu-LDH mitigates charge recombination, leading to an enhancement in reactivity by up to 2.3 times even after 500 cycles (Fig. 13a). The method of immobilizing molecular catalysts onto the photoelectrode also plays a crucial role in optimizing charge transfer. For example, modifying the preparation steps allows Si/rGO photoelectrodes to be loaded with a Co-based molecular co-catalyst in different stacking configurations, yielding varying performances.[235] In one strategy, cobalt tetraphenylporphyrin (CoTPP) is immobilized on Si/GO and Si/rGO photoelectrodes through impregnation adsorption in DMF, followed by either separate or simultaneous graphene reduction and calcination (Fig. 13b). This approach enables the photoelectrode to achieve an impressive 82.8% FE for CO from PEC CO_2 reduction at a near-neutral potential of -0.1 V_{RHE}. The simultaneous reduction and calcination process strengthens the electronic interaction between rGO and CoTPP, as evidenced by the shifted Co binding signals (Fig. 13c). Consequently, enhanced electronic interaction improves electron transfer kinetics and catalytic activity, translating to a superior CO selectivity of up to 82.8% in CO_2 reduction at -0.1 V_{RHE} (Fig. 13d). In addition, the catalytic activity of molecular cocatalyst-modified photoelectrodes can be improved by creating synergistic interfaces.[236] The formation of these synergistic interfaces is possible due to the modularity of coordination compounds of the molecular cocatalysts. One notable example is the improved oxidation of *para*-methoxy benzyl alcohol (MeO-BA) to *para*-methoxy benzaldehyde using a catalyst-dye-acceptor molecular array.[237] This array comprises a Ru tris–bipyridine complex as a photosensitizer, linked at one end to 2,2,6,6-tetramethyl-1-piperidine *N*-oxyl (TEMPO) as an alcohol oxidation catalyst, and at another end to the electron acceptor naphthalene-dicarboxyanhydride-dicarboximide (NDADI). Upon illumination, the Ru complex undergoes metal-to-ligand charge transfer, followed by electron injections either directly to the substrate (ITO NPs) or to NDADI. In the former case, the hole shifts from Ru^{III} to TEMPO, driving the oxidation reaction. In the latter case, an additional electron transfer occurs before the hole transfer to TEMPO and subsequent catalysis (Fig. 13e). This synergistic architecture enables the photoelectrode to achieve an outstanding 80% FE for *para*-methoxy benzaldehyde, a significant improvement from the initial 28% FE without TEMPO. This selectivity enhancement results from the combination of the highly oxidative Ru complex and the efficient hole transfer to TEMPO.

In the domain of selectivity tuning, molecular co-catalysts provide well-defined active sites with tunable electronic and geometric properties, enabling selective interactions with specific reactants or intermediates.[41,238,239] This targeted interaction minimizes the formation of undesired by-products and enhances the yield of high-value products. One effective strategy to exploit these capabilities is the integration of

Table 5 Summary of layered double hydroxide (LDH) utilization on the surface of photoelectrodes for PEC biomass valorization selectivity enhancement and tuning applications

Photoelectrode[a]	LDH role	Deposition method	Reaction	Target product(s)	Selectivity	FE	Reaction conditions	Ref.
BiVO$_4$/NiCo-LDH-Act	Promoting surface oxidation and charge transfer promoter	Electrodeposition and CV-assisted activation	Glycerol oxidation	DHA	42%	N/A	• Electrolyte: Na$_2$SO$_4$ (0.5 M) with glycerol (0.6 M) • Applied bias: 1.4 V$_{RHE}$ • Light: AM 1.5G (300 W Xe lamp)	225
α-Fe$_2$O$_3$/NiCo-LDH	Promoting high-valence species formation and surface oxidation	Hydrothermal	Benzyl alcohol oxidation	Benzoic acid	90.9%	N/A	• Electrolyte: KOH (1 M) with benzyl alcohol (50 mM) • Applied bias: 1.23 V$_{RHE}$ • Light: AM 1.5G (300 W Xe lamp)	226
CoNiFe-LDHs/Ta$_3$N$_5$ NAs	Promoting glycerol adsorption and C–C bond breaking, charge transfer promoter	Electrodeposition	Glycerol oxidation	Formate	98%	N/A	• Electrolyte: NaOH (0.1 M) • Applied bias: 1.4 V$_{RHE}$ • Light: AM 1.5G (Xe lamp)	227
Graphene@ ultrathin-CoAl-LDH @BiVO$_4$	Promoting benzyl alcohol and OH radical adsorption, charge transfer promoter	Hydrothermal	Benzyl alcohol oxidation	BAD	99%	N/A	• Electrolyte: PBS (0.1 M, pH 7) with benzyl alcohol (2 mM) • Applied bias: 1.2 V$_{RHE}$ • Light: AM 1.5G (100 mW cm^{-2})	228
BiVO$_4$/NiCo-LDH	Charge transfer promoter	Hydrothermal	Ethylene glycol oxidation	Formate	N/A	85%	• Electrolyte: KOH (0.1 M) • Applied bias: 1.0 V$_{RHE}$ • Light: AM 1.5G	229
Co-LDH/Bi$_2$O$_3$/TiO$_2$	Charge transfer promoter	Hydrothermal	Glycerol oxidation	DHA	65%	N/A	• Electrolyte: Na$_2$SO$_4$ (0.1 M) with glycerol (0.1 M) • Applied bias: 1.23 V$_{RHE}$ • Light: AM 1.5G	230

[a] Act: activated and NA: nanotube array.
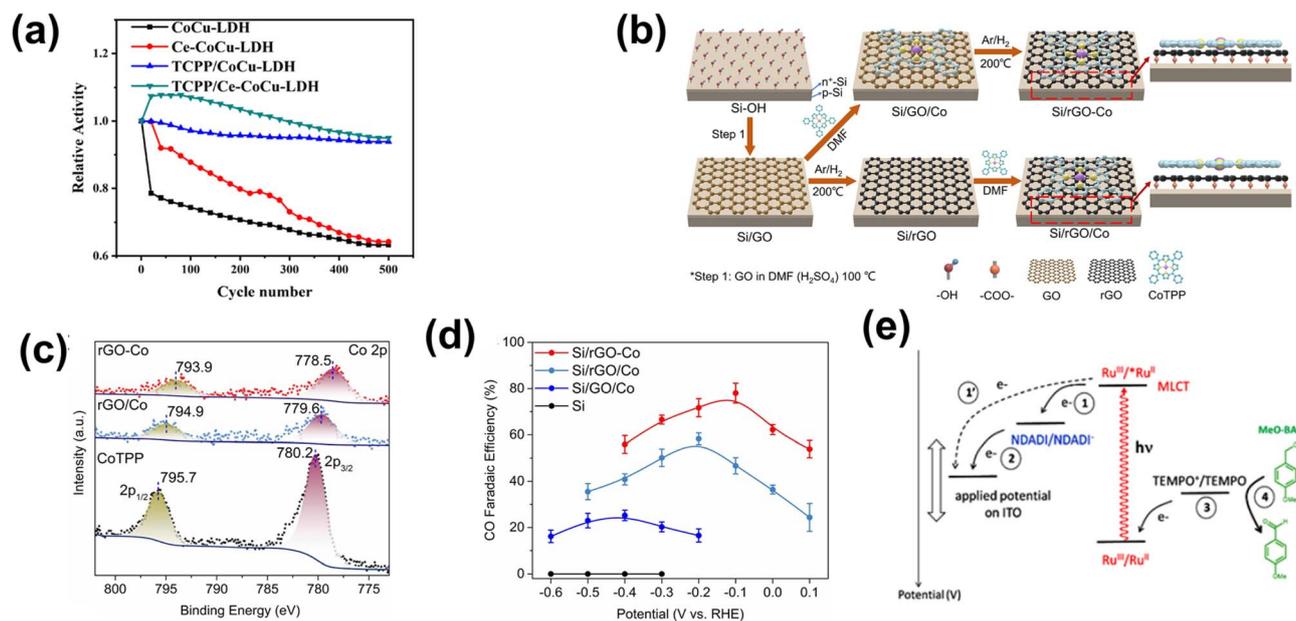
Fig. 13 Molecular co-catalyst utilization to improve catalytic activity for enhanced PEC biomass valorization selectivity. (a) Reactivity stability of bare and modified CoCu-LDHs over 500 cycles for methanol oxidation. Adapted from ref. 234 with permission. Copyright 2022 American Chemical Society. (b) Preparation steps for Si/GO/Co, Si/rGO-Co and Si/rGO/Co photocathodes. (c) XPS spectra of Co 2p for Si/GO/Co, Si/rGO-Co and Si/rGO/Co photocathodes. The peak shift is bigger for Si/rGO-Co compared to Si/rGO/Co, indicating that the electronic interaction of the former is stronger than that of the latter, which aligns with its improvement in selectivity towards CO from PEC CO_2 reduction. (d) FE of CO from CO_2 reduction over various photocathodes as a function of applied bias. Adapted from ref. 235 with permission. Copyright 2023 Wiley-VCH GmbH. (e) Ru-based molecular co-catalyst structure used to modify the α-Fe_2O_3 photoanode surface. Ru_2 and Ru_4 are synthesized as the carboxylic derivatives of Ru_1 and Ru_3, respectively, to enable the anchoring process on the surface of α-Fe_2O_3. The immobilization is conducted by stirring α-Fe_2O_3 with methanol solution containing the molecular co-catalysts.

a photoelectrode with a molecular co-catalyst tailored for specific reactions. For instance, $(bpy)Re(CO)_3Cl$ is commonly employed to enhance CO_2 reduction selectivity toward CO by suppressing formate formation while promoting CO production.[240] This selectivity arises from the unique reaction pathway in which formate is generated through a hydride reaction at an anion coordination site, whereas CO_2 fixation occurs at another site of the Re complex, thereby preventing formate production due to coordinating anions. A practical approach to leveraging this strategy involves coupling porous p-Si with $(bpy)Re(CO)_3Cl$ via hydrosilylation (i.e., the addition of Si–H across unsaturated C=C or C=O bonds), forming a $(bpy)Re(CO)_3Cl@porSi$ (1@porSi) photoelectrode (Fig. 14a).[241] Planar p-Si is electrochemically etched using a hydrofluoric acid solution in ethanol with a 40 mA current to create a porous morphology. This increases the active surface area, enabling greater co-catalyst loading and thereby improving the reactivity and selectivity of CO_2 reduction. Under AM 1.5G illumination at -1.71 $V_{Fc^+/Fc}$ in CO_2-saturated acetonitrile containing phenol, the photoelectrode achieved an average FE of 90% for CO, significantly outperforming pristine porous p-Si and exhibiting a five-fold improvement over Re complex-deposited planar p-Si (Fig. 14b), with high durability (Fig. 14c). Notably, the 1@porSi photoelectrode maintained a FE above 70% even after 5.5 hours of reaction, whereas the catalyst-deposited planar p-Si exhibited activity for only 15 minutes. This high selectivity can be attributed to the substantial molecular catalyst loading, with

41 nmol of Re per 1.2 cm^2 of the 1@porSi photoelectrode—approximately 100 times greater than that of planar p-Si. Moreover, the Re complex demonstrates excellent stability, with minimal leaching observed, as only 10% of the initial catalyst was found in solution after extended operation. Another promising approach involves the integration of mesoporous TiO_2-coupled p-Si ($Si/mesoTiO_2$) with phosphonated cobalt(II) bis(terpyridine) (CotpyP) molecular catalysts via an immersion process to enhance PEC CO_2 reduction.[242] The mesoporous TiO_2 interlayer facilitates high CotpyP loading, improving electron transfer efficiency. Under sunlight irradiation, photogenerated carriers are transferred from Si to the meso-TiO_2 layer and subsequently to the adsorbed molecular catalysts. The catalytic process involves the formation of $[Co^I]^{n-1}$ molecular species through two possible pathways, depending on electrolyte water content: direct proton-coupled electron transfer or an indirect chemical step via $[Co^I]^{n-2}$ intermediates. Following CO_2 adsorption and electron transfer, $[Co^I]^{n-2}$ transforms into $[Co^{II}-CO_2{}^-]^{n-2}$, a key CO-releasing intermediate. Additionally, decoordination of pyridines stabilizes $[Co^{II}-CO_2{}^-]^{n-2}$ via protonation of nitrogen atoms from deprotonated phosphonic acid, which serves as a proton relay to facilitate selective CO_2 reduction to CO rather than formate. This system achieved an FE of up to 48% for CO under AM 1.5G irradiation at -1.0 $V_{Fc^+/Fc}$ in anhydrous acetonitrile containing 40% water.

Molecular co-catalysts also enable multi-electron transfer reactions, a challenge in conventional PEC systems.[244] Their
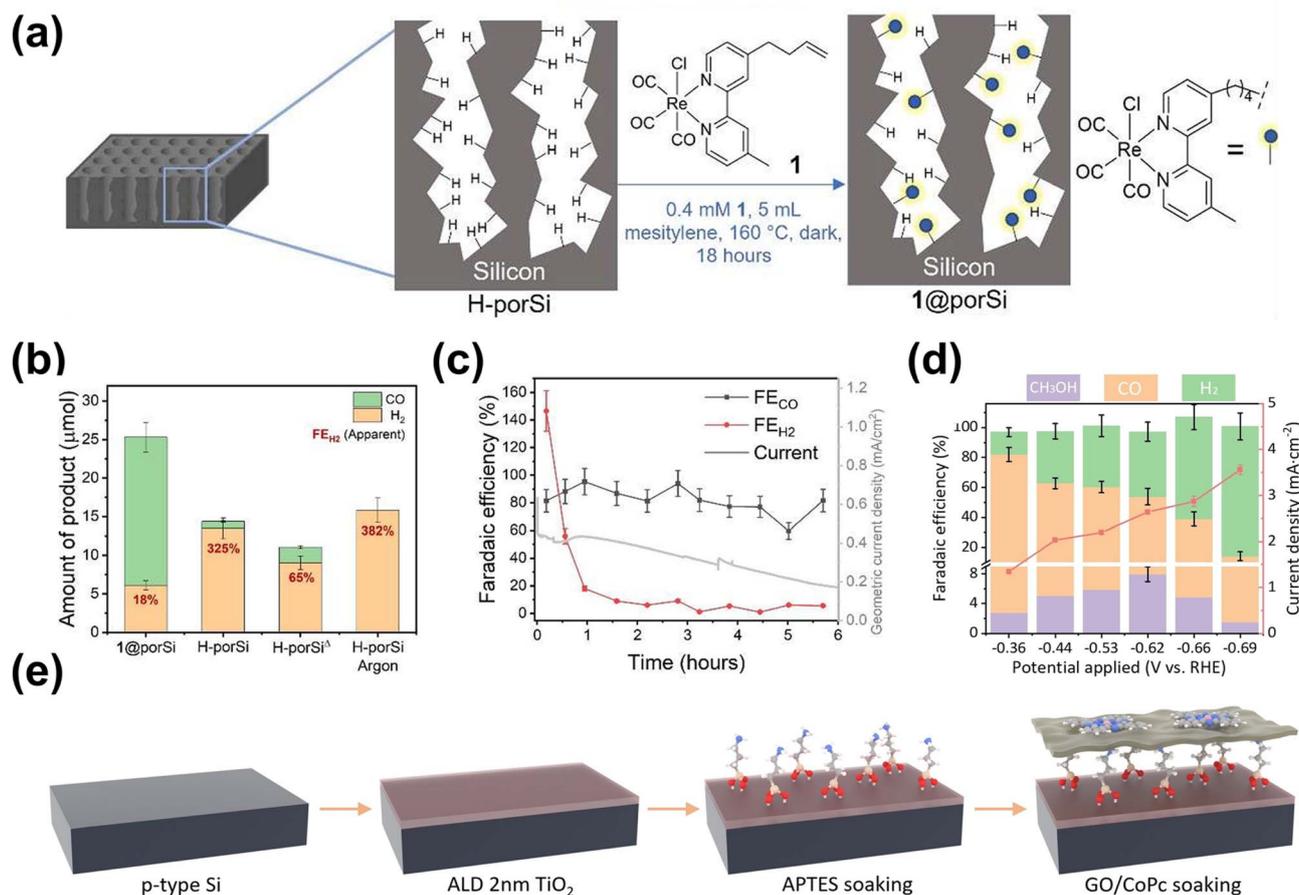
Fig. 14 Molecular co-catalyst-enabled PEC biomass valorization selectivity tuning. (a) Immobilization step of 1 onto porSi to form a 1@porSi photoelectrode. (b) Comparison of product yields and FE on 1@porSi compared to other photoelectrodes. (c) Performance of 1@porSi represented as the evolution of FE over 6 h of PEC CO_2 reduction reaction. Adapted from ref. 241 with permission. Copyright 2024 American Chemical Society. (d) Fabrication process of STA-GO/CoPc. (e) PEC CO_2 reduction of STA-GO/CoPc performance represented as FE over varying applied potentials. Adapted from ref. 243 with permission. Copyright 2022 Wiley-VCH GmbH.

ability to sequentially store and transfer multiple electrons or holes allows them to drive complex transformations, such as the reduction of oxygenated biomass intermediates or selective oxidation processes.[245,246] A notable example is the utilization of cobalt phthalocyanine (CoPc) as a molecular co-catalyst on Si–TiO_2-APTES substrate-supported graphene oxide (STA-GO) for selective PEC CO_2 reduction to CO and methanol (Fig. 14e).[243] This architecture achieves faradaic efficiencies of 86% and 8% for CO and methanol, respectively (Fig. 14f). The CoPc catalyst facilitates the six-electron reduction of CO_2, enabling methanol formation at higher applied bias. However, the relatively low methanol faradaic efficiency is not due to CoPc's catalytic limitations but rather to weak CO trapping on the Si surface, which favors CO production. Thus, modifying the planar Si structure to a more CO-adsorptive configuration could further enhance methanol selectivity.

To summarize, integration of molecular co-catalysts into PEC systems offers a highly effective strategy for enhancing and tuning the selectivity of biomass and CO_2 valorization reactions. These co-catalysts provide several key advantages, such as precise tunability of redox properties and coordination

environments to match specific reaction requirements, enhanced charge transfer kinetics that suppress recombination and improve carrier utilization, well-defined active sites that enable high selectivity toward desired products, and support for complex multi-electron reactions that are otherwise challenging in PEC systems. Despite their considerable advantages, the practical application of molecular co-catalysts in PEC systems is not without limitations. One critical challenge is their long-term operational stability, particularly under harsh photoelectrochemical conditions, where prolonged exposure to light, potential cycling, or aqueous media may lead to photodegradation and ultimately loss of catalytic activity.[247] Additionally, achieving robust and uniform immobilization of molecular co-catalysts on semiconductor surfaces often requires intricate synthetic protocols or surface modifications that may not be easily scalable. Furthermore, many high-performing molecular co-catalysts incorporate rare or expensive transition metals, which could limit their economic viability for large-scale deployment.[248] Therefore, while molecular co-catalysts offer an excellent platform for advancing PEC selectivity and activity, overcoming these challenges remains

Table 6 Summary of molecular co-catalyst utilization on the surface of photoelectrodes for PEC biomass valorization selectivity enhancement and tuning applications

Photoelectrode	Molecular cocatalyst function	Deposition method	Reaction	Target product(s)	Selectivity	FE	Reaction conditions	Ref.
Si/rGO-Co	Charge transfer promoter	Calcination	CO_2 reduction	CO	82.8%	N/A	• Electrolyte: CO_2-saturated $KHCO_3$ (0.1 M) • Applied bias: 0.1 V_{RHE} • Light: AM 1.5G (100 mW cm^{-2})	235
NDADI-P-Ru-TEMPO	Oxidation sites and charge transfer promoter	Chemical activation, ligand reaction, and complexation	_Para_-methoxy benzyl alcohol oxidation	_Para_-methoxy Benzaldehyde	N/A	80%	• Electrolyte: CH_3CN with Bu_4NPF_6 (0.1 M) with 50 mM _para_-methoxy benzyl alcohol • Applied bias: 0.4 V_{SCE} • Light: AM 1.5G	237
(bpy)Re(CO)₃Cl@porSi	CO_2 reduction sites and charge transfer promoter	Hydrothermal	CO_2 reduction	CO	N/A	90%	• Electrolyte: CO_2-saturated MeCN with 100 mM phenol • Applied bias: -1.71 $V_{Fc^+/Fc}$ • Light: AM 1.5G (100 mW cm^{-2})	241
Si/mesoTiO₂/CotpyP	CO_2 reduction and CO desorption intermediate, charge transfer promoter	Immersion	CO_2 reduction	CO	N/A	48%	• Electrolyte: CO_2-saturated $TBABF_4$ (0.1 M) with 40% water:MeCN mixture • Applied bias: 1.0 $V_{Fc^+/Fc}$ • Light: AM 1.5G (100 mW cm^{-2})	242
STA-GO/CoPc	Facilitating six-electron reduction process	Ultrasonication	CO_2 reduction	CO and methanol	N/A	86% (CO) and 23% (methanol)	• Electrolyte: CO_2-saturated $KHCO_3$ (0.1 M) • Applied bias: -0.28 V_{RHE} (CO) and -1.0 V_{RHE} (methanol) • Light: 1.5 sun illumination	243

essential for their transition from laboratory-scale systems to practical biomass and CO_2 valorization technologies. Despite these limitations, molecular co-catalysts remain a promising frontier for advancing selective and efficient PEC valorization technologies. The utilization of molecular cocatalysts for PEC biomass and CO_2 valorization selectivity enhancement and tuning is summarized in Table 6.

3.2. Crystal facet tuning

Crystal facet tuning of catalytic materials in PEC of biomass has been widely explored to enable precise control over catalytic activity, selectivity, and efficiency of the reaction system.[184,249,250] Typically, this is achieved by modulating the exposure of specific crystallographic planes on the catalyst surface. Each crystal facet possesses unique atomic arrangements, coordination states, and surface energies, which govern how reactants and intermediates interact with the catalyst.[46,251] By strategically exposing high-energy facets, which feature more unsaturated and reactive atomic sites, the activation of biomass molecules and subsequent chemical transformations can be significantly enhanced. These facets promote stronger adsorption and stabilization of specific intermediates and are ultimately responsible for lowering activation barriers and accelerating desired reaction pathways.[252] In contrast, lower-energy facets with more stable atomic arrangements may favor selective desorption of products. Consequently, this would reduce

secondary reactions and enhance product selectivity.[253–257] In particular, a facet with an optimized surface energy can selectively adsorb oxygen-containing intermediates from biomass feedstocks, which could stabilize reaction pathways that lead to valuable chemicals or fuels.[258] At the same time, it can suppress the binding of competing or undesired species, minimizing side reactions and waste by-products. For example, a study highlights that exposure of different crystal facets in monoclinic $BiVO_4$ was found to affect its catalytic activity in PEC of glycerol oxidation.[259] $BiVO_4$ with (010)-dominant facets exhibited superior performance to (121)-dominant $BiVO_4$, achieving nearly 60% selectivity to DHA (Fig. 15a). Furthermore, the study also demonstrates that the yield of liquid products obtained from the reaction was also nearly twice as high (Fig. 15b). The superiority of the (010) facet was attributed to its ability to enable more efficient adsorption of glycerol and facilitate charge transfer ability.

In addition to altering adsorption behavior, crystal facet tuning could also significantly influence both electronic and optical properties of the photocatalyst, enhancing the overall PEC performance.[46,134,261] Certain facets possess distinct electronic structures, such as a higher density of surface states or better band edge alignment, which facilitate efficient separation and transfer of photogenerated charge carriers. Electrons and holes may preferentially migrate along specific facets and allow photogenerated carriers to reach reaction sites with minimal recombination losses.[262] Many studies reported that facets with
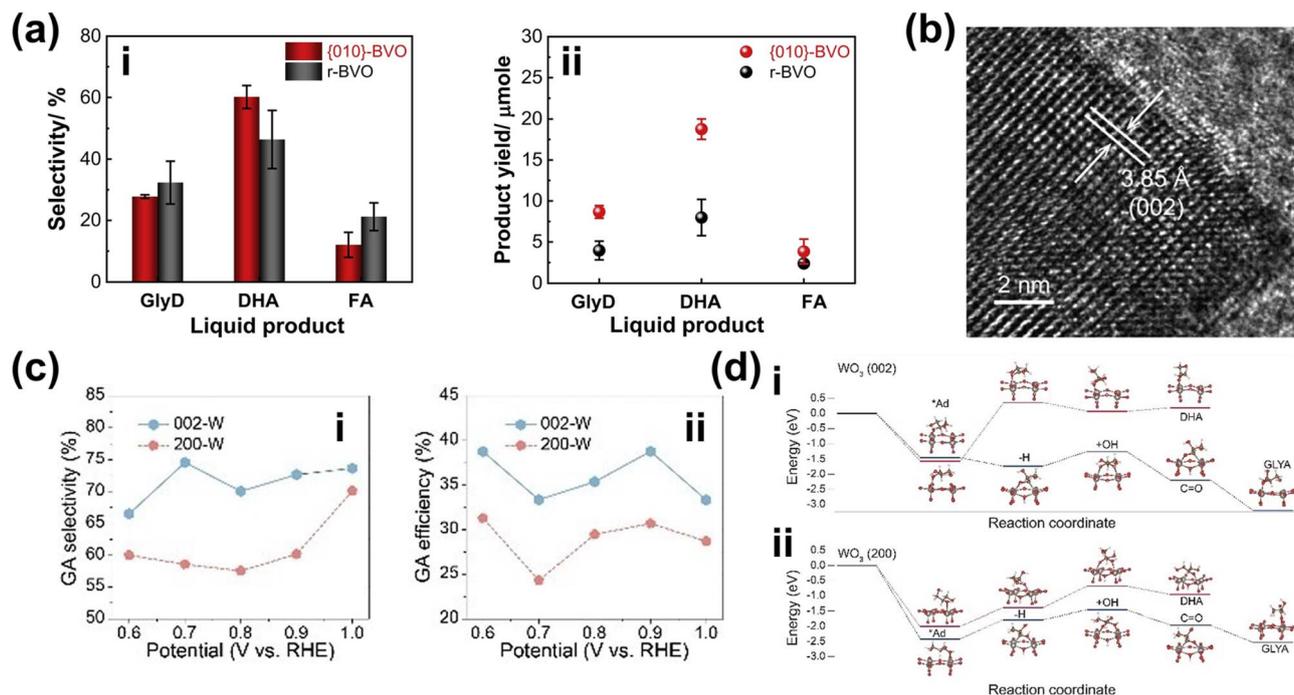

Fig. 15 Crystal facet tuning to modulate adsorption behavior and enhance charge transport for improved PEC biomass valorization selectivity. (a) PEC glycerol oxidation performance on (010)-dominant $BiVO_4$ compared to regular $BiVO_4$ (r-$BiVO_4$) represented by (i) product selectivity and (ii) yield. The (010) and (121) facet-dominated $BiVO_4$ is fabricated through a solvent-assisted hydrothermal method. The distinction of the process is the difference in reaction pH (0.9 and 0.4 for (121) and (010)-$BiVO_4$, respectively). Adapted from ref. 259 with permission. Copyright 2020 Elsevier B.V. (b) HR-TEM image of (002)-exposed WO_3. (c) PEC glycerol oxidation (i) selectivity and (ii) FE of GA on (002)-exposed WO_3 compared to (200)-exposed WO_3. (d) Free energy diagram of PEC glycerol oxidation on top of (i) the (002) facet and (ii) the (200) facet of WO_3. Adapted from ref. 260 with permission. Copyright 2023 Wiley-VCH GmbH.

favorable electronic structures may also reduce bandgaps or introduce localized surface states, which enhance the ability to absorb a broader light spectrum.[263,264] Moreover, facets with high surface energy can amplify localized electric fields. Consequently, it could enhance the activation energy of specific reaction pathways and further improve product selectivity. For instance, monoclinic WO_3 nanosheets with exposed [002] facets were proven to be effective for selective PEC oxidation of glycerol to GA (Fig. 15c).[260] A photocurrent density of 1.7 mA cm^{-2} was achieved with 73% GA selectivity and 39% FE at 0.9 V_{RHE} under AM 1.5G illumination (Fig. 15d). Both experimental and theoretical analyses revealed that the superior performance of (002) facets is attributed to better charge separation, prolonged carrier lifetime from abundant surface trapping states, a lower energy barrier for the glycerol-to-GA reaction, more active sites, and stronger oxidative power of photogenerated holes. This was further confirmed by DFT calculation, which revealed that the glycerol oxidation mechanisms—for the production of both GA and DHA—are modified with the exposure of the (002) crystal facet in WO_3. WO_3 with exposed (002) facets exhibited a much lower energy barrier for glycerol oxidation than that with (200) facets (Fig. 15d(i and ii)). This is primarily due to the ability of the (002) surface to form a spontaneous and strong electrostatic

interaction between W^{6+} and –OH with the terminal and/or middle hydroxyl groups of glycerol molecules. Consequently, this would activate glycerol to further dissociate into H^+ and a glycerol radical, which ultimately transform into GA.

The catalytic performance of facet-tuned anatase nanocrystals with different shapes, i.e. rectangular, rhombic, and nanobar, for hydrogen production via methanol photo-steam reforming has also been studied.[265] Ti^{3+} defect concentration was found to strongly correlate with hydrogen evolution rates. Rectangular nanocrystals with (001), (101), and (010) facets exhibited the highest activity due to the formation of a surface heterojunction that enhances charge separation by directing electrons to (101) and (010) facets and holes to (001) facets. This study highlights the crucial role of facet-dependent electron transfer and photogenerated defects in optimizing anatase nanocrystal photocatalysis. In another study, the effect of the ratio for (001) and (101) facets in anatase TiO_2 on its photocatalytic ability was also theoretically calculated using DFT.[266] Here, results from density of states (DOS) calculation support the introduction of the "surface heterojunction" concept, which explains the enhanced photocatalytic activity arising from the interaction between co-exposed (001) and (101) facets (Fig. 16a–c). A similar phenomenon was also observed on $BiVO_4$, where the photocatalytic
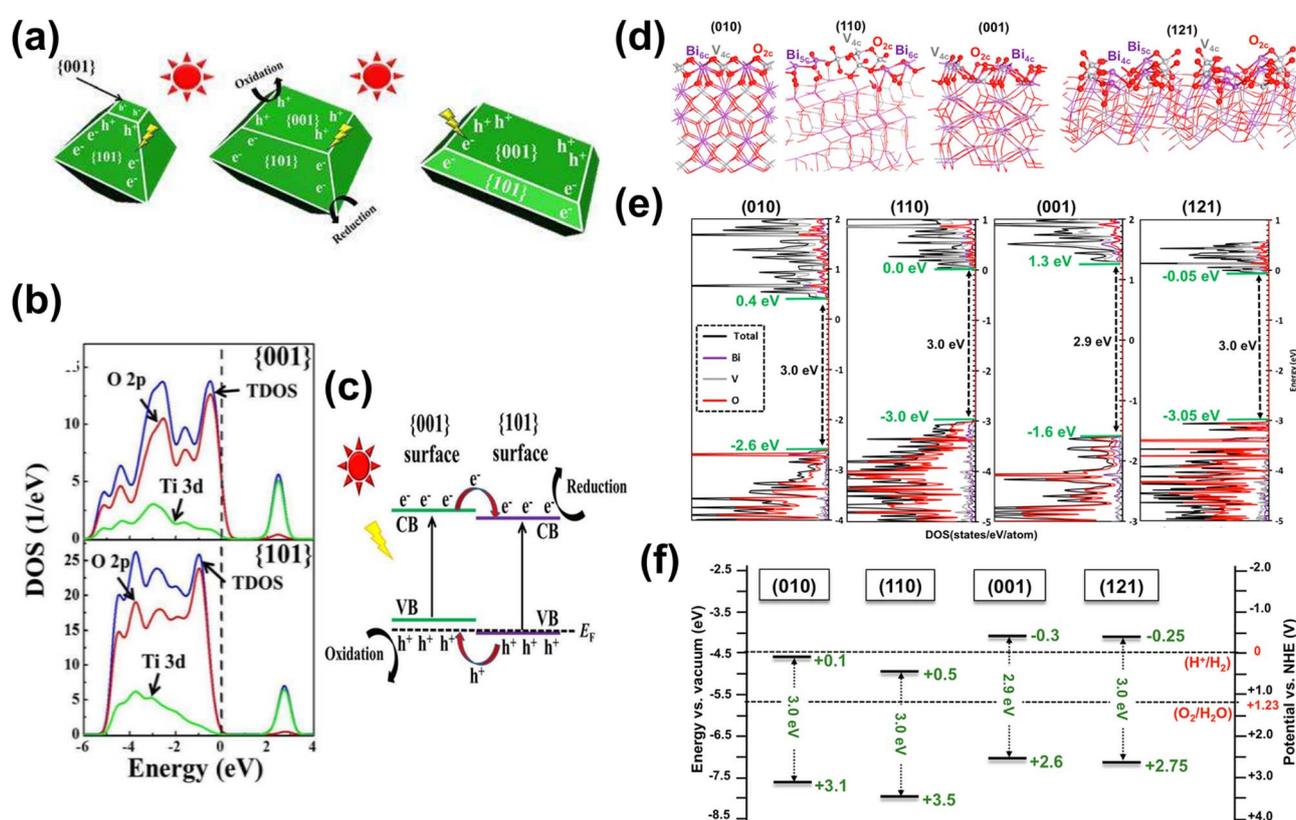
Fig. 16 Enhancing catalytic activity through crystal facet tuning. (a) Schematic illustration of charge separation of electrons and holes in TiO_2's (001) and (101) facets. (b) Density of states (DOS) of TiO_2's (001) and (101) facets. (c) Illustration of the formation of a surface heterojunction. Adapted from ref. 266 with permission. Copyright 2014 American Chemical Society. (d) Relaxed slab structures, (e) DOS diagram, and (f) VBM/CBM positions and bandgap of monoclinic $BiVO_4$ surfaces at various crystal facets. The role of each facet in proton reduction was linked to the surface Bi coordination number and its geometrical distribution. The study reveals that the (001) facet is the most suitable for both the HER and the OER, whereas the (010) facet is effective only for the OER. The (110) and (121) facets were also identified as viable for the OER, though less favorable than (001) and (010). Adapted from ref. 267. Copyright 2020 American Chemical Society.

activity was significantly influenced by the exposure of certain crystal facets.[267] According to the report, it was revealed that both the band positions, valence band maximum (VBM) and conduction band minimum (CBM), and the bandgap of $BiVO_4$ were found to be highly influenced by the exposure of certain crystal faces (Fig. 16d–f). Here, the exposure of (010), (110), (001), and (121) facets of monoclinic $BiVO_4$ was believed to greatly influence redox and transport properties despite similar electronic structures. As a result, the (001) facet was found to be the most suitable for the HER and OER, while the (010) facet is effective primarily for the OER. These studies highlight how facet tuning, through the interplay of surface energy, adsorption energy, and electronic structure, enables precise modulation of redox reactions, improving the tunability of PEC systems.[268] This approach therefore offers new insights into optimizing photoelectrodes for selective PEC biomass valorization.

Furthermore, crystal facet tuning is also capable of enhancing spatial charge separation in the photoelectrode. For instance for $SrTiO_3$ (STO), a total of 26 crystal facets with unique co-exposure of (100)/(110)/(111) were synthesized using the molten salt method (Fig. 17a).[269] Based on the results from *in situ* photodeposition experiments, it was revealed that the active reaction sites for reduction and oxidation were distributed based on the anisotropic distribution of the (100) facet and

(111)/(110) facets, respectively. This is primarily due to the preferential distribution of photogenerated charge carriers, where electrons were found to migrate to (100) facets and holes to (111)/(110) facets. Consequently, such facet-induced internal electric fields significantly improved carrier separation and enhanced the photocatalytic activity of the as-prepared STO for CO_2 reduction to CO and methane (Fig. 17b). In one case, enhancement of catalytic efficiency is caused by a phenomenon called isotropic charge transport, which typically occurs when the photogenerated charge carrier moves in all directions on a specific facet.[270] For example, a porous CuSe@BiOI heterojunction catalyst with enriched (102) facets was successfully synthesized *via in situ* electrochemical deposition and demonstrated exceptional PEC activity in CO_2 reduction and photodetection performance (Fig. 17c). Here, the as-prepared CuSe@BiOI exhibited a high current density of -57.9 mA cm^{-2} with over 80% selectivity for FA (Fig. 17d). According to the report, such enhancement in efficiency and selectivity was primarily attributed to the isotropic charge transport phenomenon where photogenerated charges were efficiently separated at the heterojunction interface due to the exposure of (102) crystal facets.

In another approach, crystal facet tuning is also considered to be responsible for influencing the formation of structural
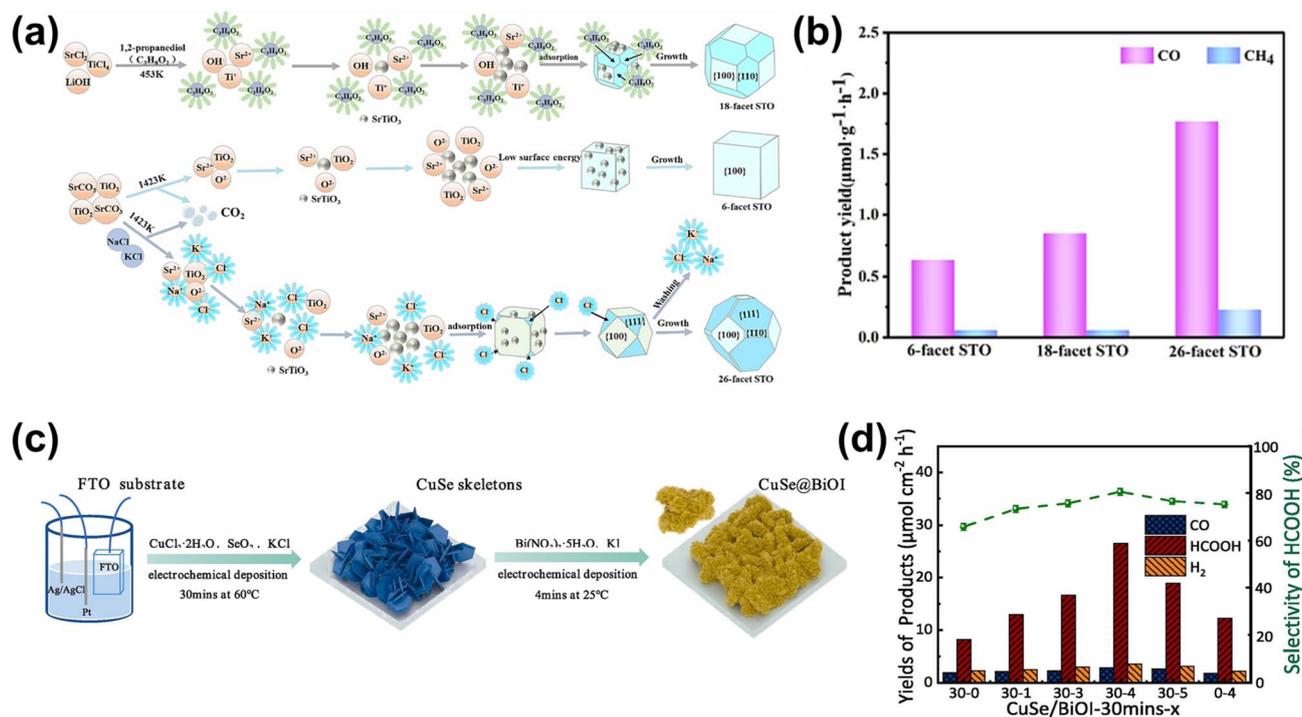
Fig. 17 Crystal facet tuning-induced spatial charge separation and isotropic charge transport to improve PEC biomass valorization selectivity. (a) Schematic of the molten salt method for the preparation of facet-exposed STO. The formation of facet-exposed STO is driven by the selective adsorption of Cl^- ions on the high-energy (111) facets, reducing their surface energy and stabilizing the final structure. During molten salt treatment, STO nanoparticles grow through Ostwald ripening, with high-energy facets shrinking while low-energy facets dominate. Similarly, in the one-step molten salt method, Sr^{2+} and O^{2-} ions migrate to TiO_2 surfaces, forming STO nuclei, with Cl^- adsorption guiding the exposure of (111) facets. (b) Product yield of photocatalytic CO_2 reduction on 6-, 18-, and 26-facet exposed STO. Adapted from ref. 269 with permission. Copyright 2023 Elsevier B.V. (c) Preparation steps for the (102) facet-exposed CuSe@BiOI heterojunction. (d) PEC CO_2 reduction product yield and selectivity of FA on CuSe@BiOI with varying deposition times. Complementing the (102)-dominant CuSe@BiOI, the porous structure of the photoelectrodes allows more CO_2 adsorption and activation. Adapted from ref. 270 with permission. Copyright 2024 Elsevier B.V.

features such as crystal defects and O_{Vac}.[271,272] High-energy facets are often associated with unsaturated atomic coordination, which tends to generate defects such as step edges, dislocations and kinks, creating highly reactive sites. These defects act as catalytic hotspots by stabilizing key intermediates and promoting selective reaction pathways. Simultaneously, O_{Vac} are more prevalent on high-energy facets due to their inherent instability and tendency to lose lattice oxygen. These vacancies introduce localized electronic states within the bandgap, improving light absorption and facilitating charge carrier separation. In addition, O_{Vac} could also provide electron-rich centers that could improve adsorption and activation of oxygen-containing functional groups in biomass molecules. For example, a study demonstrates the role of facet tuning and O_{Vac} in optimizing electron transfer and ozone activation by synthesizing CeO_2 with predominantly exposure of (110), (100), or (111) facets.[273] In this study, it was found that CeO_2 with dominant exposure of the (110) facet exhibited the highest efficiency for phenol mineralization due to its superior charge carrier separation and enhanced electron transfer for O_3 activation. Interestingly, *ex situ*, quasi-situ, and *in situ* characterization revealed that facet modulation influences the electronic properties of CeO_2 due to the increased number of O_{Vac} density, which is responsible for accelerating O_3 activation and facilitating the formation of reactive oxygen species.

To summarize, crystal facet tuning plays a pivotal role in tailoring the catalytic performance of materials in PEC biomass and CO_2 conversion by modulating the exposure of specific crystallographic planes. High-energy facets, characterized by unsaturated atomic sites, enhance reactant adsorption, lower activation barriers, and promote selective reaction pathways, while low-energy facets facilitate product desorption and improve selectivity. Moreover, crystal facet tuning significantly influences the electronic and optical properties of photocatalysts by optimizing charge carrier separation, modifying band structures, and amplifying localized electric fields, leading to enhanced PEC performance. Various studies have demonstrated how facet-dependent electronic structures, spatial charge separation, and defect formation contribute to improved reaction efficiencies. Additionally, the interplay between facet exposure and structural defects, such as O_{Vac}, introduces reactive sites that further boost catalytic activity and selectivity. However, despite these advantages, several challenges limit the widespread application of facet tuning. Precisely controlling the synthesis of facet-exposed structures often requires complex, time-consuming, and condition-sensitive fabrication methods.[274,275] These processes may have low scalability and reproducibility, hindering large-scale implementation. Furthermore, the interplay between multiple facets and their synergistic or antagonistic effects on complex biomass-derived intermediates remains difficult to predict and model, requiring advanced characterization and theoretical tools.[276] All in all, while crystal facet tuning offers highly selective PEC systems, addressing its synthetic complexity and mechanistic uncertainties will be crucial for its practical deployment in biomass and CO_2 valorization technologies. The utilization of

Table 7 Summary of crystal facet tuning of photoelectrodes for PEC biomass valorization selectivity enhancement and tuning applications

Photoelectrode	Facet tuning function	Tuning method	Reaction	Target product(s)	Selectivity	FE	Reaction conditions	Ref.
(010)-Dominant $BiVO_4$	Promotes glycerol adsorption, charge transport promoter, facilitating high carrier density	Solvent-assisted hydrothermal method	Glycerol oxidation	DHA	60%	N/A	• Electrolyte: $Na_2B_4O_7$ (0.1 M) with glycerol (0.1 M) • Applied bias: 1.1 V_{RHE} • Light: AM 1.5G (100 mW cm^{-2})	259
(002)-WO_3	Lowering the energy barrier for oxidation, charge transport promoter	Solvothermal method	Glycerol oxidation	GA	73%	N/A	• Electrolyte: H_2SO_4 (0.5 M) with glycerol • Applied bias: 0.9 V_{RHE} • Light: AM 1.5G (100 mW cm^{-2})	260
(102)-CuSe@BiOI	Charge separation promoter	Electrodeposition method	CO_2 reduction	FA	80%	N/A	• Electrolyte: CO_2-saturated $KHCO_3$ (0.5 M) • Applied bias: 1.2 V_{RHE} • Light: AM 1.5G (150 mW cm^{-2})	270

crystal facet tuning for selective PEC biomass and CO_2 valorization is summarized in Table 7.

3.3. Defect engineering

Surficial vacancy and defect engineering have been rigorously studied to improve charge separation and surface reactivity for PEC reactions.[277–281] Surface O_{Vac}, for example, have been found to suppress surface charge recombination and improve charge transport of photoelectrodes.[282,283] However, extra care is needed since bulk O_{Vac} have been shown to negatively impact the PEC performance due to the interruption of bulk charge transport.[47] Other than O_{Vac}, metal vacancies could be utilized to improve charge carrier mobility on the photoelectrode.[48]

Introduction of vacancies and defects has also been used as a strategy to enhance PEC biomass valorization selectivity and reactivity through charge transport improvement. For instance, O_{Vac} on the $CoO_x/BiVO_4$ heterojunction of the Au/$CoO_x/BiVO_4$ photoelectrode can be utilized to enhance PEC glycerol valorization to high-valued DHA (Fig. 18a).[284] This method enhances the glycerol-to-DHA selectivity from the

initial 37.9% of pristine $BiVO_4$ to 53.2% (Fig. 18b). The increased selectivity stems from the O_{Vac}, which decreases the depletion layer width of the photoelectrode, from the initial 11.95 nm to 6.28 nm for $CoO_x/BiVO_4$ (Fig. 18c), indicating sharper band bending at the photoelectrode/electrolyte interface, which accelerates hole drift from the depletion region to the surface and suppresses charge recombination. Similarly, O_{Vac} are utilized in the ultrathin B-activated $NiCoO_x/BiVO_4$ photoelectrode (Fig. 18d).[285] This treatment deposits a 2 nm thick $B:NiCoO_x$ layer on $BiVO_4$, providing abundant O_{Vac}. The ultrathin-high O_{Vac} $B:NiCoO_x$ layer creates active sites for H_2O to form hydroxyl groups, which are then used to oxidize glycerol to FA. Furthermore, the O_{Vac} facilitates hole extraction or storage and accelerates highly oxidizing hole transport. With this approach, the system achieves a selectivity of 48.7% for 1.5 hours (Fig. 18e).

Additionally, the strategy of improving charge transport through defect engineering has also been pursued to obtain high-value products of PEC CO_2 reduction with high efficiency. Considering the high value and energy density of multi-carbon products, the efficient production of ethanol and acetic acid is
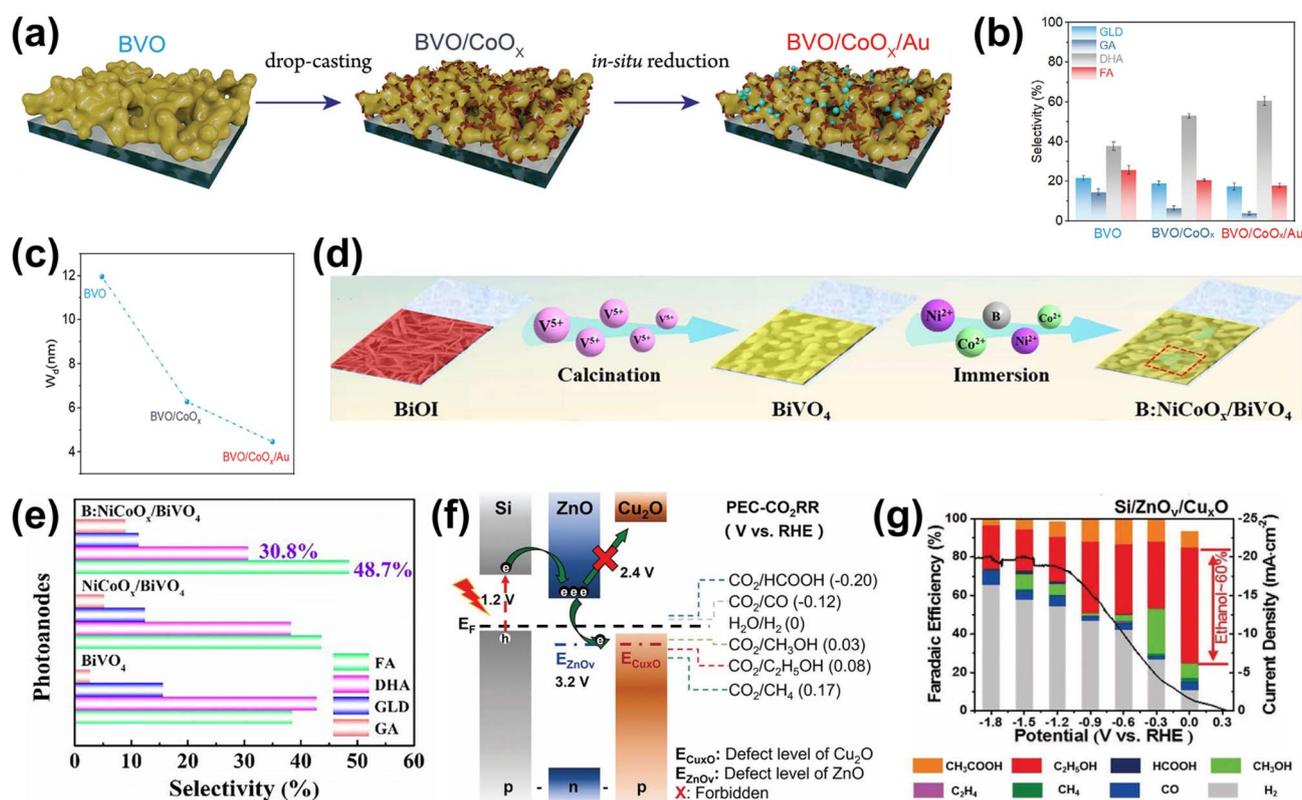
Fig. 18 Improving charge transport through surficial defects for PEC biomass valorization selectivity enhancement. (a) Fabrication steps for the Au/$CoO_x/BiVO_4$ photoelectrode. A solution of $Co(NO_3)_2 \cdot 6H_2O$ is mixed with ammonia solution and H_2O_2 and then stirred to oxidize Co^{2+} to Co^{3+}. The mixture is subsequently drop-cast onto $BiVO_4$ to form $CoO_x/BiVO_4$. (b) Increased selectivity towards DHA from PEC glycerol oxidation on Au/$CoO_x/BiVO_4$. (c) Depletion layer width comparison of Au/$CoO_x/BiVO_4$ compared to other photoelectrodes. Adapted from ref. 284 with permission. Copyright 2024 Wiley-VCH GmbH. (d) Preparation steps for the $B:NiCoO_x/BiVO_4$ photoelectrode. Pristine $BiVO_4$ is immersed in a solution containing 50 mL $NiCl_2 \cdot 6H_2O$ (10 mM), 50 mL $CoCl_2 \cdot 6H_2O$ (10 mM), and $NaBH_4$ for one hour. (e) Product selectivity of glycerol oxidation on the $B:NiCoO_x/BiVO_4$ photoelectrode. Adapted from ref. 285 with permission. Copyright 2024 Elsevier B.V. (f) Band alignment of the p-Si/ZnO_V/Cu_xO photoelectrode and electron flow schematics. (g) FE of the PEC CO_2 reduction reaction on p-Si/ZnO_V/Cu_xO. Adapted from ref. 286 with permission. Copyright 2022 Wiley-VCH GmbH.

very attractive.[287] However, to shift CO_2 reduction selectivity towards multi-carbon products, the system needs to promote multi-electron transfer, which requires very efficient excitation and separation of multiple electrons. Thus, one example utilizes ZnO with O_{Vac} (ZnO_v) and defective Cu_2O (Cu_xO) with p-Si to form a p–n–p band alignment (Fig. 18f).[286] This alignment enables confining and accumulating multiple electrons in the conduction band of n-type ZnO_v under a built-in electric field, while its shallow energy level allows the electron to escape the well and into Cu_xO. These tunneling defect energy levels on Cu_xO are close to matching the energy levels of CO_2-to-ethanol reduction. Therefore, the selectivity towards ethanol is improved (Fig. 18g). Notably, the architecture allows the system to reduce CO_2 to ethanol at 0 V_{RHE}.

Aside from improving charge transfer to enhance the selectivity of PEC biomass valorization reactions, defects could serve as or form active sites for the adsorption of intermediates, which will contribute to the selectivity tuning of PEC biomass valorization.[47] For instance, O_{Vac} on the surface of $BiVO_4$ play a vital role in selectively adsorbing and activating secondary hydroxyl groups of glycerol molecules.[288] $BiVO_4$ was deposited through spin-coating on a SnO_2 nanosheet array and further annealed in an Ar atmosphere to induce a higher concentration of O_{Vac} (Fig. 19a). The presence of O_{Vac} lowers the adsorption energy for secondary hydroxyls (Fig. 19b), thereby shifting the reaction selectivity towards DHA (Fig. 19c). However, the maximum DHA selectivity achieved is only up to 26.5%, with FA as one of the main products aside from DHA. The high FA production occurs due to the glycerol oxidation mechanism on the photoelectrode. The symmetrical molecules possess two primary hydroxyl groups, which when attacked by adsorbed

*OH will oxidize to glyceraldehyde. Glyceraldehyde is prone to further oxidation to glyceric and glycolic acid, which through C–C cleavage can be converted into FA, thereby allowing substantial FA production.

Alternatively, a higher glycerol-to-DHA selectivity has been achieved by transforming a pristine monoclinic $BiVO_4$ surface into a Bi-rich $BiVO_{4-x}$ surface.[289] Bi atoms have been shown to exhibit heightened adsorption capacity for the secondary hydroxyl group of glycerol, which is responsible for selective oxidation to DHA.[291] Therefore, forming a Bi-rich surface layer will promote the glycerol oxidation pathway towards DHA. The method involves alkaline etching in NaOH to leach surface V atoms, followed by electrochemical etching in potassium borate (KBi) electrolyte to induce O_{Vac}, providing more surface Bi atom active sites for glycerol adsorption. As shown in Fig. 19d, this approach improves selectivity towards DHA from 54% to 80.3%. Moreover, the improved selectivity also stems from the shifted band alignments toward the vacuum level (Fig. 19e), which is favorable for efficient electron–hole separation. Another example of leveraging surficial defects to tune PEC biomass valorization selectivity involves modulating O_{Vac} on the surface of a WO_3 photoelectrode (WO_{3-x}) through exposure to 15 mM $NaBH_4$, generating exclusive surface defects.[290] These vacancies increase the availability of W^{5+} active sites for glycerol adsorption. Using this method, the photoelectrode achieves 86.1% selectivity for glyceraldehyde with a production rate of 378.8 mmol m^{-2} h^{-1} (Fig. 19f). However, different from the previously mentioned interaction of the O_{Vac} with the glycerol molecules, the surface of WO_{3-x} has a lower adsorption and activation energy for the terminal hydroxyl group of the glycerol, which results in the favorable oxidation of glycerol to glyceraldehyde.
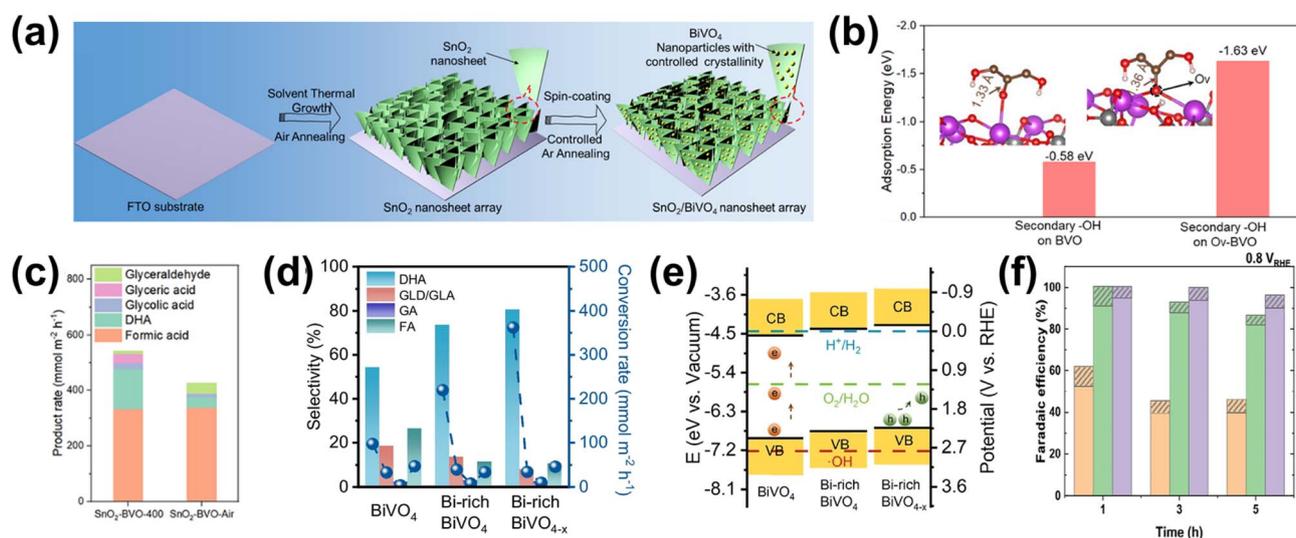
Fig. 19 Surficial defects for selectivity tuning in PEC glycerol oxidation. (a) Synthesis steps for SnO_2/O_{Vac}-enriched $BiVO_4$. (b) Calculated adsorption energy of secondary hydroxyl of glycerol on pristine and O_{Vac}-enriched $BiVO_4$. (c) Production rate of glycerol oxidation on SnO_2/O_{Vac}-enriched $BiVO_4$ compared to $SnO_2/BiVO_4$ ($SnO_2/BiVO_4$-air). Adapted from ref. 288 with permission. Copyright 2025 The Royal Society of Chemistry. (d) PEC glycerol oxidation product selectivity on the Bi-rich $BiVO_{4-x}$ photoelectrode compared to pristine $BiVO_4$ and Bi-rich $BiVO_4$. (e) Band alignments of the Bi-rich $BiVO_{4-x}$ photoelectrode compared to other photoelectrodes. Adapted from ref. 289. Copyright 2024 The Author(s). (f) FE of glycerol oxidation products on WO_3 with O_{Vac} (purple) compared with WO_3 with fewer O_{Vac} (green) and pristine WO_3 (orange). Adapted from ref. 290. Copyright 2024 The Author(s).

In another example, surface S vacancies on CdS/Cu$_2$ZnSnS$_4$ (CZTS) photoelectrodes can be modulated through heat treatment in varying ambient gases, demonstrating versatility in tuning PEC CO$_2$ reduction selectivity (Fig. 20a).[292] Heat treatment in air leads to a photoelectrode selective for methanol and ethanol, achieving yield rates of up to 3 μmol cm^{-2} h^{-1} and 2 μmol cm^{-2} h^{-1}, respectively (Fig. 20b(i)). Conversely, heat treatment in N$_2$ increased its selectivity for CO production up to 2.31 μmol cm^{-2} h^{-1} (Fig. 20b(ii)). This unique tunability arises from the S vacancies of the photoelectrode. The chemical bath deposition of the CdS layer on CZST induced S vacancies on the surface CdS layer. When treated in air, these vacancies are filled with O atoms, decreasing the S vacancies. This results in lower CO$_2$ and CO adsorption energy. In contrast, when treated with N$_2$, the CdS layer preserves the S vacancies. These vacancies facilitated CO desorption, therefore increasing its selectivity towards CO. Furthermore, O$_{Vac}$ on the CdS/CZST photoelectrode can be modulated for NO$_x$ reduction reaction selectivity tuning through the deposition of a temperature-sensitive

TiO$_x$ layer on CdS/CZST (Fig. 20c).[293] In the deposition process, decomposition of acetylacetone is temperature sensitive and leads to the formation of Ti^{3+}, which is closely related to the adsorption of NO$_3^-$ and *NO$_2^-$. The formation of Ti^{3+} on the surface accompanies the generation of O$_{Vac}$ on TiO$_x$. Therefore, the O defects can be modulated and indirectly tune the selectivity of the photoelectrode. When modified with TiO$_x$ deposited at 250 °C, the photoelectrode achieved 89.1% FE towards ammonia (Fig. 20d). One of the underlying factors for the improved selectivity is the increase of catalytically active sites. The increase in surface coverage of Ti^{3+} proved to result in selectivity towards ammonia. Additionally, the AcAc ligand from TIAA is electrophilic, which promotes adsorption of NO$_3^-$ and NO$_2^-$, thereby facilitating ammonia production. In contrast, if the TiO$_x$ layer on the photoelectrode is dominated by Ti^{4+} only, which is ordinary TiO$_2$, it promotes NO$_2^-$ desorption before further oxidation, demonstrated by 60% faradaic efficiency at 0.0 V$_{RHE}$ with no byproduct, resulting in 100% selectivity towards NO$_2^-$. It is worth highlighting that this method of
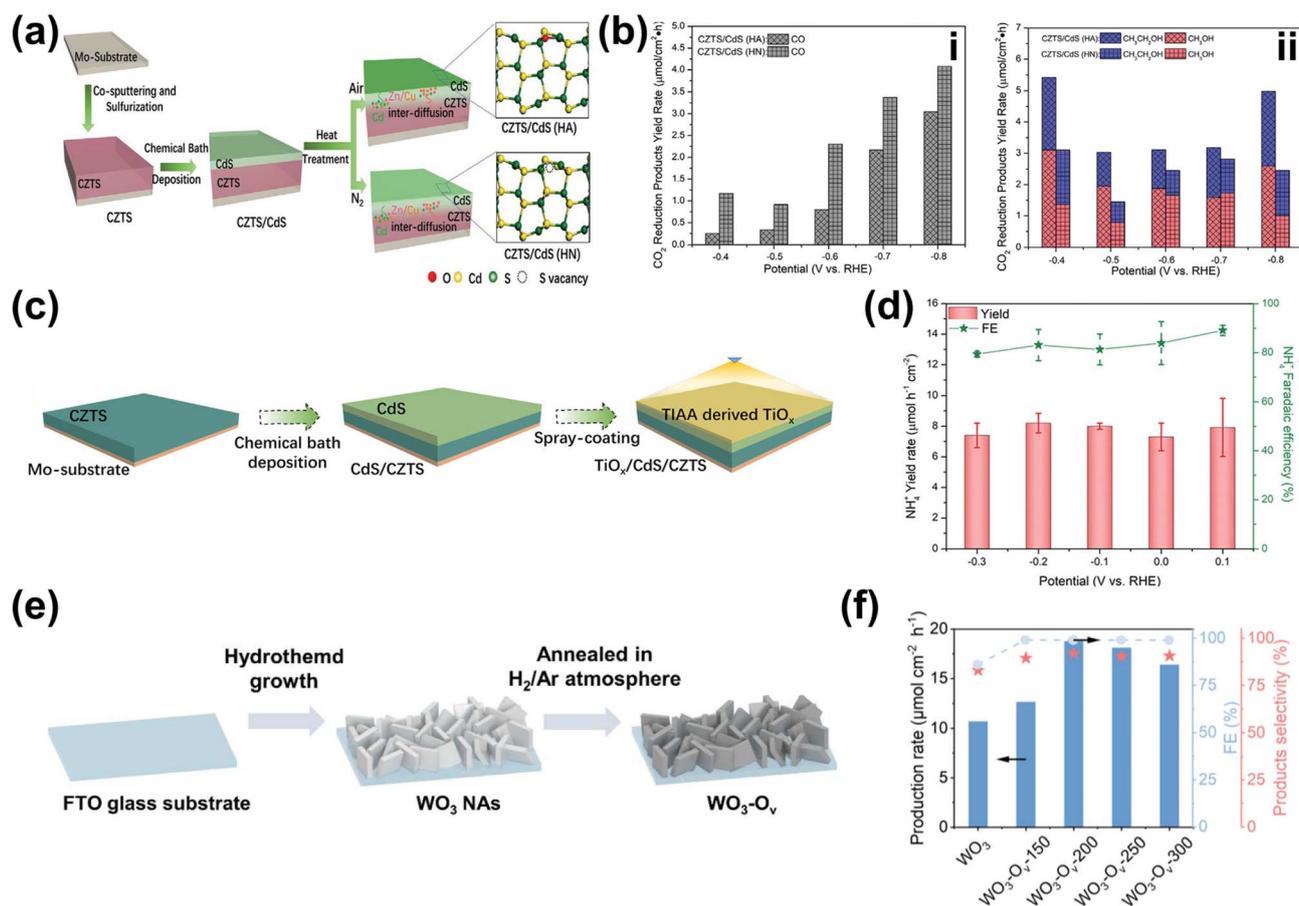
Fig. 20 Surface defects in other PEC biomass valorization applications. (a) Preparation steps of the CZTS/CdS photoelectrode. (b) PEC CO$_2$ reduction performance of CZTS/CdS photoelectrodes represented as yield for (i) CO and (ii) methanol and ethanol. Adapted from ref. 292 with permission. Copyright 2021 Wiley-VCH GmbH. (c) Fabrication steps of TiO$_x$/CdS/CZTS. The TiO$_x$ layer is deposited through spray-coating titanium diisopropoxide bis(acetylacetonate) (TIAA) on CdS/CZST. (d) PEC NO$_x$ reduction performance of TiO$_x$/CdS/CZTS represented as the yield and FE of ammonia as a function of applied bias. Adapted from ref. 293. Copyright 2022 The Author(s). (e) Fabrication process of O$_{Vac}$-enriched WO$_3$ (WO$_3$-O$_V$). (f) PEC procaine conversion to chloroprocaine performance of WO$_3$-O$_V$ photoelectrodes represented as production rate, FE, and selectivity at varying annealing temperatures. Adapted from ref. 294 with permission. Copyright 2024 American Institute of Chemical Engineers.

Table 8 Summary of surface defect utilization of photoelectrodes for PEC biomass valorization selectivity enhancement and tuning applications

| Photoelectrode	Defect function	Induction method	Reaction	Target product(s)	Selectivity	FE	Reaction conditions	Ref.
Au/CoO$_x$/BiVO$_4$	Improving charge transfer by decreasing the depletion layer width	Ammonia and H$_2$O$_2$-assisted Co^{2+} oxidation, drop-casting	Glycerol oxidation	DHA	53.2%	N/A	• Electrolyte: H$_2$SO$_4$ (pH 2) with glycerol (0.5 M) • Applied bias: 1.2 V$_{RHE}$ • Light: AM 1.5G (100 mW cm^{-2})	284
B:NiCoO$_x$/BiVO$_4$	Facilitate hole extraction, storage, transfer, serving as active oxidation sites	Immersion in NaBH$_4$-mixed solution	Glycerol oxidation	FA	48.7%	N/A	• Electrolyte: Na$_2$SO$_4$ (0.5 M) with glycerol (0.1 M) • Applied bias: 1.23 V$_{RHE}$ • Light: AM 1.5G (100 mW cm^{-2})	285
p-Si/n-ZnO$_{Vac}$/p-Cu$_x$O	Facilitating defect-assisted electron tunneling	Annealing in air and ion exchange in CuCl$_2$	CO$_2$ reduction	Ethanol	N/A	60%	• Electrolyte: CO$_2$-dissolved KHCO$_3$ (0.1 M) • Applied bias: −1.8 V$_{RHE}$ to 0 V$_{RHE}$ • Light: AM 1.5G (100 mW cm^{-2})	286
SnO$_2$/BVO-x	Secondary hydroxyl group adsorption sites	Annealing in an Ar atmosphere	Glycerol oxidation	DHA	26.5%	N/A	• Electrolyte: Na$_2$SO$_4$ (0.01 M) with glycerol (0.1 M) • Applied bias: 1.4 V$_{RHE}$ • Light: 300 W Xe lamp (100 mW cm^{-2})	288
Bi-rich BiVO$_{4-x}$/BiVO$_4$	Forming a Bi-rich surface with active sites for secondary hydroxyl adsorption	Chemical etching and electrochemical reduction	Glycerol oxidation	DHA	80.3%	N/A	• Electrolyte: Na$_2$SO$_4$ (0.01 M, pH adjusted to 2 with H$_2$SO$_4$) with glycerol (0.1 M) • Applied bias: 1.23 V$_{RHE}$ • Light: AM 1.5G (100 mW cm^{-2})	289
WO$_{3-x}$	Adsorption and activation sites for terminal hydroxyl	Annealed in an Ar/O$_2$ atmosphere and immersed in NaBH$_4$	Glycerol oxidation	GLAD	86.1%	N/A	• Electrolyte: glycerol (2 M, pH 2) • Applied bias: 1.2 V$_{RHE}$ • Light: AM 1.5G (100 mW cm^{-2})	290
CZTS/CdS	Adsorption energy modulation	Chemical bath, heat treatment in air and N$_2$ atmospheres	CO$_2$ reduction	CO, ethanol and methanol	2.31 (CO), 3 (ethanol) and 2 μmol cm^{-2} h^{-1} (methanol) production yield	N/A	• Electrolyte: CO$_2$-saturated KHCO$_3$ (0.1 M) • Applied bias: −0.6 V$_{RHE}$ (CO) and −0.4 V$_{RHE}$ (ethanol and methanol) • Light: AM 1.5G (100 mW cm^{-2})	292
239 WO$_3$-O$_{Vac}$	Cl$^-$ ion adsorption and Cl$_2$ production sites	Annealed in an H$_2$/Ar atmosphere	Procaine conversion	Chloroprocaine	N/A	92%	• Electrolyte: K$_2$SO$_4$ (0.5 M) or KCl • Applied bias: 1.0 V$_{RHE}$ • Light: AM 1.5G (100 mW cm^{-2})	294
Sn/TiO$_2$/Si	CO$_2$ molecule activation sites	Deposition of Sn	CO$_2$ reduction	Formate	N/A	69%	• Electrolyte: CO$_2$-saturated KHCO$_3$ • Applied bias: −1.0 V$_{RHE}$ • Light: AM 1.5G (100 mW cm^{-2})	298
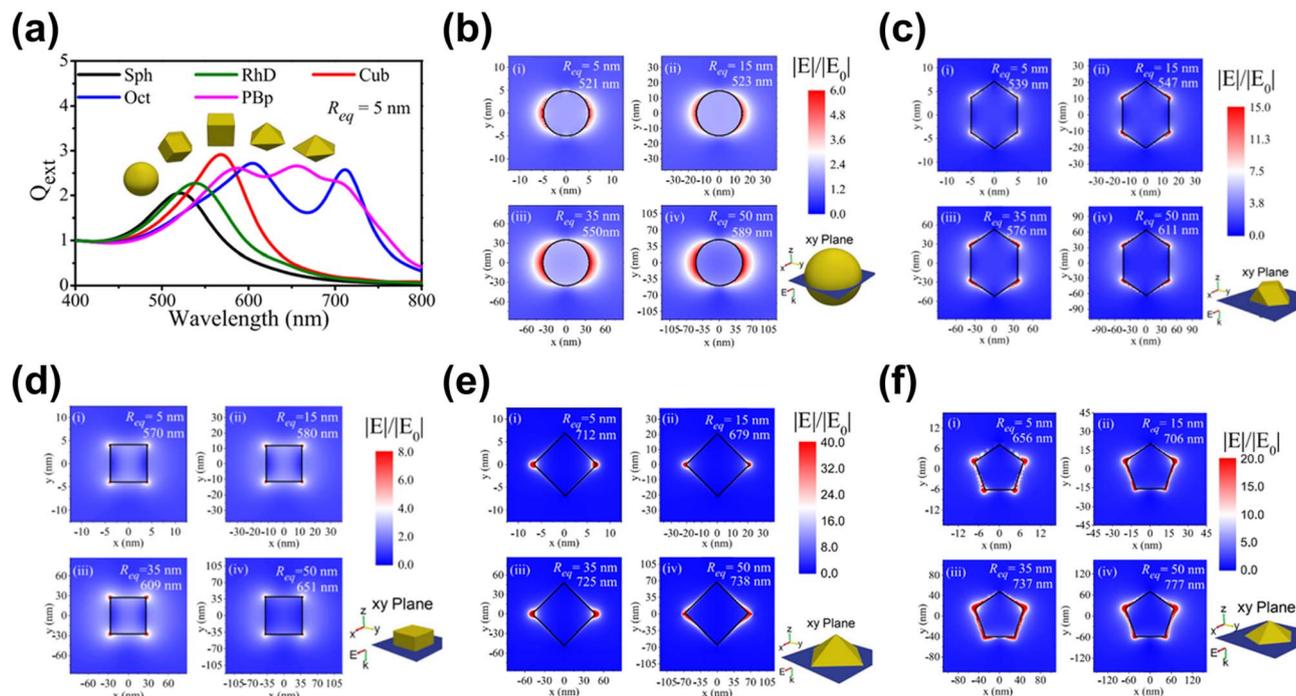
Fig. 21 Nanostructuring effects on the optical properties of materials. (a) Extinction properties of Au nanoparticles with different shapes: sphere (Sph), rhombic dodecahedron (RhD), cube (Cub), octahedron (Oct), and pentagonal bipyramid (PBp). Distribution of near field electric enhancement in the x–y plane at different equivalent radii (R_{eq}) of (b) Sph, (c) RhD, (d) Cub, (e) Oct, and (f) PBp Au nanoparticles. Optimizing nanoparticle shapes to achieve both the broadest light absorption and the highest, most widespread field enhancement is essential for enhancing the PEC performance of nanostructures. Adapted from ref. 310 with permission. Copyright 2019 American Chemical Society.

surface engineering demonstrates a faradaic efficiency of 64.9% for ammonia upon testing with nitrate-rich wastewater, making it a potential candidate for nitrate-contaminated wastewater treatment.

Adding to the versatility of vacancy and defect utilization in PEC biomass valorization, O_{Vac}-enriched WO_3 can be utilized to improve the conversion of procaine to sustainably produce chloroprocaine, a valuable chemical for medical applications.[294] The vacancies are induced through annealing in a H_2/Ar atmosphere (Fig. 20e). Through this approach, the system is capable of converting procaine to chloroprocaine with a selectivity of up to 92% (Fig. 20f). This improved selectivity stems from the Cl^- ions that are preferably adsorbed onto the vacancy-enriched WO_3, forming Cl^- enriched WO_3 and facilitating the ions to participate in the production of chloroprocaine. Complementing the catalytic activity, the O_{Vac} also increases the light absorption and charge transport ability, which also contributes to increased selectivity. All in all, these examples demonstrate the crucial role that surficial vacancies and defects play in enhancing and tuning PEC biomass and CO_2 valorization selectivity. By improving charge transfer and light absorption, as well as acting as and forming active sites for adsorption of reactants, surface vacancies and defects can selectively promote a specific reaction pathway, enhancing the selectivity. Despite these advantages, defect engineering also presents several limitations and challenges. Excessive or uncontrolled formation of defects, particularly in the bulk phase, can introduce trap states that hinder charge transport, reduce material

stability, and cause undesirable side reactions.[295] Moreover, the stability of defect-rich surfaces under prolonged PEC operation or in harsh reaction environments remains a concern, as vacancies may heal or evolve over time, leading to performance degradation.[296] The synthesis of defect-engineered materials is also often sensitive to processing conditions, which complicates reproducibility and scalability.[297] The utilization of surface vacancies and defects for PEC biomass and CO_2 valorization selectivity control and enhancement is summarized in Table 8.

3.4. Nanostructuring

Aside from heterostructuring and surficial atomic modulation, nanostructuring has emerged as another common approach for selectivity control in PEC biomass valorization. Nanostructuring enables precise tuning of surface area,[299,300] morphology,[301,302] and active site distribution,[303,304] which directly influences catalytic performance. Additionally, optimizing the shape and morphology of nanostructured materials enhances light harvesting, absorption, and scattering capabilities, further improving PEC performance.[305,306] For example, in water splitting, the photocurrent density of TiO_2 at 1.23 V_{RHE} varies significantly with structural complexity, increasing from 0D (0.02 mA cm^{-2}), 1D (0.7 mA cm^{-2}), 2D (0.44 mA cm^{-2}), and 3D (2.59 mA cm^{-2}).[307–309] The enhanced performance of the 3D structure can be attributed to their ability to improve light absorption and scattering, particularly at sharp edges and corners, which serve as charge separation and accumulation
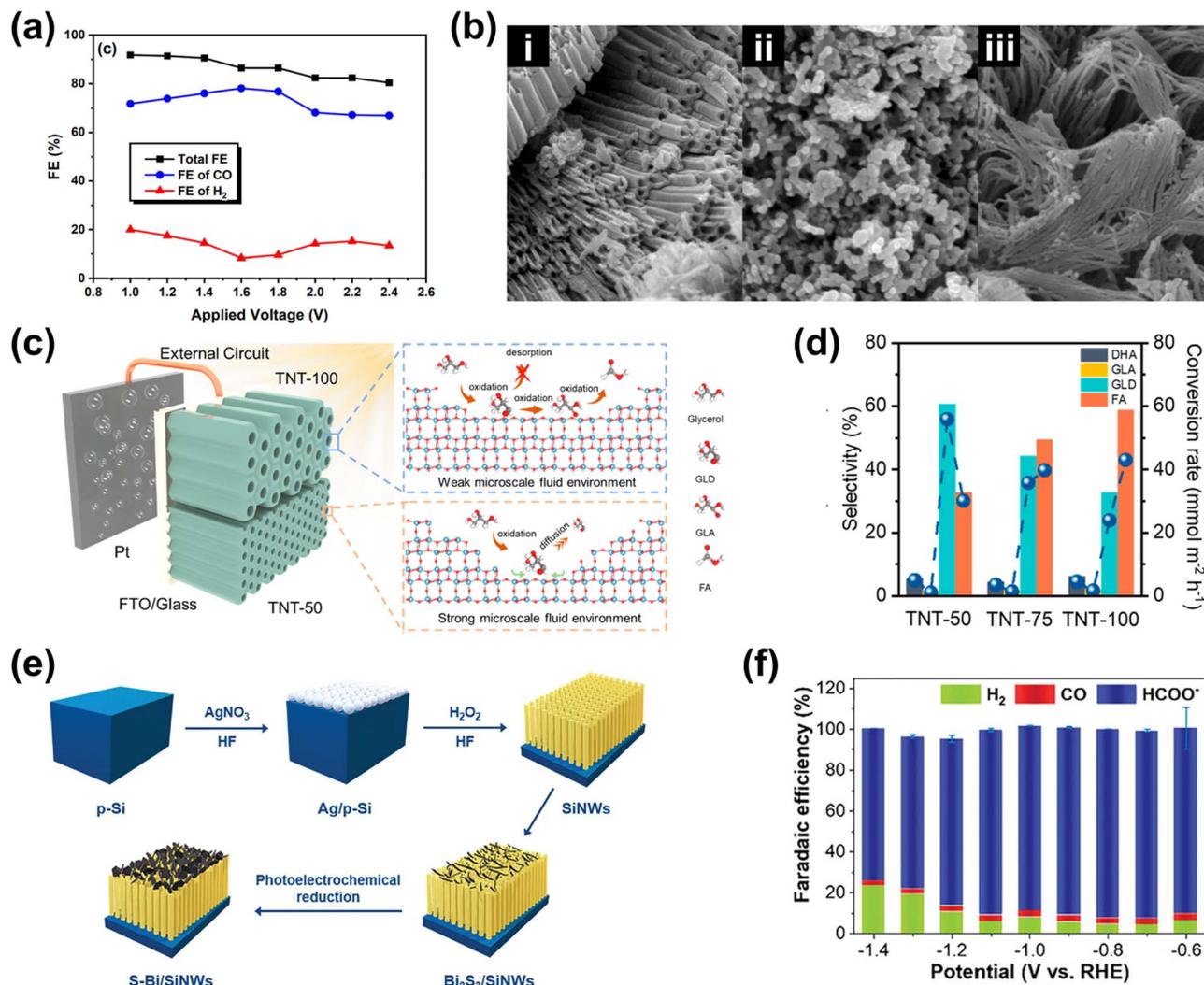
Fig. 22 Nanostructuring for PEC biomass valorization selectivity tuning. (a) PEC CO_2 reduction performance of nanostructured Ag nanocubes. Adapted from ref. 316 with permission. Copyright 2020 American Chemical Society. (b) Nanostructured TiO_2 in the form of (i) nanotubes, (ii) nanosponges, and (iii) nanobelts for PEC glycerol oxidation. Adapted from ref. 321 with permission. Copyright 2022 Elsevier Ltd. (c) Architecture of inner diameter-modulated TiO_2 nanotubes (TNTs) and illustration of the microscale fluid effect. (d) PEC glycerol oxidation product selectivity and conversion rate for inner diameter-modulated TNT photoelectrodes. Adapted from ref. 322 with permission. Copyright 2024 American Chemical Society. (e) Preparation steps for nanostructured S−Bi nanosheets on Si NWs. (f) PEC CO_2 reduction product FE on the S−Bi nanosheet-deposited Si NW photoelectrode. Adapted from ref. 323. Copyright 2024 The Author(s).

sites. The sharp edges and corners in certain shapes, such as cubes, octahedrons, or pyramids, often serve as sites for charge separation and accumulation. Furthermore, nanostructuring plasmonic nanoparticles into varying shapes, such as spheres, rods, cubes, or dendritic structures, could provide unique localized surface plasmon resonance (LSPR) characteristics that can enhance light absorption and scattering. As a result, this enhancement would increase the local electromagnetic field near the catalyst surface, which could ultimately contribute to boosting photocatalytic activity and generating hotspots that can selectively drive specific reaction pathways. The influence of morphology on the near-electric field distribution of plasmonic nanoparticles has been demonstrated in various metal nanoparticles.[310–315] Theoretical calculations show that the more localized the electrons or plasmons, the stronger the near-

electric field, leading to brighter hotspots. As shown in Fig. 21a–f, among polyhedral Au nanoparticles, octahedral structures exhibit the highest electric field enhancement. However, the enhancement is concentrated in a relatively small region compared to other morphologies with a broader near-field distribution. Additionally, as nanoparticle shapes deviate from spherical forms, their absorption domain broadens, covering a wider wavelength range, which is advantageous for PEC biomass valorization.

Aside from leveraging the optical property tunability to improve PEC biomass valorization, nanostructuring also facilitates enhanced catalytic reactions by modifying surface interactions. For instance, nanostructuring Ag into Ag nanocubes with exposed (100) planes effectively suppresses H_2 production by preferentially adsorbing CO_2, thereby improving CO_2

Table 9 Summary of nanostructuring for PEC biomass valorization selectivity enhancement and tuning applications

Photoelectrode[a]	Role of nanostructuring	Method	Reaction	Target product(s)	Selectivity	FE	Reaction conditions	Ref.
Ag NCs/MCA	Increase CO_2 adsorption by exposing the (100) plane	Sulfide-mediated polyol method	CO_2 reduction	CO	N/A	80%	• Electrolyte: CO_2-saturated $KHCO_3$ (0.5 M) • Applied bias: 1.6 V • Light: AM 1.5G (100 mW cm^{-2})	316
NT-TiO$_2$	Increasing active surface area	Anodic oxidation in a solution containing 2% volume of water and 98% volume of ethylene glycol and calcination	Glycerol oxidation	GLAD, DHA, and FA	31% (GLAD), 13% (DHA), and 5.7% (FA)	N/A	• Electrolyte: Na_2SO_4 (5 mM) with glycerol (10 mM) • Applied bias: 0.5 V_{RHE} • Light: 8 W UVA fluorescent lamp	321
NS-TiO$_2$	Increasing active surface area	Anodic oxidation in a solution containing 40% water and 60% glycerol and calcination	Glycerol oxidation	GLAD, DHA, and FA	32% (GLAD), 12% (DHA), and 6.7% (FA)	N/A	• Electrolyte: Na_2SO_4 (5 mM) with glycerol (10 mM) • Applied bias: 0.5 V_{RHE} • Light: 8 W UVA fluorescent lamp	321
NB-TiO$_2$	Increasing active surface area	Anodic oxidation in a solution containing 5% water and 95% glycerol and calcination	Glycerol oxidation	GLAD, DHA, and FA	31% (GLAD), 13% (DHA), and 7.0% (FA)	N/A	• Electrolyte: Na_2SO_4 (5 mM) with glycerol (10 mM) • Applied bias: 0.5 V_{RHE} • Light: 8 W UVA fluorescent lamp	321
TNT-50	Modulating product diffusion through induced microscale fluid environments	Titanium foil anodization	Glycerol oxidation	GLAD	60.7%	N/A	• Electrolyte: Na_2SO_4 (0.5 M) with glycerol (0.1 M) • Applied bias: 1.23 V_{RHE} • Light: AM 1.5G (100 mW cm^{-2})	322
TNT-100	Modulating product diffusion through induced microscale fluid environments	Titanium foil anodization	Glycerol oxidation	FA	60%	N/A	• Electrolyte: Na_2SO_4 (0.5 M) with glycerol (0.1 M) • Applied bias: 1.23 V_{RHE} • Light: AM 1.5G (100 mW cm^{-2})	322
S–Bi/Si NWs	Improving charge transport from Si NWs	PEC reduction	CO_2 reduction	Formate	N/A	93%	• Electrolyte: CO_2-saturated $KHCO_3$ (0.1 M) • Applied bias: −0.8 V_{RHE} • Light: AM 1.5G (100 mW cm^{-2})	323
WO$_3$/TiO$_2$	Improves charge separation efficiency, extends light absorption, and provides adsorption and desorption sites	Hydrothermal	Glycerol oxidation	GLAD and DHA	61% (GLAD) and 92% (GLAD and DHA)	N/A	• Electrolyte: Na_2SO_4 (0.1 M) with glycerol (0.05 M) • Applied bias: 1.23 V_{RHE} • Light: AM 1.5G (100 mW cm^{-2})	328
Au NW	Promoting adsorption of middle hydroxyl groups of glycerol	Electrodeposition	Glycerol oxidation	Lactic acid	80%	N/A	• Electrolyte: KOH (3 M) with glycerol • Applied bias: 0.95 V_{RHE} • Light: AM 1.5G (300 mW cm^{-2})	329

[a] NC: nanocube, MCA: membrane cathode, NB: nanobelt, NS: nanosponge, NT: nanotube, NW: nanowire, and TNT: TiO$_2$ nanotube.

reduction selectivity towards CO (Fig. 22a).[316] This demonstrates how tuning the nanoparticle shape and facet exposure can significantly impact selectivity in PEC processes. Moreover, the surface-to-volume ratio and active site density can be modulated by designing catalysts with unique nanoscale architectures such as nanorods, nanowires, or nanoporous structures.[317–320] This approach creates microenvironments that enhance adsorption and activation of specific intermediates, steering reactions toward desired products. For example, TiO_2 nanostructuring into nanotubes, nanosponges, and nanobelts (Fig. 22b(i–iii)) has been shown to improve conversion efficiency and selectivity in PEC glycerol oxidation, yielding value-added products such as glyceraldehyde (GLAD), dihydroxyacetone (DHA), and formic acid (FA).[321]

Furthermore, the geometric and spatial arrangement of nanoscale features could also impose steric constraints that favor certain reaction pathways while suppressing competing reactions. Consequently, this could also further contribute to the alteration of selectivity. Notably, for TiO_2 nanotubes, it has been demonstrated that further nanostructuring, in the form of varying inner diameters, has a significant effect on the reaction kinetics, particularly for PEC glycerol oxidation.[322] The microenvironment of nanotubes allows for the diffusion of molecules (Fig. 22c). In the case of decreasing the inner diameter of the nanotubes, the strength of the microenvironment, in the form of microscale fluid effect, is increased. Thus, the diffusion of the oxidation products is heightened, allowing the reaction to produce multi-carbon products. However, when the inner diameter is increased, this effect is weakened and the oxidation product desorption from the system is sluggish, allowing further oxidation. This unique nanostructuring-enabled reaction mechanism allows for selectivity tuning of the system to single-carbon products, FA, or multi-carbon products, GLAD (Fig. 22d).

We also note that nanostructuring could also facilitate efficient charge carrier separation and transport. This is primarily due to the reduction in the distance of photogenerated carriers and reaction sites, which are responsible for suppressing charge recombination.[236,324] For instance, nanostructuring Bi_2S_3 to Bi nanoplates can help mitigate surface charge recombination of Si nanowires (NWs) (Fig. 22e).[323] In multi-electron reactions, such as CO_2 reduction, enlarging the junction area of semiconductors such as nanowires is expected to boost the photocurrent by reducing the travel distance of the minority carriers. However, excessive area augmentation can increase surface recombination, lowering open-circuit potential and reducing catalytic activity. In this approach, the S–Bi nanosheet rapidly extracts photogenerated electrons from the Si NWs and facilitates CO_2 reduction on its surface. Therefore, with the enhanced charge transport, the photoelectrodes allow for improved selectivity towards formate (Fig. 22f).

In summary, nanostructuring is a powerful tool for improving and tuning PEC biomass and CO_2 valorization selectivity through optical property modulation, electronic structure tailoring, and modifying interactions with reactants. By carefully nanostructuring photoelectrodes, researchers can manipulate optical, electronic, and catalytic properties to achieve higher efficiency and selectivity in PEC reactions. This approach not only enables precise control over reaction pathways but also paves the way for developing advanced photoelectrodes tailored for PEC biomass and CO_2 valorization. Despite its significant advantages, nanostructuring also presents several challenges that must be carefully managed. Complex nanostructures often require intricate synthetic procedures, which can limit scalability, reproducibility, and cost-effectiveness.[325] Stability is another key concern, as nanostructured materials with high surface energy or delicate morphologies may degrade or restructure under operational PEC conditions, diminishing long-term performance.[326] Additionally, the interplay between morphology and selectivity is highly system-specific, and the mechanistic understanding of how nanostructure-induced microenvironments alter reaction kinetics remains incomplete.[327] Therefore, achieving reproducible, durable, and mechanistically sound nanostructure designs requires careful balancing of structural complexity, material stability, and application-specific requirements. The utilization of nanostructuring for PEC biomass and CO_2 valorization selectivity enhancement and tuning is summarized in Table 9.

4. Conclusions and outlook

The advancement of PEC biomass valorization has been significantly driven by surface engineering strategies, which play a crucial role in modulating the catalytic and electronic properties of photoelectrodes. Approaches such as surface functionalization, crystal facet tuning, defect engineering, and nanostructuring offer distinct advantages in enhancing selective PEC biomass valorization. In this review, we have comprehensively summarized and discussed how these strategies contribute to PEC biomass valorization selectivity through three key roles: first, they enhance charge generation, separation, and transport to reactants. Cocatalysts such as nanoparticles, quantum dots, and single-atom metals serve as electron or hole sinks, reducing recombination losses and directing carriers toward desired reaction sites. Second, they improve light absorption, particularly through surface functionalization, where cocatalysts, such as nanoparticles, quantum dots, and single-atom metals, serve as effective light harvesters. Surface decorations broaden the light absorption range through synergistic optical interactions. Plasmonic nanoparticles, quantum-confined dots, and tailored nanostructures increase photoresponse in the visible and near-infrared regions, while also amplifying local electromagnetic fields. Lastly, surface engineering plays a pivotal role in selectivity tuning by modulating photoelectrode-reactant interactions. Several studies have demonstrated that engineered surfaces can selectively generate active sites for specific molecules or key intermediates, thereby influencing reaction pathways. Among these strategies, crystal facet tuning and defect engineering, in particular, have demonstrated the ability to generate site-specific interactions, enabling high product selectivity.

Despite these advancements, several critical challenges must be addressed to fully realize the potential of surface engineering for scalable PEC biomass and CO_2 valorization. One aspect is

combining multiple surface engineering techniques, which could further open opportunities to amplify beneficial effects and achieve finer selectivity control.[330] Furthermore, modified surfaces, in particular with molecular co-catalysts, often suffer from degradation under prolonged PEC operation. Additionally, nanostructured materials may degrade or restructure under operational PEC conditions. Addressing these stability issues will require the development of protective coatings, self-healing materials, or dynamically adaptive interfaces.[331–333] Moreover, translating laboratory-scale strategies to large-scale practical systems demands scalable, cost-effective synthesis methods that maintain precise control over morphology, composition, and surface features.[334,335] Simplifying complex fabrication processes without compromising performance is a key step toward commercial deployment, in particular for sophisticated surface engineering strategies such as single-atom metal. Additionally, deeper mechanistic insight into how surface modifications influence reaction intermediates, charge carrier dynamics, and microenvironmental conditions is essential. Advances in *operando* characterization and theoretical modeling will be instrumental in guiding rational design. Finally, to enable broader applicability, it is also essential to develop generalized surface engineering strategies that can be effectively applied to both oxidation and reduction half-reactions. Many current modifications are highly reaction-specific, and a more universal approach would facilitate the design of integrated PEC systems for complete biomass conversion or coupled CO_2 reduction and biomass oxidation. All in all, by addressing current challenges, surface-engineered PEC systems can be further advanced into a more versatile and efficient platform for selective biomass and CO_2 valorization.

Author contributions

Y. T. A., F. F. A., and F. A. A. N. conceived the idea and defined the structure of the review. All authors contributed to the writing, reviewing, and editing of the manuscript. F. F. A. and F. A. A. N. supervised the overall project.

Conflicts of interest

The authors declare no conflict of interest.

Data availability

No primary research results, software or code have been included in this review.

Acknowledgements

References

1 K. Li and B. Lin, *Renewable Sustainable Energy Rev.*, 2015, **52**, 1107–1122.

2 Q. Fu, L. Liu and H. Wang, *Resour. Policy*, 2023, **86**, 104126.

3 Q. Wang and K. Zhou, *Appl. Energy*, 2017, **188**, 19–31.

4 F. C. Robert, G. S. Sisodia and S. Gopalan, *Sustain. Cities Soc.*, 2018, **40**, 735–745.

5 S. Kaza, L. C. Yao, P. Bhada-Tata and F. Van Woerden, *What a Waste 2.0: A Global Snapshot of Solid Waste Management to 2050*, World Bank, Washington, DC, 2018.

6 I. S. W. A. United Nations Environment Programme, *Global Waste Management Outlook 2024 – Beyond an age of waste: Turning Rubbish into a Resource*, 2024.

7 N. F. Islam, B. Gogoi, R. Saikia, B. Yousaf, M. Narayan and H. Sarma, *Reg. Sustainability*, 2024, **5**, 100174.

8 Q. Kanwal, X. Zeng and J. Li, *Humanit. Soc. Sci. Commun.*, 2023, **10**, 471.

9 D. Sun, Y. Zhang, Y. Zhou, Y. Nie, L. Ban, D. Wu, S. Yang, H. Zhang, C. Li and K. Zhang, *Adv. Energy Mater.*, 2025, **15**, 2406098.

10 L. Qin, M. Wang, J. Zhu, Y. Wei, X. Zhou and Z. He, *Complexity*, 2021, **2021**, 5822568.

11 N. C. Joshi, S. Sinha, P. Bhatnagar, Y. Nath, B. Negi, V. Kumar and P. Gururani, *Curr. Res. Microb. Sci.*, 2024, **6**, 100237.

12 J. Cai, N. Lin, Y. Li, J. Xue, F. Li, L. Wei, M. Yu, X. Zha and W. Li, *J. Anal. Appl. Pyrolysis*, 2024, **177**, 106321.

13 M. V. Barros, R. Salvador, A. C. de Francisco and C. M. Piekarski, *Renewable Sustainable Energy Rev.*, 2020, **131**, 109958.

14 B. Segers, P. Nimmegeers, M. Spiller, G. Tofani, E. Jasiukaitytė-Grojzdek, E. Dace, T. Kikas, J. M. Marchetti, M. Rajić, G. Yildiz and P. Billen, *RSC Sustainability*, 2024, **2**, 3730–3749.

15 F. W. S. Lucas, R. G. Grim, S. A. Tacey, C. A. Downes, J. Hasse, A. M. Roman, C. A. Farberow, J. A. Schaidle and A. Holewinski, *ACS Energy Lett.*, 2021, 1205–1270.

16 S. Katre, P. Baghmare and A. S. Giri, *Nanoscale Adv.*, 2024, **6**, 5258–5284.

17 A. N. Wilson, A. Dutta, B. A. Black, C. Mukarakate, K. Magrini, J. A. Schaidle, W. E. Michener, G. T. Beckham and M. R. Nimlos, *Green Chem.*, 2019, **21**, 4217–4230.

18 Y. Wang and J. J. Wu, *Renewable Sustainable Energy Rev.*, 2023, **187**, 113754.

19 Z. Sun, J. Cheng, D. Wang, T. Yuan, G. Song and K. Barta, *ChemSusChem*, 2020, **13**, 5199–5212.

20 C. Jin, M. Han, Y. Wu and S. Wang, *Energy Environ. Sci.*, 2024, **17**, 7459–7511.

21 A. Vilanova, P. Dias, T. Lopes and A. Mendes, *Chem. Soc. Rev.*, 2024, **53**, 2388–2434.

22 B. Zhang, H. Zhang, Y. Pan, J. Shao, X. Wang, Y. Jiang, X. Xu and S. Chu, *Chem. Eng. J.*, 2023, **462**, 142247.

23 L. Wen, X. Zhang and F. F. Abdi, *Mater. Today Energy*, 2024, **44**, 101648.

24 J.-Y. Cui, T.-T. Li, Z.-H. Yin, L. Chen and J.-J. Wang, *Chem. Eng. J.*, 2024, **493**, 152461.

25 J. Yu, J. González-Cobos, F. Dappozze, F. J. López-Tenllado, J. Hidalgo-Carrillo, A. Marinas, P. Vernoux, A. Caravaca and C. Guillard, *Appl. Catal., B*, 2022, **318**, 121843.

26 Y. Jung, S. Kim, H. Choi, Y. Kim, J. B. Hwang, D. Lee, Y. Kim, J.-C. Park, D.-Y. Kim and S. Lee, *Nanomaterials*, 2023, **13**, 1690.

27 R. Ciriminna, A. Fidalgo, L. M. Ilharco and M. Pagliaro, *ChemistryOpen*, 2018, **7**, 233–236.

28 G. Kongprawes, D. Wongsawaeng, P. Hosemann, K. Ngaosuwan, W. Kiatkittipong and S. Assabumrungrat, *Sci. Rep.*, 2024, **14**, 31295.

29 Q. Yan, Y. Chen, B. Tang, X. Wu, H. Zhou, H. Wang, H. Li, L. Lu, H. Zhang, S. Yang, C. Xu and T. Ma, *Angew. Chem., Int. Ed.*, 2025, **64**, e202505718.

30 K. Lu, Y. Zhang, Y. Shen and H. Li, *Catal. Sci. Technol.*, 2024, **14**, 2973–2990.

31 F. Amano, S. Suzuki, K. Tsushiro, J. Ito, T. Naito and H. Kubota, *ACS Appl. Mater. Interfaces*, 2024, **16**, 24631–24640.

32 V. Kumaravel, J. Bartlett and S. C. Pillai, *ACS Energy Lett.*, 2020, **5**, 486–519.

33 C. Dong, C. Lin, P. Li, J. H. Park, J. Shen and K. Zhang, *Angew. Chem., Int. Ed.*, 2025, **64**, e202423730.

34 G. Zeng, G. Liu, G. Panzeri, C. Kim, C. Song, O. J. Alley, A. T. Bell, A. Z. Weber and F. M. Toma, *ACS Energy Lett.*, 2025, **10**, 34–39.

35 A. Amirjani, N. B. Amlashi and Z. S. Ahmadiani, *ACS Appl. Nano Mater.*, 2023, **6**, 9085–9123.

36 A. R. Fareza, F. A. A. Nugroho and V. Fauzia, *ACS Appl. Nano Mater.*, 2022, **5**, 16051–16060.

37 C. Jiang, Y. Ding, J. Lin, Y. Sun, W. Zhou, X. Zhang, H. Zhao, W. Cao and D. Cheng, *Dalton Trans.*, 2025, **54**, 2460–2470.

38 F. R. H. Rayanisaputri, D. Aryanto, L. Bijelić, A. Susarrey-Arce, F. Ruiz-Zepeda, F. A. A. Nugroho and V. Fauzia, *ACS Appl. Nano Mater.*, 2025, **8**, 1479–1489.

39 D. Liu, X. Wan, T. Kong, W. Han and Y. Xiong, *J. Mater. Chem. A*, 2022, **10**, 5878–5888.

40 P. Prabha Sarangi, D. Prava Sahoo, U. Aparajita Mohanty, S. Nayak and K. Parida, *ChemCatChem*, 2024, **16**, e202301533.

41 R. Wang, Y. Kuwahara, K. Mori and H. Yamashita, *ChemCatChem*, 2021, **13**, 5058–5072.

42 A. R. Fareza, L. Roza, F. A. A. Nugroho and V. Fauzia, *Surf. Interfaces*, 2023, **37**, 102663.

43 L. T. Samosir, F. A. A. Nugroho and V. Fauzia, *Electrochim. Acta*, 2024, **496**, 144483.

44 X. Wu, Q. Yan, H. Wang, D. Wu, H. Zhou, H. Li, S. Yang, T. Ma and H. Zhang, *Adv. Funct. Mater.*, 2024, **34**, 2404535.

45 L. Ban, Y. Zhang, D. Sun, Y. Zhou, Y. Li, C. Xu, S. Yang and H. Zhang, *Adv. Funct. Mater.*, 2025, 2506114.

46 Q. Li, J. Li, H. Bai and F. Li, *Chin. J. Catal.*, 2024, **58**, 86–104.

47 X. Li, Y. Sun, F. Ren, Y. Bai and Z. Cheng, *Mater. Today Energy*, 2021, **19**, 100619.

48 J. Wang, K. Liu, W. Liao, Y. Kang, H. Xiao, Y. Chen, Q. Wang, T. Luo, J. Chen, H. Li, T.-S. Chan, S. Chen, E. Pensa, L. Chai, F. Liu, L. Jiang, C. Liu, J. Fu, E. Cortés and M. Liu, *Nat. Catal.*, 2025, **8**, 229–238.

49 Y. An, T. Lei, W. Jiang and H. Pang, *Green Chem.*, 2024, **26**, 10739–10773.

50 G. Zhou, Z. Wang, J. Gong, S. Shen and W. Zhong, *Chem. Sci.*, 2025, **16**, 12718–12767.

51 H. Liang, M. Li, Z. Li, W. Xie, T. Zhang and Q. Wang, *J. CO₂ Util.*, 2024, **79**, 102639.

52 V. Kumaravel, J. Bartlett and S. C. Pillai, *ACS Energy Lett.*, 2020, **5**, 486–519.

53 S. Tang, W. Qiu, S. Xiao, Y. Tong and S. Yang, *Energy Environ. Sci.*, 2020, **13**, 660–684.

54 D. Li, Y. Liu, W. Shi, C. Shao, S. Wang, C. Ding, T. Liu, F. Fan, J. Shi and C. Li, *ACS Energy Lett.*, 2019, **4**, 825–831.

55 L. Yao, A. Rahmanudin, N. Guijarro and K. Sivula, *Adv. Energy Mater.*, 2018, **8**, 1802585.

56 Y. Zhang, C. Pan, G. Bian, J. Xu, Y. Dong, Y. Zhang, Y. Lou, W. Liu and Y. Zhu, *Nat. Energy*, 2023, **8**, 361–371.

57 S. Corby, R. R. Rao, L. Steier and J. R. Durrant, *Nat. Rev. Mater.*, 2021, **6**, 1136–1155.

58 A. J. Bard, L. R. Faulkner and H. S. White, *Electrochemical Methods: Fundamentals and Applications*, Wiley, 3rd edn, 2022.

59 H. Kong, S. Gupta, A. F. Pérez-Torres, C. Höhn, P. Bogdanoff, M. T. Mayer, R. van de Krol, M. Favaro and F. F. Abdi, *Chem. Sci.*, 2024, **15**, 10425–10435.

60 J. Wu, J. Li, Y. Li, X. Ma, W. Zhang, Y. Hao, W. Cai, Z. Liu and M. Gong, *Angew. Chem., Int. Ed.*, 2021, **61**, e202113362.

61 L. A. Larew and D. C. Johnson, *J. Electroanal. Chem. Interfacial Electrochem.*, 1989, **262**, 167–182.

62 J. Zhao, W. Jing, T. Tan, X. Liu, Y. Kang and W. Wang, *New J. Chem.*, 2020, **44**, 4604–4612.

63 J. Ouyang, X. Liu, B.-H. Wang, J.-B. Pan, S. Shen, L. Chen, C.-T. Au and S.-F. Yin, *ACS Appl. Mater. Interfaces*, 2022, **14**, 23536–23545.

64 M. G. Walter, E. L. Warren, J. R. McKone, S. W. Boettcher, Q. Mi, E. A. Santori and N. S. Lewis, *Chem. Rev.*, 2010, **110**, 6446–6473.

65 M. Simões, S. Baranton and C. Coutanceau, *ChemSusChem*, 2012, **5**, 2106–2124.

66 J. R. Hemmerling, A. Mathur and S. Linic, *Acc. Chem. Res.*, 2021, **54**, 1992–2002.

67 X. Liu, X. He, D. Xiong, G. Wang, Z. Tu, D. Wu, J. Wang, J. Gu and Z. Chen, *ACS Catal.*, 2024, **14**, 5366–5376.

68 D. Liu, J.-C. Liu, W. Cai, J. Ma, H. Bin Yang, H. Xiao, J. Li, Y. Xiong, Y. Huang and B. Liu, *Nat. Commun.*, 2019, **10**, 1779.

69 H. Kong, S. Gupta, A. F. Pérez-Torres, C. Höhn, P. Bogdanoff, M. T. Mayer, R. van de Krol, M. Favaro and F. F. Abdi, *Chem. Sci.*, 2024, **15**, 10425–10435.

70 K. Kobayashi, S. N. Lou, Y. Takatsuji, T. Haruyama, Y. Shimizu and T. Ohno, *Electrochim. Acta*, 2020, **338**, 135805.

71 W. Wang and L. Qi, *Adv. Funct. Mater.*, 2019, **29**, 1807275.

72 X. Zhao, W. Luo, J. Feng, M. Li, Z. Li, T. Yu and Z. Zou, *Adv. Energy Mater.*, 2014, **4**, 1301785.

73 J. U. Kim, H. S. Han, J. Park, W. Park, J. H. Baek, J. M. Lee, H. S. Jung and I. S. Cho, *J. Catal.*, 2018, **365**, 138–144.

74 S. Wan, C. Dong, J. Jin, J. Li, Q. Zhong, K. Zhang and J. H. Park, *ACS Energy Lett.*, 2022, **7**, 3024–3031.

75 T. Zhang, P. Lin, N. Wei and D. Wang, *ACS Appl. Mater. Interfaces*, 2020, **12**, 20110–20118.

76 K. Zhu, S. K. Frehan, G. Mul and A. Huijser, *J. Am. Chem. Soc.*, 2022, **144**, 11010–11018.

77 S. Selim, E. Pastor, M. García-Tecedor, M. R. Morris, L. Francàs, M. Sachs, B. Moss, S. Corby, C. A. Mesa, S. Gimenez, A. Kafizas, A. A. Bakulin and J. R. Durrant, *J. Am. Chem. Soc.*, 2019, **141**, 18791–18798.

78 S. Wang, G. Liu and L. Wang, *Chem. Rev.*, 2019, **119**, 5192–5247.

79 Z. Liu, Y. Guo, Q. Ge and X. Zhu, *React. Chem. Eng.*, 2025, **10**, 750–767.

80 S. Su, I. Siretanu, D. van den Ende, B. Mei, G. Mul and F. Mugele, *J. Am. Chem. Soc.*, 2024, **146**, 2248–2256.

81 S. Su, I. Siretanu, D. van den Ende, B. Mei, G. Mul and F. Mugele, *Adv. Mater.*, 2021, **33**, 2106229.

82 J. Zhu, S. Pang, T. Dittrich, Y. Gao, W. Nie, J. Cui, R. Chen, H. An, F. Fan and C. Li, *Nano Lett.*, 2017, **17**, 6735–6741.

83 R. Chen, Z. Ren, Y. Liang, G. Zhang, T. Dittrich, R. Liu, Y. Liu, Y. Zhao, S. Pang, H. An, C. Ni, P. Zhou, K. Han, F. Fan and C. Li, *Nature*, 2022, **610**, 296–301.

84 J. Xiao, C. Li, X. Jia, J. Sun, F. Liubov, C. Liang, X. Zhang and B. Wang, *Electrochim. Acta*, 2024, **475**, 143643.

85 Y.-K. Hsu, Y.-G. Lin and Y.-C. Chen, *Electrochem. Commun.*, 2011, **13**, 1383–1386.

86 Z. Li, L. Zhang, Y. Liu, C. Shao, Y. Gao, F. Fan, J. Wang, J. Li, J. Yan, R. Li and C. Li, *Angew. Chem., Int. Ed.*, 2020, **59**, 935–942.

87 K. Zhu, A. P. Rodríguez, M. B. Brands, T. de Haas, F. Buda, J. N. H. Reek, G. Mul and A. Huijser, *Adv. Sci.*, 2024, **11**, 2403454.

88 W.-J. Liu, Z. Xu, D. Zhao, X.-Q. Pan, H.-C. Li, X. Hu, Z.-Y. Fan, W.-K. Wang, G.-H. Zhao, S. Jin, G. W. Huber and H.-Q. Yu, *Nat. Commun.*, 2020, **11**, 265.

89 A. Medrano-Banda, E. Ginoux, T. Faverge, A. Oshchepkov, A. Bonnefont, M. Chatenet, C. Coutanceau, G. Kéranguéven, P. Cognet and E. Savinova, *Electrochim. Acta*, 2024, **487**, 144159.

90 N. Schlegel, A. Bagger, J. Rossmeisl and M. Arenz, *J. Phys. Chem. C*, 2023, **127**, 18609–18618.

91 T. H. Kwan, K. L. Ong, M. A. Haque, S. Kulkarni and C. S. K. Lin, *Process Saf. Environ. Prot.*, 2019, **121**, 194–208.

92 N. Akkarawatkhoosith, A. Jaree, C. Yoocham, T. Damrongsakul and T. Tongtummachat, *J. Environ. Chem. Eng.*, 2024, **12**, 111646.

93 Ü. Ünlü, M. E. Oruc and Ö. Yücel, *Chem. Eng. J.*, 2025, **509**, 161280.

94 L. Zheng, P. Xu, Y. Zhao, Z. Bao, X. Luo, X. Shi, Q. Wu and H. Zheng, *Appl. Catal., B*, 2023, **331**, 122679.

95 J. Qiu, T. Forbes and T. Lin, *Chem. Commun.*, 2025, **61**, 3421–3435.

96 S. G. Lee, M. J. Kang, M. Park, K. Kim, H. Lee and H. S. Kim, *Appl. Catal., B*, 2022, **304**, 120967.

97 C. Zhang, Z. Lin, L. Jiao and H. Jiang, *Angew. Chem., Int. Ed.*, 2024, **63**, e202414506.

98 M. Checa, S. Nogales-Delgado, V. Montes and J. M. Encinar, *Catalysts*, 2020, **10**, 1–41.

99 Z.-C. Hu, Y.-G. Zheng and Y.-C. Shen, *Bioresour. Technol.*, 2011, **102**, 7177–7182.

100 X. Han, H. Sheng, C. Yu, T. W. Walker, G. W. Huber, J. Qiu and S. Jin, *ACS Catal.*, 2020, **10**, 6741–6752.

101 K. Fernández-Caso, G. Díaz-Sainz, M. Alvarez-Guerra and A. Irabien, *ACS Energy Lett.*, 2023, **8**, 1992–2024.

102 D. Du, R. Lan, J. Humphreys and S. Tao, *J. Appl. Electrochem.*, 2017, **47**, 661–678.

103 A. Irabien, M. Alvarez-Guerra, J. Albo and A. Dominguez-Ramos, in *Electrochemical Water and Wastewater Treatment*, Elsevier, 2018, pp. 29–59.

104 A. Mendoza, R. Romero, G. P. Gutiérrez-Cedillo, G. López-Tellez, O. Lorenzo-González, R. M. Gómez-Espinosa and R. Natividad, *Catal. Today*, 2020, **358**, 149–154.

105 A. Behr, J. Eilting, K. Irawadi, J. Leschinski and F. Lindner, *Green Chem.*, 2008, **10**, 13–30.

106 A. C. Brix, D. M. Morales, M. Braun, D. Jambrec, J. R. C. Junqueira, S. Cychy, S. Seisel, J. Masa, M. Muhler, C. Andronescu and W. Schuhmann, *ChemElectroChem*, 2021, **8**, 2336–2342.

107 P. Saini, M. Arora and M. N. V. R. Kumar, *Adv. Drug Delivery Rev.*, 2016, **107**, 47–59.

108 W. P. Smith, *J. Am. Acad. Dermatol.*, 1996, **35**, 388–391.

109 N. Madnani and K. Khan, *Indian J. Dermatol., Venereol. Leprol.*, 2013, **79**, 654.

110 M. Ai and K. Ohdan, *Appl. Catal., A*, 1997, **150**, 13–20.

111 V. C. Ghantani, S. T. Lomate, M. K. Dongare and S. B. Umbarkar, *Green Chem.*, 2013, **15**, 1211.

112 X. Bai, Q. Hou, H. Qian, Y. Nie, T. Xia, R. Lai, G. Yu, M. Laiq Ur Rehman, H. Xie and M. Ju, *Appl. Catal., B*, 2022, **303**, 120895.

113 S. Solmi, C. Morreale, F. Ospitali, S. Agnoli and F. Cavani, *ChemCatChem*, 2017, **9**, 2797–2806.

114 S. T. Al-Absi, K. Bashir, M. Abbotsi-Dogbey, Q. Zhang, D. Zhang, J. Liu, A. Mohamed, M. Yassien, W. Yan and X. Jin, *Ind. Eng. Chem. Res.*, 2025, **64**, 10101–10116.

115 H. G. Cha and K.-S. Choi, *Nat. Chem.*, 2015, **7**, 328–333.

116 K. Han, B. C. Rowley, M. P. Schellekens, S. Brugman, M. P. de Heer, L. P. S. Keyzer and P. J. Corbett, *ACS Energy Lett.*, 2024, **9**, 2800–2806.

117 Z. Liu, J. Qian, G. Zhang, B. Zhang and Y. He, *Sep. Purif. Technol.*, 2024, **330**, 125177.

118 F.-Y. Gao, R.-C. Bao, M.-R. Gao and S.-H. Yu, *J. Mater. Chem. A*, 2020, **8**, 15458–15478.

119 Y. Chiou, K. Juchniewicz, K. R. Kupiec, A. Mikolajczuk-Zychora, B. Mierzwa, H. Lin and A. Borodzinski, *ChemElectroChem*, 2021, **8**, 3348–3359.

120 X. Yu and P. G. Pickup, *J. Power Sources*, 2008, **182**, 124–132.

121 S. Saini, P. paramita Samal, S. Krishnamurty, A. Ray and S. L. Jain, *Green Chem.*, 2021, **23**, 9048–9060.

122 W. Ahmad, P. Koley, S. Dwivedi, R. Lakshman, Y. K. Shin, A. C. T. van Duin, A. Shrotri and A. Tanksale, *Nat. Commun.*, 2023, **14**, 2821.

123 C. Zhan, X. Li, G. Lan, E. E. K. Baidoo, Y. Yang, Y. Liu, Y. Sun, S. Wang, Y. Wang, G. Wang, J. Nielsen, J. D. Keasling, Y. Chen and Z. Bai, *Nat. Catal.*, 2023, **6**, 435–450.

124 T. Biswal, K. P. Shadangi, P. K. Sarangi and R. K. Srivastava, *Chemosphere*, 2022, **298**, 134299.

125 T. J. Deka, A. I. Osman, D. C. Baruah and D. W. Rooney, *Environ. Chem. Lett.*, 2022, **20**, 3525–3554.

126 A. Catarina Faria, C. V. Miguel, A. F. P. Ferreira, A. E. Rodrigues and L. M. Madeira, *Chem. Eng. J.*, 2023, **476**, 146539.

127 Z. Xu, R. Lu, Z.-Y. Lin, W. Wu, H.-J. Tsai, Q. Lu, Y. C. Li, S.-F. Hung, C. Song, J. C. Yu, Z. Wang and Y. Wang, *Nat. Energy*, 2024, **9**, 1397–1406.

128 S. Romegialli, A. Tripodi, A. Gramegna, M. Tommasi, G. Ramis and I. Rossetti, *Ind. Eng. Chem. Res.*, 2025, **64**, 190–208.

129 W. Ni, H. Chen, N. Tang, T. Hu, W. Zhang, Y. Zhang and S. Zhang, *Nat. Commun.*, 2024, **15**, 6078.

130 Y. Gao, L. Neal, D. Ding, W. Wu, C. Baroi, A. M. Gaffney and F. Li, *ACS Catal.*, 2019, **9**, 8592–8621.

131 L. M. Neal, V. P. Haribal and F. Li, *iScience*, 2019, **19**, 894–904.

132 P. Wang, H. Yang, C. Tang, Y. Wu, Y. Zheng, T. Cheng, K. Davey, X. Huang and S.-Z. Qiao, *Nat. Commun.*, 2022, **13**, 3754.

133 Y. Wang, K. Wang, B. Zhang, X. Peng, X. Gao, G. Yang, H. Hu, M. Wu and N. Tsubaki, *ACS Catal.*, 2021, **11**, 11742–11753.

134 M. Khalil, G. T. M. Kadja, F. A. A. Nugroho, L. G. Sutanto, P. K. Jiwanti, F. F. Abdi, F. Hussin and M. K. Aroua, *Renewable Sustainable Energy Rev.*, 2024, **206**, 114869.

135 R. Li, J. Zhao, B. Liu and D. Wang, *Adv. Mater.*, 2024, **36**, 2308653.

136 T. Mou, H. S. Pillai, S. Wang, M. Wan, X. Han, N. M. Schweitzer, F. Che and H. Xin, *Nat. Catal.*, 2023, **6**, 122–136.

137 Y. Zheng, E. Wang, J. Zhou and Z. Sun, *ACS Mater. Lett.*, 2024, **6**, 3572–3601.

138 L. C. Goveas, S. Nayak, R. Vinayagam, R. Selvaraj and A. Pugazhendhi, *Fuel*, 2023, **348**, 128460.

139 A. R. Fareza, F. A. A. Nugroho, F. F. Abdi and V. Fauzia, *J. Mater. Chem. A*, 2022, **10**, 8656–8686.

140 T. Kawawaki, Y. Mori, K. Wakamatsu, S. Ozaki, M. Kawachi, S. Hossain and Y. Negishi, *J. Mater. Chem. A*, 2020, **8**, 16081–16113.

141 C. F. Bohren and D. R. Huffman, *Absorption and Scattering of Light by Small Particles*, Wiley, 1998.

142 G. Ma, N. Jiang, D. Song, B. Qiao, Z. Xu, S. Zhao and Z. Liang, *J. Mater. Chem. A*, 2025, **13**, 889–917.

143 K. Jakubow-Piotrowska, B. Witkowski, P. Wrobel, K. Miecznikowski and J. Augustynski, *Nanomaterials*, 2024, **14**, 2001.

144 M. Khalil, G. Rahmaningsih, J. Gunlazuardi and A. Umar, *Int. J. Technol.*, 2019, **10**, 808.

145 Z. Xie, X. Liu, P. Jia, Y. Zou and J. Jiang, *Energy Adv.*, 2023, **2**, 1366–1374.

146 P. Subramanyam, T. Khan, G. Neeraja Sinha, D. Suryakala and C. Subrahmanyam, *Int. J. Hydrogen Energy*, 2020, **45**, 7779–7787.

147 S. L. Shinde, S. Ishii, T. D. Dao, R. P. Sugavaneshwar, T. Takei, K. K. Nanda and T. Nagao, *ACS Appl. Mater. Interfaces*, 2018, **10**, 2460–2468.

148 C. W. Moon, M.-J. Choi, J. K. Hyun and H. W. Jang, *Nanoscale Adv.*, 2021, **3**, 5981–6006.

149 B. F. Mohazzab, K. Torabi and D. Gao, *Sustainable Energy Fuels*, 2024, **8**, 5620–5637.

150 R. Verma, R. Rani, P. Choubey, A. Sharma and M. Basu, *ACS Appl. Nano Mater.*, 2024, **7**, 26434–26444.

151 P. Hepperle, W. Y. Baek, H. Nettelbeck and H. Rabus, *Part. Part. Syst. Charact.*, 2022, **39**, 2200136.

152 A. Qdemat, E. Kentzinger, J. Buitenhuis, U. Rücker, M. Ganeva and T. Brückel, *RSC Adv.*, 2020, **10**, 18339–18347.

153 Q. Kong, D. Kim, C. Liu, Y. Yu, Y. Su, Y. Li and P. Yang, *Nano Lett.*, 2016, **16**, 5675–5680.

154 S. Mubarak, D. Dhamodharan, H.-S. Byun, D. K. Pattanayak and S. B. Arya, *J. Ind. Eng. Chem.*, 2022, **113**, 124–131.

155 A. R. Zanatta, *Sci. Rep.*, 2019, **9**, 11225.

156 C. M. Pelicano and H. Tong, *Appl. Res.*, 2024, **3**, e202300080.

157 Y. Zhang, Q. Wang, K. Wang, Y. Liu, L. Zou, Y. Zhou, M. Liu, X. Qiu, W. Li and J. Li, *Chem. Commun.*, 2022, **58**, 9421–9424.

158 Y. Sun, G. Han, L. Du, C. Du, X. Zhou, Q. Sun, Y. Gao, G. Yin, Y. Li and Y. Wang, *Chem Catal.*, 2021, **1**, 1260–1272.

159 J. E. Benedetti, D. R. Bernardo, A. Morais, J. Bettini and A. F. Nogueira, *RSC Adv.*, 2015, **5**, 33914–33922.

160 A. Stefancu, L. Nan, L. Zhu, V. Chiș, I. Bald, M. Liu, N. Leopold, S. A. Maier and E. Cortes, *Adv. Opt. Mater.*, 2022, **10**, 2200397.

161 X.-Q. Liu, F.-F. Meng, X. Chen, Y.-H. Li, H. Yang, F. Peng, X.-H. Lu, Y.-X. Tong, Z.-Q. Tian, J.-F. Li and P.-P. Fang, *iScience*, 2020, **23**, 101107.

162 J. Yi, E.-M. You, S.-Y. Ding and Z.-Q. Tian, *Natl. Sci. Rev.*, 2020, **7**, 1228–1238.

163 X. Feng, X. Feng and F. Zhang, *J. Mater. Chem. A*, 2023, **11**, 20242–20253.

164 L. Luo, W. Chen, S.-M. Xu, J. Yang, M. Li, H. Zhou, M. Xu, M. Shao, X. Kong, Z. Li and H. Duan, *J. Am. Chem. Soc.*, 2022, **144**, 7720–7730.

165 J. F. de Brito, F. F. Hudari and M. V. B. Zanoni, *J. CO$_2$ Util.*, 2018, **24**, 81–88.

166 K. Wang, N. Fan, B. Xu, Z. Wei, C. Chen, H. Xie, W. Ye, Y. Peng, M. Shen and R. Fan, *Small*, 2022, **18**, 2201882.

167 H. A. Chaliyawala, S. Bastide, D. Muller-Bouvet, C. Pichon, K. Bah, A. Djoumoi, F. Marty, T. Bourouina and E. Torralba, *ACS Appl. Energy Mater.*, 2023, **6**, 8397–8409.

168 H. Chaliyawala, S. Bastide, C. Cachet-Vivier, N. Ilic, T. Bourouina, F. Marty, K. Bah and E. Torralba, *ChemElectroChem*, 2025, **12**, e202400405.

169 Q. Shen, Z. Chen, X. Huang, M. Liu and G. Zhao, *Environ. Sci. Technol.*, 2015, **49**, 5828–5835.

170 J. S. DuChene, G. Tagliabue, A. J. Welch, X. Li, W.-H. Cheng and H. A. Atwater, *Nano Lett.*, 2020, **20**, 2348–2358.

171 I. Roh, S. Yu, C.-K. Lin, S. Louisia, S. Cestellos-Blanco and P. Yang, *J. Am. Chem. Soc.*, 2022, **144**, 8002–8006.

172 G. Li, L. Lv, H. Fan, J. Ma, Y. Li, Y. Wan and X. S. Zhao, *J. Colloid Interface Sci.*, 2010, **348**, 342–347.

173 S. Shen, X. Peng, L. Song, Y. Qiu, C. Li, L. Zhuo, J. He, J. Ren, X. Liu and J. Luo, *Small*, 2019, **15**, 1902229.

174 J. Liu, Z. Hu, Z. Huang, X. Zhang, Z. Dong, W. Wu, Y. Zhang, Z. Zhou, Y. Gao and D. Luan, *Ceram. Int.*, 2025, **51**, 9548–9558.

175 R. M. e Silva, F. de Lourdes Souza, E. Dias, G. T. dos, S. T. da Silva, F. E. Durán, A. Rego, D. Higgins and C. Ribeiro, *J. Alloys Compd.*, 2023, **968**, 172090.

176 K. K. Bera, A. Chowdhury, S. K. Bera, M. R. Das, A. Roy, S. Das and S. K. Bhattacharya, *ACS Omega*, 2023, **8**, 28419–28435.

177 R. Xu, Y. Guan, L. Cao, X. Yu, L. Li, B. Ma and C. Liu, *J. Water Proc. Eng.*, 2024, **68**, 106316.

178 L. Mohapatra and S. H. Yoo, *Mater. Today Energy*, 2023, **35**, 101331.

179 G. Ma, N. Jiang, D. Song, B. Qiao, Z. Xu, S. Zhao and Z. Liang, *J. Mater. Chem. A*, 2025, **13**, 889–917.

180 P. Prabha Sarangi, D. Prava Sahoo, U. Aparajita Mohanty, S. Nayak and K. Parida, *ChemCatChem*, 2024, **16**, e202301533.

181 M. P. A. Muthalif, C. D. Sunesh and Y. Choe, *J. Colloid Interface Sci.*, 2019, **534**, 291–300.

182 A. Pal, F. Arshad and M. P. Sk, *Adv. Colloid Interface Sci.*, 2020, **285**, 102274.

183 P. Sun, Z. Xing, Z. Li and W. Zhou, *Chem. Eng. J.*, 2023, **458**, 141399.

184 M. T. Ahmed, S. A. Farooqui, S.-H. Hsu, L. Daeun and S. K. Chaerun, *Solar Light-To-Hydrogenated Organic Conversion: Heterogeneous Photocatalysts*, Springer Nature Singapore, Singapore, 2024.

185 N. Li, X. Liu, J. Zhou, W. Chen and M. Liu, *Chem. Eng. J.*, 2020, **399**, 125782.

186 X. Dou, Q. Zhang, S. N. A. Shah, M. Khan, K. Uchiyama and J.-M. Lin, *Chem. Sci.*, 2019, **10**, 497–500.

187 U. A. Rani, L. Y. Ng, C. Y. Ng and E. Mahmoudi, *Adv. Colloid Interface Sci.*, 2020, **278**, 102124.

188 X. Fan, S. Yu, X. Wang, Z. Li, F. Zhan, J. Li, Y. Gao, A. Xia, Y. Tao, X. Li, L. Zhang, C. Tung and L. Wu, *Adv. Mater.*, 2019, **31**, 1804872.

189 S. Kumbhar and M. De, *Mater. Today: Proc.*, 2023, **76**, 271–278.

190 S. Kumbhar and M. De, *Mater. Sci. Eng., B*, 2023, **298**, 116815.

191 X. Li, J. Wang, A. Wei, X. Li, W. Zhang and Y. Liu, *Sep. Purif. Technol.*, 2024, **332**, 125779.

192 H. Gao, H. Yang, J. Xu, S. Zhang and J. Li, *Small*, 2018, **14**, 1801353.

193 M. Ye, Z. Zhao, Z. Hu, L. Liu, H. Ji, Z. Shen and T. Ma, *Angew. Chem., Int. Ed.*, 2017, **56**, 8407–8411.

194 A. J. King, A. Z. Weber and A. T. Bell, *ACS Appl. Mater. Interfaces*, 2024, **16**, 36380–36391.

195 S. Lee, L. Ji, A. C. De Palma and E. T. Yu, *Nat. Commun.*, 2021, **12**, 3982.

196 D. V. Esposito, I. Levin, T. P. Moffat and A. A. Talin, *Nat. Mater.*, 2013, **12**, 562–568.

197 P. Wen, H. Li, X. Ma, R. Lei, X. Wang, S. M. Geyer and Y. Qiu, *J. Mater. Chem. A*, 2021, **9**, 3589–3596.

198 M. Lubitz, P. A. Medina, A. Antic, J. T. Rosin and B. D. Fahlman, *J. Chem. Educ.*, 2014, **91**, 1022–1027.

199 J. Huang, B. Xu, L. Tian, P. B. Pati, A. S. Etman, J. Sun, L. Hammarström and H. Tian, *Chem. Commun.*, 2019, **55**, 7918–7921.

200 D. Guzmán, M. Isaacs, I. Osorio-Román, M. García, J. Astudillo and M. Ohlbaum, *ACS Appl. Mater. Interfaces*, 2015, **7**, 19865–19869.

201 P. Wen, H. Li, X. Ma, R. Lei, X. Wang, S. M. Geyer and Y. Qiu, *J. Mater. Chem. A*, 2021, **9**, 3589–3596.

202 D. Wei, W. Tang, Y. Gan and X. Xu, *Catal. Sci. Technol.*, 2020, **10**, 5666–5676.

203 Z. Zeng, S. Chen, T. T. Y. Tan and F.-X. Xiao, *Catal. Today*, 2018, **315**, 171–183.

204 J. Ma, H. Yan, X. Hou, M. Xu and T. Cui, *Microstructures*, 2025, **5**, 2025002.

205 D. Tang, J. Liu, X. Zhang, L. Chen, L. Ma and Q. Zhang, *Green Chem.*, 2023, **25**, 7843–7862.

206 S. Wu and P. Schmuki, *Adv. Mater.*, 2025, **37**, 2414889.

207 J. Li, D. Yi, F. Zhan, B. Zhou, D. Gao, D. Guo, S. Liu, X. Wang and J. Yao, *Appl. Catal., B*, 2020, **271**, 118925.

208 G. Gao, Y. Jiao, E. R. Waclawik and A. Du, *J. Am. Chem. Soc.*, 2016, **138**, 6292–6297.

209 Y. Li, Z. Wang, T. Xia, H. Ju, K. Zhang, R. Long, Q. Xu, C. Wang, L. Song, J. Zhu, J. Jiang and Y. Xiong, *Adv. Mater.*, 2016, **28**, 6959–6965.

210 M. Qian, X. Wu, M. Lu, L. Huang, W. Li, H. Lin, J. Chen, S. Wang and X. Duan, *Adv. Funct. Mater.*, 2023, **33**, 2208688.

211 Z. Sun, S. Wang and W. Chen, *J. Mater. Chem. A*, 2021, **9**, 5296–5319.

212 Z. Tian, Y. Da, M. Wang, X. Dou, X. Cui, J. Chen, R. Jiang, S. Xi, B. Cui, Y. Luo, H. Yang, Y. Long, Y. Xiao and W. Chen, *Nat. Commun.*, 2023, **14**, 142.

213 J. Kang, W. He, K. Wang, Y. Chen, Y. Liu, Y. Li and W. Li, *Chem. Commun.*, 2024, **60**, 6039–6042.

214 X. Feng, T. Sun, X. Feng, H. Yu, Y. Yang, L. Chen and F. Zhang, *Adv. Funct. Mater.*, 2024, **34**, 2316238.

215 B. Zhao, X. Huang, Y. Ding and Y. Bi, *Angew. Chem., Int. Ed.*, 2023, **62**, e202213067.

216 H. Yu, W. Wang, Q. Mao, K. Deng, Z. Wang, Y. Xu, X. Li, H. Wang and L. Wang, *Appl. Catal., B*, 2023, **330**, 122617.

217 E. A. Moges, C. Chang, W. Huang, K. Lakshmanan, Y. A. Awoke, C. Pao, M. Tsai, W. Su and B. J. Hwang, *Adv. Funct. Mater.*, 2022, **32**, 2206887.

218 A. A. Ayele, M.-C. Tsai, D. B. Adam, Y. A. Awoke, W.-H. Huang, C.-Y. Chang, S.-C. Liao, P.-Y. Huang, J.-L. Chen, C.-W. Pao, W.-N. Su and B. J. Hwang, *Appl. Catal., A*, 2022, **646**, 118861.

219 Y. Wang, Y.-Q. Zhu, Z. Xie, S.-M. Xu, M. Xu, Z. Li, L. Ma, R. Ge, H. Zhou, Z. Li, X. Kong, L. Zheng, J. Zhou and H. Duan, *ACS Catal.*, 2022, **12**, 12432–12443.

220 S. Wu and P. Schmuki, *Adv. Mater.*, 2025, **37**, 2414889.

221 N. Gao, H. Yang, D. Dong, D. Dou, Y. Liu, W. Zhou, F. Gao, C. Nan, Z. Liang and D. Yang, *J. Colloid Interface Sci.*, 2022, **611**, 294–305.

222 Z. Chi, J. Zhao, Y. Zhang, H. Yu and H. Yu, *Green Energy Environ.*, 2022, **7**, 372–393.

223 G. Zhao, J. Zou, X. Chen, J. Yu and F. Jiao, *Chem. Eng. J.*, 2020, **397**, 125407.

224 G. Fan, F. Li, D. G. Evans and X. Duan, *Chem. Soc. Rev.*, 2014, **43**, 7040–7066.

225 Y. Miao, Z. Li, Y. Song, K. Fan, J. Guo, R. Li and M. Shao, *Appl. Catal., B*, 2023, **323**, 122147.

226 B. Gao, X. Mu, J. Liu, J. Feng, H. Huang, Z. Zou and Z. Li, *J. Phys. Chem. Lett.*, 2024, **16**, 148–152.

227 Q. Wang, X. Ma, P. Wu, B. Li, L. Zhang and J. Shi, *Nano Energy*, 2021, **89**, 106326.

228 L. Luo, Z. J. Wang, X. Xiang, D. Yan and J. Ye, *ACS Catal.*, 2020, **10**, 4906–4913.

229 F. Kang, Q. Wang, D. Du, L. Wu, D. W. F. Cheung and J. Luo, *Angew. Chem., Int. Ed.*, 2025, **64**, e202417648.

230 L. Niu, R. Tian, W. Zhang, H. Wang, J. Wang and Y. Liu, *ACS Catal.*, 2025, **15**, 2124–2138.

231 I. Carrai, R. Mazzaro, C. Bellatreccia, A. Piccioni, M. Salvi, S. Grandi, S. Caramori, P. Ceroni and L. Pasquini, *ChemSusChem*, 2025, **18**, e202402604.

232 Y. Piekner, D. S. Ellis, D. A. Grave, A. Tsyganok and A. Rothschild, *Energy Environ. Sci.*, 2021, **14**, 4584–4598.

233 I. Carrai, R. Mazzaro, E. Bassan, G. Morselli, A. Piccioni, S. Grandi, S. Caramori, P. Ceroni and L. Pasquini, *Sol. RRL*, 2023, **7**, 2300205.

234 H. Yang, X. Liu, K. Qin, Q. Bu and Q. Liu, *Inorg. Chem.*, 2022, **61**, 7414–7425.

235 Z. Wei, Y. Su, W. Pan, J. Shen, R. Fan, W. Yang, Z. Deng, M. Shen and Y. Peng, *Angew. Chem., Int. Ed.*, 2023, **62**, e202305558.

236 M. Khalil, J. Gunlazuardi, T. A. Ivandini and A. Umar, *Renewable Sustainable Energy Rev.*, 2019, **113**, 109246.

237 P. B. Pati, M. Abdellah, S. Diring, L. Hammarström and F. Odobel, *ChemSusChem*, 2021, **14**, 2902–2913.

238 X. Liang, X. Cao, W. Sun and Y. Ding, *ChemCatChem*, 2019, **11**, 6190–6202.

239 Z. N. Zahran, Y. Tsubonouchi, E. A. Mohamed and M. Yagi, *ChemSusChem*, 2019, **12**, 1775–1793.

240 J. Hawecker, J.-M. Lehn and R. Ziessel, *J. Chem. Soc., Chem. Commun.*, 1984, 328–330.

241 X. Jia, E. Stewart-Jones, J. L. Alvarez-Hernandez, G. P. Bein, J. L. Dempsey, C. L. Donley, N. Hazari, M. N. Houck, M. Li, J. M. Mayer, H. S. Nedzbala and R. E. Powers, *J. Am. Chem. Soc.*, 2024, **146**, 7998–8004.

242 J. J. Leung, J. Warnan, K. H. Ly, N. Heidary, D. H. Nam, M. F. Kuehnel and E. Reisner, *Nat. Catal.*, 2019, **2**, 354–365.

243 B. Shang, C. L. Rooney, D. J. Gallagher, B. T. Wang, A. Krayev, H. Shema, O. Leitner, N. J. Harmon, L. Xiao, C. Sheehan, S. R. Bottum, E. Gross, J. F. Cahoon, T. E. Mallouk and H. Wang, *Angew. Chem., Int. Ed.*, 2023, **62**, e202215213.

244 A. M. May and J. L. Dempsey, *Chem. Sci.*, 2024, **15**, 6661–6678.

245 Z. Li, J. Cai, L. Wang and C. Duan, *ACS Catal.*, 2024, **14**, 16374–16382.

246 M. Zhan, Y. Wang, H. Liu, R. Zhang, L. Peng and J. Zhang, *Mol. Catal.*, 2024, **553**, 113788.

247 L. Yao, Y. Liu, H.-H. Cho, M. Xia, A. Sekar, B. Primera Darwich, R. A. Wells, J.-H. Yum, D. Ren, M. Grätzel, N. Guijarro and K. Sivula, *Energy Environ. Sci.*, 2021, **14**, 3141–3151.

248 R. Francke, B. Schille and M. Roemelt, *Chem. Rev.*, 2018, **118**, 4631–4701.

249 T. Butburee, Y. Bai, H. Wang, H. Chen, Z. Wang, G. Liu, J. Zou, P. Khemthong, G. Q. M. Lu and L. Wang, *Adv. Mater.*, 2018, **30**, 1705666.

250 S. Manna, A. K. Satpati, C. N. Patra and A. K. Tyagi, *ACS Omega*, 2024, **9**, 6128–6146.

251 D. Ma, C. Zhi, Y. Zhang, J. Chen, Y. Zhang and J.-W. Shi, *ACS Nano*, 2024, **18**, 21714–21746.

252 Z.-Y. Zhou, N. Tian, J.-T. Li, I. Broadwell and S.-G. Sun, *Chem. Soc. Rev.*, 2011, **40**, 4167.

253 A. C. Muñoz Peña, E. Flórez and F. Núñez-Zarur, *ChemistryOpen*, 2025, **14**, e202400153.

254 Y. Wei, Y. Li, Y. Xu, Y. Sun, T. Xu, H. Liang and J. Bai, *Front. Chem. Sci. Eng.*, 2024, **18**, 53.

255 G. L. De Gregorio, T. Burdyny, A. Loiudice, P. Iyengar, W. A. Smith and R. Buonsanti, *ACS Catal.*, 2020, **10**, 4854–4862.

256 D. Kim, L. S. Oh, Y. C. Tan, H. Song, H. J. Kim and J. Oh, *ACS Catal.*, 2021, **11**, 14926–14931.

257 P. Tereshchuk, A. S. Chaves and J. L. F. Da Silva, *J. Phys. Chem. C*, 2014, **118**, 15251–15259.

258 H. Mou, F. Lu, Z. Zhuang, Q. Chang, L. Zhang, X. Chen, Y. Zhang and J. G. Chen, *Precis. Chem.*, 2024, **2**, 103–111.

259 T.-G. Vo, C.-C. Kao, J.-L. Kuo, C. Chiu and C.-Y. Chiang, *Appl. Catal., B*, 2020, **278**, 119303.

260 Y. Xiao, M. Wang, D. Liu, J. Gao, J. Ding, H. Wang, H. Bin Yang, F. Li, M. Chen, Y. Xu, D. Xu, Y. Zhang, S. Fang, X. Ao, J. Wang, C. Su and B. Liu, *Angew. Chem., Int. Ed.*, 2024, **63**, e202319685.

261 Y.-M. Zhang, Z.-Y. Zhao, M. Yang, D. Xiong, W. Tang and Y.-K. Zhao, *Int. J. Hydrogen Energy*, 2024, **51**, 1236–1247.

262 W. Sun, Y. Dong, X. Zhai, M. Zhang, K. Li, Q. Wang and Y. Ding, *Chem. Eng. J.*, 2022, **430**, 132872.

263 M. H. Huang, *Small*, 2019, **15**, 1804726.

264 Y. Gao, X. Zhang, C. Ban, R. Feng, J. Hou, J. Meng, G. Yang, C. Gao, L. Xia, P. Ma, K. Wang and X. Qu, *Mater. Today Energy*, 2024, **40**, 101483.

265 M. D'Arienzo, M. V. Dozzi, M. Redaelli, B. Di Credico, F. Morazzoni, R. Scotti and S. Polizzi, *J. Phys. Chem. C*, 2015, **119**, 12385–12393.

266 J. Yu, J. Low, W. Xiao, P. Zhou and M. Jaroniec, *J. Am. Chem. Soc.*, 2014, **136**, 8839–8842.

267 S. Lardhi, L. Cavallo and M. Harb, *J. Phys. Chem. Lett.*, 2020, **11**, 5497–5503.

268 E. Pastor, L. Montañés, A. Gutiérrez-Blanco, F. S. Hegner, C. A. Mesa, N. López and S. Giménez, *Nanoscale*, 2022, **14**, 15596–15606.

269 Q. Shen, W. Kang, L. Ma, Z. Sun, B. Jin, H. Li, Y. Miao, H. Jia and J. Xue, *Chem. Eng. J.*, 2023, **478**, 147338.

270 X. Gong, S. Fan, Q. Yang, J.-L. Yang, Y. chen, X. Qi, H. Shen, D. Ren and M. Wang, *Chem. Eng. J.*, 2024, **493**, 152773.

271 Z. Liu, Y. Guo, Q. Ge and X. Zhu, *React. Chem. Eng.*, 2025, **10**, 750–767.

272 H. Zhang, S. Wang, Y. Li, M. Wang, N. Wang, Z. Liu, B. Zheng, Y. Xi, M. Wu and W. Wu, *Chem. Eng. J.*, 2025, **505**, 159227.

273 Z. Yang, R. Xu, H. Tao, Y. Yang, Y. Hou, K. Wang, J. Zhang, Z. Yu, M. Anpo and X. Fu, *J. Catal.*, 2024, **438**, 115714.

274 Q. Chen, N. Gong, Q. Zhang, W. Peng, Y. Li, F. Zhang and X. Fan, *Chem Catal.*, 2023, **3**, 100646.

275 Y. Li and C. Zhang, *Chem. Eng. J.*, 2024, **487**, 150687.

276 Q. Li, J. Li, H. Bai and F. Li, *Chin. J. Catal.*, 2024, **58**, 86–104.

277 P. Tereshchuk, R. C. Amaral, Y. Seminovski and J. L. F. Da Silva, *RSC Adv.*, 2017, **7**, 17122–17127.

278 H. Yan, M. Zhao, G. Wang, X. Zhou, X. Feng, Y. Liu and C. Yang, *Chem. Eng. J.*, 2024, **500**, 156842.

279 W. Lei, Y. Yu, H. Zhang, Q. Jia and S. Zhang, *Mater. Today*, 2022, **52**, 133–160.

280 H. K. Woo, A. K. Gautam, J. S. Barroso-Martínez, A. P. Baddorf, K. Zhou, Y. Y. Choi, J. He, A. V. Mironenko, J. Rodríguez-López and L. Cai, *Nano Lett.*, 2023, **23**, 11493–11500.

281 X. Wang, S. Ma, B. Liu, S. Wang and W. Huang, *Chem. Commun.*, 2023, **59**, 10044–10066.

282 H. Wu, S. Qu, Z. Xie and Y. H. Ng, *ACS Appl. Energy Mater.*, 2022, **5**, 8419–8427.

283 P. Yang, H. Shi, H. Wu, D. Yu, L. Huang, Y. Wu, X. Gong, P. Xiao and Y. Zhang, *Nanoscale*, 2023, **15**, 4536–4545.

284 L. Wang, Z. Chen, Q. Zhao, N. Wen, S. Liang, X. Jiao, Y. Xia and D. Chen, *Adv. Funct. Mater.*, 2024, **34**, 2409349.

285 Z. Kang, Y. Zheng, H. Li, Y. Shen, W. Zhang, M. Huang and X. Tao, *Chem. Eng. J.*, 2024, **499**, 156324.

286 M. Kan, C. Yang, Q. Wang, Q. Zhang, Y. Yan, K. Liu, A. Guan and G. Zheng, *Adv. Energy Mater.*, 2022, **12**, 2201134.

287 J. Albero, Y. Peng and H. García, *ACS Catal.*, 2020, **10**, 5734–5749.

288 H. Sun, R. Tang, L. Wang, Y. Liang, W. Yang, Z. Lin, X. Zhang, K. Chen, W. Liang, S. Zhao, R. Zheng and J. Huang, *EES Catal.*, 2025, **3**, 337–346.

289 Y. Lu, B. G. Lee, C. Lin, T.-K. Liu, Z. Wang, J. Miao, S. H. Oh, K. C. Kim, K. Zhang and J. H. Park, *Nat. Commun.*, 2024, **15**, 5475.

290 Y. Jung, S. Kim, S. Kim, Y. Kim, J. B. Hwang, D. Kim and S. Lee, *Small*, 2025, **21**, 2409082.

291 Y. Kwon, Y. Birdja, I. Spanos, P. Rodriguez and M. T. M. Koper, *ACS Catal.*, 2012, **2**, 759–764.

292 S. Zhou, K. Sun, J. Huang, X. Lu, B. Xie, D. Zhang, J. N. Hart, C. Y. Toe, X. Hao and R. Amal, *Small*, 2021, **17**, 2100496.

293 S. Zhou, K. Sun, C. Y. Toe, J. Yin, J. Huang, Y. Zeng, D. Zhang, W. Chen, O. F. Mohammed, X. Hao and R. Amal, *Adv. Mater.*, 2022, **34**, 2201670.

294 W. Chen, N. Pan, L. Luo, Y. Miao, S. Zhang, Z. Zhang, R. Zhang, Z. Li and M. Shao, *AIChE J.*, 2024, **70**, e18591, DOI: **10.1002/aic.18591**.

295 Z. Wang, M. Xiao, J. You, G. Liu and L. Wang, *Acc. Mater. Res.*, 2022, **3**, 1127–1136.

296 J. Zheng, Y. Lyu, B. Wu and S. Wang, *EnergyChem*, 2020, **2**, 100039.

297 W. Lei, Y. Yu, H. Zhang, Q. Jia and S. Zhang, *Mater. Today*, 2022, **52**, 133–160.

298 C. Li, X. Zhou, Q. Zhang, Y. Xue, Z. Kuang, H. Zhao, C. Mou and H. Chen, *ChemSusChem*, 2022, **15**, e202200188.

299 E. Plaza-Mayoral, P. Sebastián-Pascual, K. N. Dalby, K. D. Jensen, I. Chorkendorff, H. Falsig and M. Escudero-Escribano, *Electrochim. Acta*, 2021, **398**, 139309.

300 H. Kim, M.-C. Kim, S. Kim, Y.-S. Kim, J.-H. Choi and K.-W. Park, *RSC Adv.*, 2020, **10**, 10519–10525.

301 K. Rakhimbekov, J. Potgieter, D. Valiev, V. An, A. Blinova, N. Usoltseva, A. Pustovalov, M. Vasilevichev, A. Platonova, S. Stepanov, D. Kokotov and V. Sypchenko, *ACS Appl. Energy Mater.*, 2024, **7**, 9756–9765.

302 A. Rokade, G. K. Rahane, A. Živković, S. N. Rahane, H. S. Tarkas, K. Hareesh, N. H. de Leeuw, S. D. Sartale, N. Y. Dzade, S. R. Jadkar and S. R. Rondiya, *Langmuir*, 2024, **40**, 6884–6897.

303 Q. Yang, C. Zhang, B. Dong, Y. Cui, F. Wang, J. Cai, P. Jin and L. Feng, *Appl. Catal., B*, 2021, **296**, 120359.

304 X. Rao, S. Zhang and J. Zhang, *Curr. Opin. Electrochem.*, 2023, **42**, 101416.

305 G. Edman Jonsson, H. Fredriksson, R. Sellappan and D. Chakarov, *Int. J. Photoenergy*, 2011, **2011**, 1–11.

306 Y.-S. Park and J. S. Lee, *ACS Photonics*, 2017, **4**, 2587–2594.

307 T. Butburee, Y. Bai, H. Wang, H. Chen, Z. Wang, G. Liu, J. Zou, P. Khemthong, G. Q. M. Lu and L. Wang, *Adv. Mater.*, 2018, **30**, 201705666.

308 H. Li, Z. Li, Y. Yu, Y. Ma, W. Yang, F. Wang, X. Yin and X. Wang, *J. Phys. Chem. C*, 2017, **121**, 12071–12079.

309 J. W. Yoon, D. H. Kim, J.-H. Kim, H. W. Jang and J.-H. Lee, *Appl. Catal., B*, 2019, **244**, 511–518.

310 J. L. Montaño-Priede and U. Pal, *J. Phys. Chem. C*, 2019, **123**, 11833–11839.

311 A. Agrawal, I. Kriegel and D. J. Milliron, *J. Phys. Chem. C*, 2015, **119**, 6227–6238.

312 R. K. Saini, A. Kumar, V. Goyal, A. Agarwal and R. Prajesh, *Mater. Today: Proc.*, 2023, **76**, 383–387.

313 C. L. Nehl and J. H. Hafner, *J. Mater. Chem.*, 2008, **18**, 2415.

314 H. Bin Jeon, P. V. Tsalu and J. W. Ha, *Sci. Rep.*, 2019, **9**, 13635.

315 A. Rabkin, O. Friedman and Y. Golan, *J. Colloid Interface Sci.*, 2015, **457**, 43–51.

316 W. Lu, Y. Zhang, J. Zhang and P. Xu, *Ind. Eng. Chem. Res.*, 2020, **59**, 5536–5545.

317 X. Lu, S. Xie, H. Yang, Y. Tong and H. Ji, *Chem. Soc. Rev.*, 2014, **43**, 7581–7593.

318 A. Khan, A. Adam, Md. A. Aziz, M. I. Ahmed, Z. H. Yamani and M. Qamar, *Int. J. Hydrogen Energy*, 2019, **44**, 23054–23065.

319 M. Khalil, B. M. Jan, C. W. Tong and M. A. Berawi, *Appl. Energy*, 2017, **191**, 287–310.

320 Y. Zi, Y. Hu, J. Pu, M. Wang and W. Huang, *Small*, 2023, **19**, 202208274.

321 S. Çetinkaya, G. Khamidov, L. Özcan, L. Palmisano and S. Yurdakal, *J. Environ. Chem. Eng.*, 2022, **10**, 107210.

322 Y. Lu, T.-K. Liu, C. Lin, K. H. Kim, E. Kim, Y. Yang, X. Fan, K. Zhang and J. H. Park, *Nano Lett.*, 2024, **24**, 4633–4640.

323 A. Ma, Y. Lee, D. Seo, J. Kim, S. Park, J. Son, W. Kwon, D. Nam, H. Lee, Y. Kim, H. Um, H. Shin and K. M. Nam, *Adv. Sci.*, 2024, **11**, 202400874.

324 D. Liu and Y. Kuang, *Adv. Mater.*, 2024, **36**, 202311692.

325 Z. Qiu and D. Tang, *J. Mater. Chem. B*, 2020, **8**, 2541–2561.

326 F. E. Osterloh, *Chem. Soc. Rev.*, 2013, **42**, 2294–2320.

327 A. Vilanova, P. Dias, T. Lopes and A. Mendes, *Chem. Soc. Rev.*, 2024, **53**, 2388–2434.

328 Y. Yan, Q. Wang, P. Hao, H. Zhou, X. Kong, Z. Li and M. Shao, *ACS Appl. Mater. Interfaces*, 2023, **15**, 23265–23275.

329 X. Li, J. Wang, A. Wei, X. Li, W. Zhang and Y. Liu, *Sep. Purif. Technol.*, 2024, **332**, 125779.

330 P. Uthirakumar, H. Son, V. Dao, Y. Lee, S. Yadav and I.-H. Lee, *J. Environ. Chem. Eng.*, 2024, **12**, 112442.

331 W. Lin, Y. Yang and H. Tuan, *Small*, 2023, **19**, 202300046.

332 C. Feng, F. Wang, Z. Liu, M. Nakabayashi, Y. Xiao, Q. Zeng, J. Fu, Q. Wu, C. Cui, Y. Han, N. Shibata, K. Domen, I. D. Sharp and Y. Li, *Nat. Commun.*, 2021, **12**, 5980.

333 C. Feng and Y. Li, *Chin. J. Catal.*, 2024, **60**, 158–170.

334 D. Hansora, J. W. Yoo, R. Mehrotra, W. J. Byun, D. Lim, Y. K. Kim, E. Noh, H. Lim, J.-W. Jang, S. Il Seok and J. S. Lee, *Nat. Energy*, 2024, **9**, 272–284.

335 S. Dilger, M. Trottmann and S. Pokrant, *ChemSusChem*, 2019, **12**, 1931–1938.